High Temperature Co-Sintering for Metal Supported-Solid Oxide Fuel Cell Fabrication

By

Sannan Yousaf Toor

A thesis
presented to the University of Waterloo
in fulfillment of the
thesis requirement for the degree of
Doctor in Philosophy
in
Chemical Engineering

Waterloo, Ontario, Canada, 2019

Examining Committee Membership

The following served on the Examining Committee for this thesis. The decision of the Examining Committee is by majority vote.

External Examiner	Michael Tucker Chemist Research Scientist Lawrence Berkeley National Laboratory
Supervisor(s)	Eric Croiset Department Chair and Professor Chemical Engineering University of Waterloo
Internal Member	Zhongwei Chen Professor-Chemical Engineering-University of Waterloo Canada Research Chair in Advanced Materials for Clean Energy
Internal Member	Michael Fowler Professor-Chemical Engineering University of Waterloo
Internal-external Member	Robert Varin Professor-Mechanical and Mechatronic Engineer University of Waterloo

AUTHORS DECLERATION

I hereby declare that I am the sole author of this thesis. This is a true copy of the thesis, including any required final revisions, as accepted by my examiners.

I understand that my thesis may be made electronically available to the public.

ABSTRACT

Metal supported-solid oxide fuel cells (MS-SOFC) are third generation solid oxide fuel cells (SOFC). In these cells the primary support is a porous metal upon which the active cell layers (anode, electrolyte, and cathode) are deposited. MS-SOFCs are known for their better mechanical stability, tolerance to redox cycles, and are also cheaper than all-ceramic cells since the conventional support material (one of the active components) is almost entirely replaced by a cheaper metal. Several MS-SOFC fabrication methods have been reported in the literature, including thermal spray deposition on pre-fabricated porous metal support, and tape casting and co-sintering of half-cell layers (metal support and electrolyte). In this thesis a study is done on MS-SOFC's fabrication using tape casting and high temperature co-sintering in non-oxidizing atmosphere to protect the metal support. The MS-SOFCs studied had SS-430L as metal support, and samarium doped ceria (SDC) or yittrium stabilized zirconia (YSZ) as electrolyte.

To use SDC as electrolyte, the co-sintering temperature should be lowered to mitigate the reduction of cerium (IV) to cerium (III) in ceria when exposed to reducing atmosphere at high temperatures. To lower the sintering temperature varying amounts of copper (0 - 5.0 mol%) were used as sintering aid with SDC. X-ray diffraction (XRD), scanning electron microscopy (SEM), energy dispersive x-ray (EDX), and electrochemical impedance spectroscopy (EIS) were used to characterize SDC with and without copper.

Upon doping, copper goes in the SDC crystal structure and starts forming an additional copper oxide phase for copper content above 0.1 mol%. The SDC crystal lattice constant decreased from 0.5446 to 0.5427 nm when the copper content was increased from 0 to 5.0 mol%. SEM of sintered samples showed similar grain size (1-2 microns) and shape, and minimum visible surface porosity for samples containing 0.5 mol% and more copper. Even though as copper content is increased, the sintering temperature decreases, the ionic conductivity also decreases. 0.5 mol% copper shows the best compromise, with sintering temperature lowered to 1180°C compared to 1350°C for plain SDC, and total conductivity of 0.065 $S.cm^{-1}$ compared to 0.077 $S.cm^{-1}$ for plain SDC at 800°C. The amount of additional copper oxide phase is lowest for 0.5 mol% copper co-doped SDC, limiting the effect on SDC's grain boundary conduction.

To use tape casting and co-sintering for MS-SOFC half-cell fabrication, shrinkage analysis of cell components (metal support and electrolyte) were carried out using dilatometry. The shrinkage analysis includes the effect of sintering profile (temperature profile, and sintering atmosphere) on the shrinkage dynamics of cell components. YSZ shows similar shrinkage behavior in inert and reducing atmospheres, however increasing the ramping rate between 1000℃ and 1350℃ shifts the maximum shrinkage rate peak to a higher temperature. Dilatometry analysis showed that reducing atmosphere is more suitable for co-sintering than inert atmosphere, as co-sintering in inert atmosphere leads to formation of silica and alumina in the metal support. In addition to being non-conductive, silica and alumina act as sintering aids that enhance the shrinkage of SS-430L. Hence, upon reaching the co-sintering temperature (1350℃) in inert atmosphere, SS-430L is close to its final shrinkage (~ 1% shrinkage left) and is rigid. However, upon reaching the co-sintering temperature in inert atmosphere, YSZ is not as close to its maximum shrinkage (~3-5% shrinkage left). Therefore, continued shrinkage of thin YSZ layer on rigid SS-430L surface will lead to cracks and delamination.

By increasing the ramping rate during co-sintering in reducing atmosphere the shrinkage of SS-430L can be increased to an extent that it is similar to YSZ shrinkage upon reaching sintering temperature. At a ramping rate of 5.0℃/min, the shrinkage of SS-430L layer and YSZ were 17.1% and 18.1%, respectively as opposed to 8.8% and 17.1% at 2.5℃/min ramping. Since increasing ramping rate shifts the maximum shrinkage rate to a higher temperature for YSZ, upon reaching sintering temperature YSZ is not as close to its maximum shrinkage. For 5℃/min ramping rate upon reaching sintering temperature YSZ has to shrink 2.4% more to get to maximum shrinkage whereas sample with 7.5℃/min ramping rate has to shrink 3.1% to get to maximum shrinkage. This means that the thin YSZ layer is softer upon reaching the sintering temperature at higher ramping rate and will not crack upon continued shrinking. In this study, 7.5℃/min ramping rate gives the best co-sintered half-cells without physical defects. The anode catalyst (NiO/SDC) was infiltrated as a solution in the porous metal support, and the cathode catalyst (LSCF/GDC) was printed on YSZ. Initial cell performance testing showed open circuit voltage of 0.989 V at 700℃ and maximum power density of only 0.5 $mW.cm^{-2}$ at 700℃.

For MS-SOFCs with copper co-doped SDC, 0.5 mol% copper co-doped SDC was used. There is a difference in shrinkage set off temperature for copper co-doped SDC and SS-430L, where

shrinkage of copper co-doped SDC starts around 700℃ compared to 1100℃ for SS-430L. This means that during co-sintering, the copper co-doped SDC layer will be close to its maximum shrinkage when the sample reaches 1100℃, which is only when SS-430L starts shrinking. Due to such a difference in shrinkage behaviors, MS-SOFC with copper co-doped SDC were not successfully fabricated. Contrary to the initial hypothesis to lower the sintering temperature, because of shrinkage dynamics of SS-430L, higher co-sintering temperatures may be more suitable.

Acknowledgments

Firstly, I would like to thank God Almighty for giving me a chance to be part of such a prestigious institution and the SOFC research group, and for all of His help when I did not know any better.

I sincerely thank my supervisor, Dr. Eric Croiset, who has my deepest appreciation for all of his help through out this time period. I am forever grateful for his support, mentorship, guidance, advice, and encouragement, without which this project would not have been possible.

I appreciate the help from Ms. Judy Caron, Ms. Rose Guderian and Ms. Ingrid Sherrer in the Department of Chemical Engineering for administration work and Mr. Bert Habicher and Mr. Ralph Dickhout for their technical support.

To my colleagues and friends at the university, I thank you for sharing your knowledge with me, your support, care, and all the memorable time we spent together.

Finally, to my parents and my siblings, I would have never even thought of this if I did not have my mothers support, love, and teachings. Your never-ending love and care helped me every single step of the way. I would like to express my love and gratitude for my family for making this possible.

I thank my sister, Dr. Sheza Arif Toor, for helping me reason in difficult times.

Table of Contents

AUTHORS DECLERATION iii

ABSTRACT iv

Acknowledgments vii

Table of Contents viii

List of Figures xii

List of Tables xviii

Nomenclature xx

Chapter 1 Introduction and Motivation 1

1.1 Fundamental of Fuel Cells 1

1.1.1 Working of a Fuel Cell 2

1.1.2 Types of Fuel Cells 6

1.2 Fundamentals of Solid Oxide Fuel Cells 9

1.3 Motivation 10

1.4 Organization of Thesis 15

Chapter 2 Literature Review 17

2.1 Metal Supported Solid Oxide Fuel Cells 17

2.2 Materials used in MS-SOFC 19

2.2.1 Material for metal support 19

2.2.2 Anode 21

2.2.3 Electrolyte 28

2.2.4 Cathode 31

2.2.5 Structures of co-sintered MS-SOFC 35

2.2 Use of sintering aid for doped ceria electrolytes 38

Chapter 3 Theoretical Background on Sintering 40

3.1 Working principles of sintering 40

3.2 Enhanced sintering through sintering aid 46

Chapter 4 Experimental methods 49

4.1 Use of sintering aid: 49

4.1.1 Fabrication of the electrolyte 50

4.1.2 Sample preparation for physical properties characterization 52

4.2 Fabrication of MS-SOFC via tape casting and co-sintering. 54

4.2.1 Experimental approach 55

4.2.2 Experimental procedure and details for slurry formulation and tape casting 61

4.3 Apparatus and techniques used 64

4.3.1 X-Ray Diffraction 64

4.3.2 Scanning Electron Microscopy (SEM) 65

4.3.3 Dilatometry Analysis 65

4.3.4 Electrochemical Testing 66

4.3.5 Porosity measurement 71

Chapter 5 Use of Sintering Aid with SDC Electrolyte 72

5.1 Introduction 72

5.2 Experimental procedure 73

5.2.1 Physical Characterization 74

5.2.2 Conductivity Characterization 75

5.3 Results and Discussion 77

5.3.1 Physical characterization 77

5.3.2 Conductivity Characterization 86

Summary 91

Chapter 6 Fabrication of Metal Supported-Solid Oxide Fuel Cells using Tape Casting and Co-Sintering 94

6.1 Introduction 94

6.2 Experimental 95

6.2.1 Selection of materials for metal support 95

6.2.2 Slurry synthesis for tape casting 96

6.2.3 Shrinkage analysis of cell components 98

6.2.4 Effect of pore former content on final porosity of sintered metal support 98

6.2.5 Fabrication of MS-SOFC using tape casting and co-sintering. 99

6.3 Results 100

6.3.1 Selection of material for metal support 100

6.3.2 Effect of pore former content on final porosity of sintered metal support 101

6.3.3 Shrinkage analysis of cell components 102

6.3.4 Fabrication of MS-SOFCs with copper co-doped SDC 117

6.3.5 Fabrication of MS-SOFC with YSZ electrolyte using tape casting and co-sintering 117

Summary 130

Chapter 7 Conclusions and Recommendations 133

7.1 Conclusions 133

7.1.1 Use of copper as sintering aid for SDC 133

7.2 Recommendations. 135

7.2.1 Use of copper as sintering aid for SDC 135

7.2.2 Fabrication of MS-SOFC using tape casting and co-sintering 135

References 137

APPENDIX A 150

Porosity calculation for sintered metal support 150

APPENDIX B 151

Use of EIS for conductivity and activation energy calculation. 151

List of Figures

Figure 1.1: Ideal and actual fuel cell voltage/current characteristics [3]. 5

Figure 1.2: Schematic of a Solid Oxide Fuel Cell. 9

Figure 1.3: Material limitations for SOFC [6]. 10

Figure 1.4: SEM image of cross section of an Anode Supported Cell (ASC) with a vertical crack passing through the electrolyte layer [15]. 12

Figure 1.5: Schematic of a) Anode Supported Cell (ASC) and b) Metal Supported Cell (MS-SOFC). 13

Figure 2.1: Impedance spectra of a metal supported solid oxide fuel cell with impregnated nickel as anode and Strontium Samarium Cobalt oxide (SSC) as cathode [38]. 22

Figure 2.2: SEM image of MS-SOFC with Ni-SDC as the functional anode. (ao) before cell operation and (a1) picture after cell operation of 175 hours at 700°C [66]. 25

Figure 2.3: SEM image coupled with EDX spectra for MS-SOFC cells with an adhesion layer between metal support and anode (a) Image and spectra before operation (b) Image and spectra after operation [37]. 26

Figure 2.4: a) polarization curve for MS-SOFC with Ni-GDC (red) and Ru-GDC (black) as anode, b) impedance spectra of MS-SOFC with Ni-GDC (red) and Ru-GDC (Black) as anode [70]. 27

Figure 2.5: a) comparison of OCV of cells with bi-layered ScSZ-SDC as electrolyte (OCV1) and cell with just SDC as electrolyte (OCV2); b) comparison of MPD of cell with bi-layered ScSZ-SDC as electrolyte (MPD1) and cell with just SDC as electrolyte (MPD2)[88]. 30

Figure 2.6: SEM image of cross-section of a symmetrical MS-SOFC [28]. 36

Figure 2.7: SEM image of cross-section of MS-SOFC, left to right-Porous metal support| Electrolyte| YSZ cathode backbone [38]. 37

Figure 2.8: SEM of cross-section of co-sintered MS-SOFC [59]..... 37

Figure 3.1: Various types of sintering on a phase diagram [118]..... 40

Figure 3.2: Illustration of densification and grain growth, the two paths for sintering [118]. .. 42

Figure 3.3: Surface curvature showing vacancy movement in solids [119]..... 44

Figure 3.4: Solid state sintering mechanisms [119]..... 45

Figure 3.5: Grain boundary diffusion in a) solid state sintering and in b) liquid-phase sintering. 48

Figure 4.1: Picture of apparatus used for GNC process. 52

Figure 4.2: Sequence of experiments conducted to study the effect of copper as sintering aid with SDC..... 53

Figure 4.3: Sequence of experiments conducted in study of tape casting and co-sintering for MS-SOFC. 56

Figure 4.4: Picture of apparatus used for anode electro-catalyst infiltration..... 60

Figure 4.5: Schematic of reaction tube assembly for EIS and Electrochemical testing. 67

Figure 4.6: Typical Nyquist plot for a solid electrolyte..... 69

Figure 4.7: An example of equivalent circuit. 70

Figure 5.1: Schematic of test for rig for electrochemical testing..... 76

Figure 5.2: XRD spectra of different electrolyte samples. 78

Figure 5.3: SEM images of electrolyte samples sintered at 1100°C; a) Pure SDC sample, b) 0.1 CSDC sample, and c) 0.5 CSDC sample, d) 1.0 CSDC, e) 3.0 CSDC, and f) 5.0 CSDC..... 81

Figure 5.4: SEM of PSDC samples sintered at 1350°C; a) 5 KX magnification and b) 50 KX magnification. 82

Figure 5.5: SEM in Back Scattered Electron (BSD) mode for a) 0.1 CSDC, b) .0.5 CSDC, and c) 1.0 CSDC sintered at 1100℃ for 5 hours. 82

Figure 5.6: SEM and EDX of 0.5-CSDC sintered at 1100℃ for 5 hours. 83

Figure 5.7: Shrinkage curve for SDC with and without copper doping; PSDC, 0.1 CSDC, 0.5 CSDC, and 5.0 CSDC. 84

Figure 5.8: Shrinkage rate versus temperature for electrolyte samples. 86

Figure 5.9: Arrhenius plot of total conductivity for different electrolyte samples. 87

Figure 5.10: Nyquist plot for 0.1 CSDC at a) 400℃ and b) 700℃. 88

Figure 5.11: SEM image of a) 0.5 CSDC, b) 1.0 CSDC, and c) 3.0 CSDC. 89

Figure 5.12: Arrhenius plot of conductivity; a) grain bulk conductivity, and b) grain boundary conductivity. 90

Figure 5.13: Activation energy as a function of copper content of SDC. 91

Figure 6.1: Shrinkage curve for SS 430-L and SS 410-L and temperature profile used for dilatometry tests. 101

Figure 6.2: Porosity percentage versus pore former content in metal support slurry. Porosity measurements were done twice; first trial is labelled Data Set 1 and second trial is labelled Data Set 2. 102

Figure 6.3: Sintering temperature profiles used for dilatometry analysis. 103

Figure 6.4: Shrinkage profiles for SS-430L under different ramping rates in reducing atmosphere. 104

Figure 6.5: Shrinkage rate versus temperature for SS-430L with 2.5, and 5.0℃/min ramping rate in reducing atmosphere (5% H2 / 95% Ar). 105

Figure 6.6: Shrinkage profile of YSZ with 2.5, 5.0, and 7.5℃/min ramping between 1000℃ and 1350℃ in reducing atmosphere (5% H2/ 95% Ar). 106

Figure 6.7: Shrinkage rate for YSZ samples versus temperature with different sintering temperature profiles in reducing atmosphere. 107

Figure 6.8: Schematic showing sample geometry upon reaching sintering temperature and after dwell on sintering temperature for samples with 2.5, 5.0, and 7.5℃/min ramping rate. 109

Figure 6.9: Shrinkage profile of metal support samples sintered at 1350℃ in inert gas atmosphere (Ar) and at different ramping rates. 111

Figure 6.10: Shrinkage rate versus temperature for SS-430L samples sintered at 1350℃ in inert gas atmosphere. 111

Figure 6.11: Shrinkage profile for YSZ samples sintered at 1350℃ at different ramping rates in inert gas atmosphere. 112

Figure 6.12: Shrinkage rate vs. temperature for YSZ samples sintered at 1350℃ in inert atmosphere with different ramping rates. 113

Figure 6.13: SEM images of metal support sintered in reducing atmosphere (a and c), and in inert atmosphere (b and d). 115

Figure 6.14: a) SEM image of metal support sintered in inert atmosphere; b) EDX spectra of selected area in SEM image in ‘a’. 115

Figure 6.15: Refined sintering temperature profile for co-sintering of metal supported half-cells. 116

Figure 6.16: SEM image of a) 0.5CSDC surface of a SS-430L|0.5CSDC half-cell sintered at 1100℃ in reducing atmosphere and b) SEM image of PSDC surface of a SS-430L|PSDC half-call sintered at 1350℃ in inert atmosphere. 117

Figure 6.17: Optical image of a Metal Supported half-cell sintered in reducing atmosphere at 1350℃; a) Samples sintered without a scavenger, and b) samples sintered with a scavenger. 118

Figure 6.18: Optical image of co-sintered half-cell with a counter weight during sintering... 119

Figure 6.19: Cell structures tested in this study. 119

Figure 6.20: Cross-sectional SEM of a sintered MS-SOFC half-cell with structure 1 ‘Metal Support | 50/50 transition layer | 30/70 transition layer | Porous YSZ | Dense YSZ (electrolyte). 120

Figure 6.21: Cross-sectional SEM image of MS-SOFC sintered half-cell with structure 2 “Metal Support | 50/50 transition layer | Dense YSZ (electrolyte)”. 121

Figure 6.22: Cross-sectional SEM image of MS-SOFC sintered half-cell with the structure “Metal support | Porous YSZ | Electrolyte”. 122

Figure 6.23: Co-sintered MS-SOFC half-cells; a) cell had 30 wt% pore former in PYSZ layer, b) cell has 40 wt % pore former in PYSZ layer. 122

Figure 6.24: XRD spectra of anode powder made through heat treatment of anode catalyst solution (nitrate solution of Ni, Ce, and Sm). 123

Figure 6.25: TGA result for sintered metal support for the first anode burn-out cycle. a) Percentage mass change with temperature and time; b) Actual mass change with temperature and time. 124

Figure 6.26: a) SEM image of MS-SOFC half-cell infiltrated with NiO/SDC and heat treated at 400℃, b) SEM image of section circled in Figure 6.24a (electrolyte-electrode interface). 125

Figure 6.27: SEM image of electrolyte-transition layer interface. 125

Figure 6.28: EDX spectra of selected areas in Figure 6.25; a) EDX spectra of selected area 1, b) EDX spectra of selected area 2, and c) EDX spectra of selected area 3. 126

Figure 6.29: Picture of a MS-SOFC with anode and cathode catalyst. 127

Figure 6.30: SEM image of cross-section of MS-SOFC with sintered cathode. 127

Figure 6.31: a) Polarization curve of MS-SOFC tested at 700℃; b) Nyquist plot for the same MS-SOFC at 700℃ with 2.47 $mA.cm^{-2}$ current density. 128

Figure 6.32: SEM image of cross-section of MS-SOFC used in performance testing. The top layer is cathode, the middle layer is electrolyte, and the bottom layer is the 50/50 transition layer. 129

Figure 6.33: a) SEM image of anode catalyst before cathode sintering; b) SEM image of anode catalyst after operation. 129

Figure 6.34: a) SEM image of cathode surface before operation, b) SEM image of cathode surface after operation. 130

Figure B.1: Nyquist plot for 0.5 CSDC at 400℃……151

Figure B.2: Arrhenius plot for PSDC grain boundary conductivity……..152

List of Tables

Table 1.1: Comparison of different Fuel Cells (adapted from [11]). 7

Table 2.1: Summary of performance of MS-SOFCs with different anode materials [38,55,56]. 23

Table 2.2: Anode polarization resistance obtained from [59] at 650°C for different anode materials. 23

Table 2.3: Performance results for different anode materials used in MS-SOFCs at the Shanghai Institute of Ceramics Chinese Academy of Science. 26

Table 2.4: Common electrolyte materials and densification methods for MS-SOFC. 28

Table 2.5: Sinterability comparison of different cathode materials [92]. 32

Table 2.6: Performance comparison of infiltrated cathode catalyst (work from CAS Key Laboratory of Materials for Energy Conversion, Shanghai Institute of Ceramics, Chinese Academy of Sciences (SICCAS). 33

Table 2.7: Approximated values of ASR for different LSCrM cathodes calculated using ASR plots at 900°C [99]. 35

Table 4.1: Casting thickness of cell components. 63

Table 4.2: Details of chemicals used. 64

Table 5.1: Temperature profile used for dilatometry analysis. 74

Table 5.2: Ionic radii of cations in copper doped SDC [33][113]. 77

Table 5.3: Lattice constant for SDC with and without copper. 78

Table 5.4: Theoretical density of different samples 80

Table 5.5: Maximum shrinkage and temperature required to attain maximum shrinkage. 85

Table 5.6: Temperature above which grain boundary arc disappears. 89

Table 6.1: Composition of slurry for metal support. 96

Table 6.2: Preliminary slurry for transition layers and electrolyte. 96

Table 6.3: Base powder slurry for transition layers. 97

Table 6.4: Base powder slurry composition for electrolyte layer. 97

Table 6.5: Summary of important parameters from Figure 6.4-6.7 (reducing sintering atmosphere). 108

Table 6.6: Summary of key parameters from Figures 6.9-6.12. 113

Table A.1: Measured values of mass for porosity measurement……..150

Nomenclature

Roman Symbols

A	Surface Area (m^{-2})
C	Concentration
D	Diffusivity ($m^2.s$)
E	Cell Potential (V)
E_r	Reversible Cell Potential (V)
E_a	Activation Energy
F	Faraday's Constant (96487 $C.mol^{-1}$)
ΔG	Change in Gibbs Free Energy ($J.mol^{-1}$)
Δh	Enthalpy Change
I	Current (Amps)
I	Current Density ($Amps.cm^{-2}$)
J	Molar flux ($mol.cm^{-2}.sec$)
K	Boltzmann Constant (8.617×10^{-5} $eV.K^{-1}$)
l	Thickness (cm)
n	moles of electrons per mole of fuel
n_r	Second Law Efficiency
P	Power Density ($W.cm^{-2}$)
p	External Applied Pressure
q	Heat generated or absorbed (J)
R	Radius (cm)
R_{ee}	Electrode-Electrolyte Interface Resistance (Ω)
R_{gb}	Grain Boundary Resistance (Ω)
R_{gi}	Grain Interior Resistance (Ω)
R_T	Total Resistance (Ω)
s	entropy ($J.K^{-1}$)
T	Temperature (K)

t	Time (min)
w	work done (J)
w_{max}	Maximum work done (J)
Z	Impedance (Ω)
$Re\ Z$	Real Impedance (Ω)
$Im\ Z$	Imaginary Impedance (Ω)

Greek Symbols

δ_s	Entropy Generated
δw	Work Done
$\emptyset_{c,r}$	Reversible Cathode Potential
$\emptyset_{a,r}$	Reversible Anode Potential
$\emptyset_c$	Cathode Potential
$\emptyset_a$	Anode Polarization
γ	Surface Energy
A	Surface Area (m^2)
υ	Vibrational Frequency
λ	Distance between 2 adjacent planes
μ_v	Vacancy Chemical Potential
μ_a	Atom Chemical Potential
Ω	Molar Volume

Abbreviations

AFC	Alkaline Fuel Cell
ADIS	Analysis of Differences in Impedance Spectra
AFL	Anode Functional Layer
APU	Auxiliary Power Unit
ASC	Anode Supported Cell
ASR	Area Specific Resistance
BSCF	$Ba_{0.5}Sr_{0.5}Co_{0.8}Fe_{0.2}O_{3-d}$
BSE	Back Scattered Electrons
CGO	Cerium Gadolinium Oxide
CSC	Cathode Supported Cell
CTE	Co-efficient of Thermal Expansion
DBL	Diffusion Barrier Layer
D.C	Direct Current
D.G	Distributed Generation
DMFC	Direct Methanol Fuel Cell
DTU	Danish Technological University
EDS	Energy Dispersive X-Ray Spectroscopy
EIS	Electrical Impedance Spectroscopy
ESB	$(Bi_2O_3)_{0.7}(Er_2O_3)_{0.3}$-Ag

ESC	Electrolyte Supported Cell
FC	Fuel Cell
GDC	Gadolinium Doped Ceria
GNC	Glycine Nitrate Combustion
LBNL	Lawrence Berkeley National Laboratory
LBSM	$(La_{0.74}Bi_{0.10}Sr_{0.16})MnO_3$
LSC	$(La_{0.6}Sr_{0.4})_{0.99}CoO_{3-\delta}$
LSCM	$La_{0.8}Sr_{0.2}Co_{1-x}Mn_xO_{3-\delta}$
LSCrM	$La_{0.8}Sr_{0.2}Cr_{1-x}Mn_xO_{3-\delta}$
LSFC	$La_{0.58}Sr_{0.4}Co_{0.2}Fe_{0.8}O_{3-\delta}$
LSFNT	$La_{0.4}Sr_{0.4}Fe_{0.03}Ni_{0.03}Ti_{0.94}O_3$
LSFSc	$La_{0.6}Sr_{0.4}Fe_{0.9}Sc_{0.1}O_{3-\delta}$
LSGM	$La_{0.8}Sr_{0.2}Ga_{0.8}Mg_{0.2}O_{3-\delta}$
MCFC	Molten Carbonate Fuel Cell
MIEC	Mixed Ionic Electronic Conductor
MPD	Maximum Power Density
MSC	Metal Supported Cell
MS-SOFC	Metal Supported-Solid Oxide Fuel Cell
OCV	Open Circuit Voltage
PEM-FC	Polymer Electrolyte Membrane-Fuel Cell

PLD	Pulsed Laser Deposition
PSD	Plasma Spray Deposition
PVD	Physical Vapor Deposition
SBSC50	$SmBa_{0.5}Sr_{0.5}Co_{2.0}O_{5+d}$
SE	Secondary Electrons
SEM	Scanning Electron Microscopy
SFMO	$Sr_2Fe_{1.5}Mo_{0.5}O_{6-d}$
SOFC	Solid Oxide Fuel Cell
SS	Stainless-Steel
TFC	Topsoe Fuel Cell
TPB	Triple Phase Boundary
XRD	X-Ray Diffraction

Chapter 1 Introduction and Motivation

In the past 5 decades the world has seen an exponential increase in the demand of electrical power, with an increase in demand from 9,886 to 24,816 TWh between 1985 and 2016 [1]. To fulfill this steep rise in demand using conventional thermal power generation devices larger and larger amounts of fossil fuel are consumed. Conventional thermal power generation devices have low efficiencies, averaging 41% worldwide[2], and also contribute substantially to the emissions of greenhouse gasses leading to global warming. It has been reported that 17 of the 18 warmest years in the last 136 years occurred after 2001 [3]. In 2017 the Earth surface temperature was reported to be 0.9℃ higher than the average Earth temperature between the 1951 and 1980 [3].

These problems have driven research in developing new renewable energy technologies, and in developing power generation devices with higher efficiencies and lower greenhouse gas emissions. Amongst many others, fuel cells (FC) have been researched extensively as a solution for the past 50 years. FC is an electrochemical device which works by directly converting chemical energy of a fuel to electrical energy thereby having a higher electrical efficiency. There are several types of FCs, with solid oxide fuel cells (SOFCs) having the ability to operate with a variety of fuels including natural gas, renewable natural gas (RNG), bio-gas, hydrogen, etc. Hence, SOFC is an attractive technology to address current energy and environmental crisis and has been under development in the past 3 decades.

1.1 Fundamental of Fuel Cells

Fuel cells (FC) are electrochemical devices used to convert chemical energy of a fuel directly to electricity. The direct transformation helps attain higher efficiencies than heat engines due to lower energy losses during energy conversion. Since 1960s many different types of FCs have been developed:

1. Polymer Electrolyte Membrane Fuel Cell (PEM-FC).
2. Alkaline Fuel Cell (AFC).

3. Direct Methanol Fuel Cell (DMFC).
4. Phosphoric Acid Fuel Cell (PAFC).
5. Molten Carbonate Fuel Cell (MCFC).
6. Solid Oxide Fuel Cell (SOFC).

Essentially, all FCs are made of three primary components; anode, electrolyte, and cathode. All three components have specific electrochemical functions to perform. Anode is responsible for the electrochemical oxidation of fuel molecules, cathode is responsible for the electrochemical reduction of the oxidant molecules, and electrolyte bridges the anode and cathode to complete the circuit. The main role of electrolyte is to transport either anions or cations to the opposite electrode depending on the type of FC. By direct electrochemical oxidation and reduction leading to production and transportation of electrons FCs avoid energy transformation steps, which are inherent in conventional thermal power generation systems. This leads to higher efficiencies of the system making this technology more attractive.

1.1.1 Working of a Fuel Cell

The reactions taking place at the electrodes (anode and cathode) are commonly known as half-cell reactions. For instance, in the case of SOFC with hydrogen as fuel, the anode reaction is:

$$H_2 + O^{2-} \rightarrow H_2O + 2e^- \qquad \text{R-1.1}$$

The reaction at the cathode, in turn, is:

$$\frac{1}{2}O_2 + 2e^- \rightarrow 0^{2-} \qquad \text{R-1.2}$$

And the overall reaction is:

$$H_2 + {}^1/_2\, O_2 \rightarrow H_2 0 \qquad \text{R-1.3}$$

Depending on the type of FC, these reactions can take place at different temperatures, for instance in the case of SOFC the operating temperature is normally kept between 700-900℃ to allow for sufficient electrolyte conductivity. Regardless of the operating temperature, the overall performance is governed by thermodynamic and kinetic principles. The maximum work attainable

through a FC is equivalent to the Gibbs free energy of a particular full cell reaction. In the above case it will be the Gibbs free energy of the hydrogen reaction with oxygen. Using the first and second law of thermodynamics, equations for net heat generated/absorbed and work done by the system can be formulated as:

$$q = T\Delta s - T\delta_s \qquad (1.1)$$

$$\delta w = -\Delta G - T\delta_s \qquad (1.2)$$

where 'q' is the heat generated or absorbed, 'T' is the absolute temperature of the system, 's' is the entropy of the system, 'δ_s' is the entropy generated due to irreversibilities, 'δw' is the work done and 'ΔG' is the Gibbs free energy. The equation for work done is basically the electrical work done by the system. This electrical work is made from two components including the reaction term as change in Gibbs free energy and the entropy generation term. For maximum work, the generation of entropy equals zero; under this condition the work done becomes the work done under reversible conditions. It should be noted that reversible work cannot be achieved in reality. However, it can be used as a standard to rate the performance of a fuel cell since the work done in that case is the maximum work done (Equation 1.3).

$$w_{max} = -\Delta G \qquad (1.3)$$

An ideal fuel cell is arbitrarily taken to be a fuel cell running on hydrogen without any irreversibility. This is the standard hydrogen fuel cell and the reversible potential given from this cell is taken as the standard mark. Below is the calculation for evaluating reversible cell potential. The reversible cell potential is the electrical potential generated when a fuel cell works under completely reversible conditions. It is appropriate to express this work done in term of potential difference or the electromotive force as it better correlates to the output of a fuel cell. The electrical energy output, E, from a fuel cell is defined as the potential energy equivalent to the work done (J) in moving a unit charge (C) through an electrical field. This has the units of Volts (V) and the fuel cell potential is the potential difference between the cathode and anode potential (Equation 1.4).

$$E = \frac{\delta w}{nF} \qquad (1.4)$$

where ‘δw’ is the work done, ‘n’ is the number of moles of electrons released per mole of fuel and F is the Faradays constant (F = 96487 C/mole electron). The maximum potential (or reversible cell potential), E_{max} can be determined as:

$$E_{max} = \frac{w_{max}}{nF} = \frac{-\Delta G}{nF} \qquad (1.5)$$

Like any other energy conversion device, fuel cells are limited by the second law of thermodynamics to a maximum efficiency only attainable in case of reversible operation. This efficiency (η_r) is labeled as the second law efficiency and can be calculated through

$$\eta_r = \frac{\Delta g}{\Delta h} \qquad (1.6)$$

As changes in Gibbs free energy and enthalpy are functions of temperature, the efficiency of a fuel cell also depends on temperature. In most cases the efficiency decreases with increasing temperature because the change in entropy increases. Other losses in fuel cell performance occur due to irreversibility in the system, such as incomplete reactions. However, since a fuel cell does not operate within a temperature range like conventional power production units, the efficiency of a fuel cell, in purely ideal terms, is higher than that of conventional thermal power generation device.

The study of thermodynamics of a fuel cell is important to assess the maximum performance possible. However, the study of kinetics of a fuel cell gives details about how fast and how much current can be produced. It also gives insight into the actual reaction pathways or mechanism, as well as providing qualitative and quantitative analysis of losses occurring during actual working conditions. In a fuel cell electrochemical reaction takes place at both electrodes and hence there is an associated potential with the electrodes. This potential is referred to as the anodic and cathodic potentials. The overall cell potential, E_r, is the difference between the cathode potential and the anode potential.

$$E_r = \emptyset_{c,r} - \emptyset_{a,r} \qquad (1.7)$$

where $'\emptyset_{c,r}'$ and $'\emptyset_{a,r}'$ are the reversible cathode and anode potentials, respectively. The overall reversible cell potential ‘E_r’ represents the voltage generated when the fuel cell runs reversibly,

that is without any extraction of current and without any other losses. The actual overall cell potential can then be defined as:

$$E = \emptyset_c - \emptyset_a \qquad (1.8)$$

where $'\emptyset_c$, and $'\emptyset_a'$ are the actual cathode and anode potentials, respectively. Using Eqs. 1.7 and 1.8 the overpotential associated with a fuel cell can be calculated (see Eq. 1.9).

$$\eta = E_r - \mathrm{E} \qquad (1.9)$$

Using eqs. 1.7-1.9, anode and cathode overpotentials can also be defined. It can be shown that the actual potential is the difference between the reversible overall cell potential and the sum of all the overpotentials. Normally, irreversibility in a cell increases the anodic potential and reduces the cathodic potential, thus decreasing the overall cell potential. Therefore, the anode overpotential is always positive and the cathode overpotential always negative.

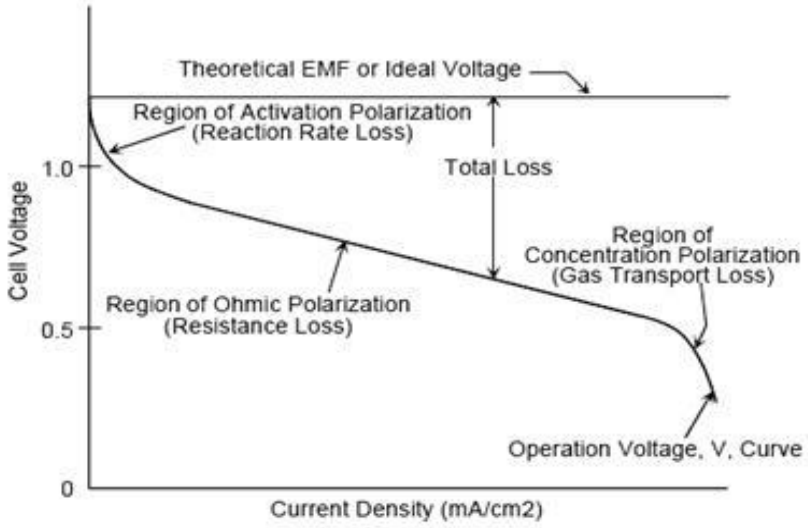

Figure 1.1: Ideal and actual fuel cell voltage/current characteristics [3].

The three major types of overpotentials are activation, ohmic and concentration overpotentials. Figure 1.1 shows voltage and current density relation and depicts the region where these losses occur. Among these, the activation and concentration overpotentials can be explained by studying the kinetics of a fuel cell, however, ohmic overpotential requires the study of transport

phenomenon in the fuel cell. Activation overpotential is the loss in cell potential due to activation energy required to start the reaction; that means that a certain amount of cell potential is used up in crossing the energy barrier associated with electrode reactions. Hence, when a current is drawn a small but steep decrease in cell voltage is seen at low current densities.

The transport of species involved in a fuel cell operation is also very important. The rate at which reactants are supplied to the reaction active sites and the rate at which the products are removed is critical to maintaining a constant production of electrical power. For instance, in case of large current density (high rate of consumption for reactants) the supply of reactant limits the overall process. In extreme cases, the supply of reactants is slow compared to the current produced, and, hence, because of shortage of reactants, the current might rapidly decline to zero. The value of current density drawn for this to happen is called the limiting current density. Losses happening due to insufficient supply of reactants or mass transfer limitations are known as concentration overpotential and can be studied and optimized through a study of transport phenomena in electrodes.

Similarly, the transport of charged species through the electrolyte governs the overall system performance. Charged species, preferably ions rather than electrons, move through the electrolyte to complete the electrochemical reaction and form a closed circuit. The flow of charged species happens under the influence of a charge gradient. Conductivity, transport of ions, is used as a characterization parameter for electrolyte selection. Governing equations pertaining to mass, energy and momentum coupled with Fick's law of diffusion can be used to study the transport of these species in electrodes and the electrolyte.

1.1.2 Types of Fuel Cells

There are different types of fuel cells, depending on the choice of electrolyte. Even though the working principle remains the same, the type of charge the electrolyte transports is different for different fuel cells. The choice of electrolyte also governs the operating temperature of these fuel cells. Below is a list and brief description of the main types of fuel cells.

1. Solid Oxide Fuel Cells (SOFC):

Solid oxide fuel cells use ceramic metal oxides, commonly doped zirconia and ceria, as the electrolyte to transport negative oxygen ions. Since these are ceramic oxides, their operating temperatures are in the range 600-1000°C to sustain sufficient ionic conductivity.

2. Molten Carbonate Fuel Cells (MCFC):

   MCFC uses a mixture of lithium and potassium carbonate to transport negative carbonate ions. Similar to SOFCs, higher conductivity is achieved at high temperatures. The usual operating temperatures are around 600^{o}C.

3. Polymer Electrolyte Membrane Fuel Cell (PEMFC):

   As goes by the name PEMFC uses a polymer electrolyte which can transport ions with positive charge. Hydrogen ions are transported through the electrolyte in this case. These fuel cells normally use an acidified polymer film to conduct the protons. Their normal operating temperatures fall in the range of 70 to 90^{o}C.

4. Phosphoric Acid Fuel Cells (PAFC):

   PAFCs also transport protons through the electrolyte. The direction is from anode to cathode. As suggested by the name, normally phosphoric acid is used as the electrolyte. Normal operating temperature ranges between 115 and 205^{o}C.

5. Alkaline Fuel Cells (AFC):

   AFCs transport negative hydroxyl ions through the electrolyte; hence the electrolyte is an alkaline solution normally. The most common choice is potassium hydroxide. These cells operate in the range of 100-220^{o}C.

Based on the above definition the most prominent feature of MCFC and SOFC is that they do not specifically need hydrogen as fuel. They show higher fuel flexibility when compared to others. The comparison of all these types of fuel cells is shown in Table 1.1.

Table 1.1: Comparison of different Fuel Cells (adapted from [11]).

	PEMFC	PAFC	MCFC	SOFC
Type of Electrolyte	H^+ ions (with anions bound in polymer membrane)	H^+ ions (H_3PO_4 solutions)	CO_3^{2-} ions (typically molten $LiKaCO_3$ eutectics)	O^{2-} ions (Stabilized ceramic matrix

				with free oxide ions)
Common electrolyte	Solid polymer membrane	Liquid phosphoric acid in lithium aluminum oxide matrix	Solution of lithium, sodium, and/or potassium carbonates soaked in a ceramic matrix	Solid ceramic, Yttria stabilized zirconia (YSZ), Doped Ceria
Typical construction	Plastic, metal or carbon	Carbon, porous ceramics	High temperature metals, porous ceramic	Ceramic, high temperature metals
Internal reforming	No	No	Yes, good temperature match	Yes, good temperature match
Oxidant	Air to O_2	Air to Enriched Air	Air	Air
Operational Temperature	150-180°F (65-85°C)	302-392°F (150-200°C)	1112-1292°F (600-700°C)	1202-1832°F (700-1000°C)
DG system level efficiency (%HHV)	25 to 35%	35 to 45%	40 to 50 %	45 to 55%

Solid oxide fuel cells (SOFC) are a type of FCs which can operate with a variety of different fuels, making SOFC a more viable and practical choice. They are also competitive when it comes to conversion efficiency (Table 1.1). SOFC is an all solid device made from special rare earth metals and metal oxides. These solid materials demonstrate electrochemical properties, in that they can conduct and transport charge species (ions and electrons) and promote electrochemical charge transfer reactions for the generation of electricity. These materials are only active at sufficiently

high temperatures, in the range of 700-1000°C. This means that SOFC is a device which operates at high temperatures and can be coupled with heat recycling for even higher efficiencies. This makes SOFC a popular choice for research globally.

1.2 Fundamentals of Solid Oxide Fuel Cells

The first fuel cell was created in 1838 by the English scientist, William Groove, and was named after him as the "Groove Cell"[4] . Since then, tremendous work has been done in the development and realization of this technology, with major contributions from Guagain, Nernst and Wagner in the field of SOFCs. In 1859 Guagain [5] made the discovery of 'solid electrolyte' followed by Nernst [6] who reported that 15 mol% Yittria stabilized with Zirconia supports ionic conductivity in 1899. Later in 1943 Wagner showed that doped oxides show ionic conductivity through oxygen ion vacancy hoping mechanism, where oxygen ions jump through the vacancies in the crystal structure of a doped oxide solid solution [7]. This phenomenon of vacancy hoping in solid solutions of doped oxides was later investigated for use in SOFC. Keeping this in mind, many patents were filled between the period of 1960-70 regarding oxygen conduction through thin ceramic oxide films, which showed appreciable performance at high temperatures of 1000^{o}C [8]. A simplified schematic of SOFC is shown in Figure 1.2.

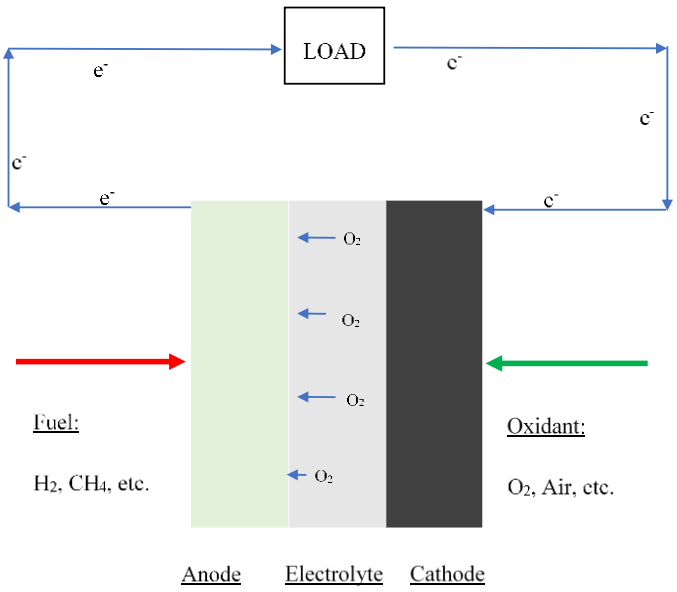

Figure 1.2: Schematic of a Solid Oxide Fuel Cell.

There are three sub kinds of SOFCS; Anode Supported Cells (ASC), Electrolyte Supported Cells (ESC) and Cathode Supported Cells (CSC). Although the choice of support, the component which is left thicker, depends on the application, commonly ASCs are the most popular choice. This is because of cell performance optimization. Since electrolyte is only liable for charge conduction, the thinner it is the lesser the resistance faced in the transport which ultimately leads to lower energy or cell potential loss. Since cathode shows a higher resistance to charge transfer reactions than anode, thin cathodes are preferable. The conventional structure, ASC, and operating conditions of a SOFC cause several problems pertaining to both cell life and performance.

1.3 Motivation

Limitations with SOFC can be divided into three categories; i) wear and tear of cell because of cell operation, ii) problems associated with cell component materials (reactivity of cobalt containing cathode with YSZ, grain coarsening of nickel containing anode, etc.), and iii) cell's structure. Firstly, the operating temperature, being in the range of 700-900°C, can lead to cell wear and tear in many ways. Apart from inducing high capital costs it also causes prolonged start-up time for pre-heating requirements. Figure 1.3 shows the requirements and limitations of cell components operating at these high temperatures.

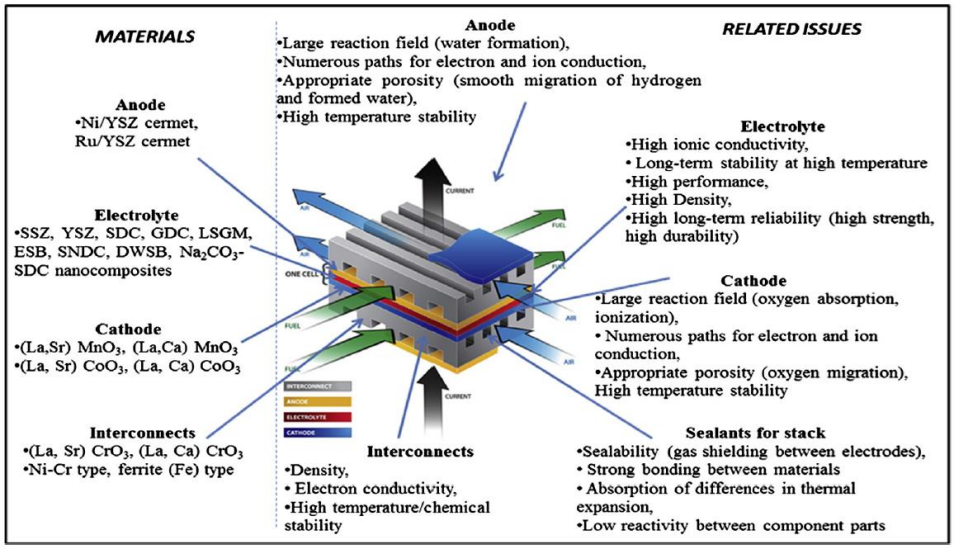

Figure 1.3: Material limitations for SOFC [6].

At these high temperature, nickel, the active anode catalyst, starts to sinter slowly [9,10] leading to agglomeration and coarsening of grains. The coarsening of nickel particles can lead to reduction in Triple Phase Boundary (TPB) which reduces the area available for electrochemical reactions and hence causes degradation[11]. Secondly, the choice of material can lead to chemical and physical changes in the cell structure leading to low cell life and decreased performance over time. Conventionally, nickel oxide mixed with common electrolyte materials (Yittrium Stabilized Zirconia (YSZ), Samarium Doped Ceria (SDC)) has been used as the anode material [12]. The choice of nickel is because of its high catalytic activity towards electrochemical oxidation of fuel molecules, and also because it is an active catalyst towards internal reforming of carbon fuels allowing for fuel flexibility in SOFCs. The use of a mix of nickel oxide and SDC as the anode and structural support comes with a problem. Prior to operation nickel oxide is reduced to activated nickel, as nickel is active towards the desired reactions opposed to nickel oxide. The reduction and oxidation reaction of NiO and Ni are given below.

$$NiO + H_2 \rightarrow Ni + H_2O \qquad \text{R-1.4}$$

$$Ni + \tfrac{1}{2}O_2 \rightarrow NiO \qquad \text{R-1.5}$$

The above two reactions are exothermic, but the difference in magnitude of energy released is significant. Reduction reaction has a net enthalpy of -13 kJ.mol^{-1} and the net enthalpy for oxidation is -239.8 kJ.mol^{-1}. This can lead to a thermal shock in the cell structure and is also a cause of cell degradation caused by reduction-oxidation cycle [13]. The continuous oxidation and reduction, commonly known as redox cycling, also leads to a large volume change in the support layer which can induce damage to the structure. In cases where there is fuel shortage or fuel cut off nickel can be oxidized back to nickel oxide gaining 69.2% volume as compared to bulk nickel [14]. Since the materials used are metal oxides and ceramics, which are brittle in nature, the integrity of the cell is compromised during redox cycling while in operation. Waldbilig et al. [15] have done extensive work on cell failure due to redox cycling in which the anode was made of nickel oxide mixed with either YSZ or SDC. Figure 1.4 shows a SEM image of the cross-section of an (ASC) after redox cycling. It is evident in the figure that because of stresses in the anode, caused by redox cycling, the electrolyte cracked.

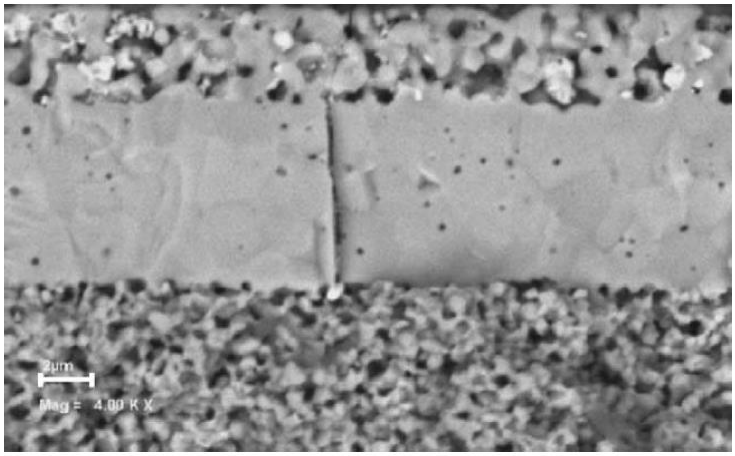

Figure 1.4: SEM image of cross section of an Anode Supported Cell (ASC) with a vertical crack passing through the electrolyte layer [15].

Considerable research has been conducted to better understand redox cycling at the anode and to develop ways to mitigate this problem [16–18]. However, it has been reported that anode redox cycling is the major failure mechanism for ASCs [14,19].

Thermal cycling, which is fast heat up and cool down of a cell also contributes to cell failure. It has been reported that ceramics, materials used in SOFC, undergo racheting (common in metals) where the properties of the material change due to plastic deformation at high temperature [12]. In the case of SOFCs it has been reported that cermet anode made of Ni/YSZ experiences an increase in its Coefficient of Thermal Expansion (CTE) during these cycles which leads to stresses in the support layer [20]. This change in CTE leads to an aggravated thermal expansion mismatch between different components of SOFC which can cause cell cracking and delamination. In summary, most of the problems associated with conventional SOFCs are related to low structural integrity caused by operating conditions and choice of materials.

To cater for these problems, in the past two decades, a new type of SOFC has been under development, which is Metal Supported-Solid Oxide Fuel Cell (MS-SOFC). These cells are also being labelled as the third generation SOFCs. Essentially, the support layer is made of metal and all other components; anode, electrolyte and cathode are deposited on it. Figure 1.5 shows a comparison between ASC and MS-SOFC.

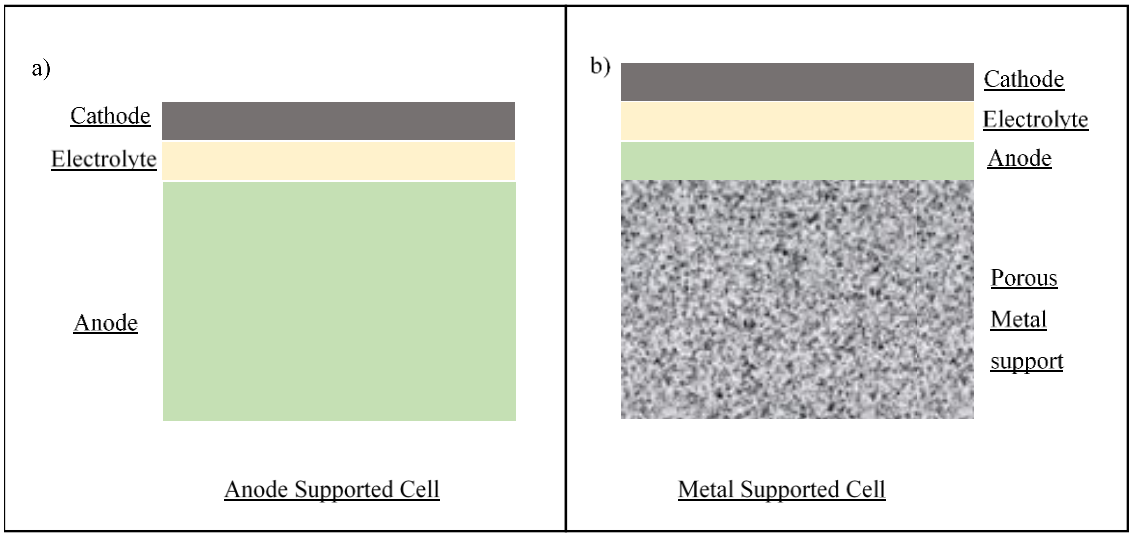

Figure 1.5: Schematic of a) Anode Supported Cell (ASC) and b) Metal Supported Cell (MS-SOFC).

In this type of cell, the porous metal layer acts as the mechanical support of the cell and can also acts as the interconnect in cell stacks. Researchers have used different materials (Alloys) as metal support but the most popular choice remains stainless steel. The addition of metal as a support can help introduce tolerance to redox and thermal cycling to the entire cell structure. In addition, it also provides cells with more ruggedness hence making it possible to use SOFC in portable applications where the system might go through physical shocks [21]. Further, it also allows for use of thinner active layers which reduces the overall ohmic resistance in the cell.

The idea of MS-SOFCs, however, is not new; the first rounds of research date as far back as 1960s when zirconia was used as the electrolyte with austenitic stainless steel; the recorded performance for this cell was 115 $mW.cm^{-2}$ at 750°C [22]. Over time, researchers tried using special alloys like NiCrAlY and $CrFe_5Y_2O_3$ [23]. Even though work in this type of cells took a faster pace in early 2000s there is still a lot to cover to completely understand and perfect both the manufacturing and operation of these cells. A significant number of research groups rely on the use of techniques like Plasma Spray Deposition (PSD) and Pulsed Laser Deposition (PLD) for the manufacture of these cells. In these methods, ceramic layers (especially the thin dense electrolyte layer) are deposited on a pre-manufactured porous metal substrate. However, it has been reported that electrolyte deposited using thermal spray deposition methods is not fully dense leading to cell inefficiencies

[24,25]. Similarly, the use of plasma spray deposition can lead to localized hot spots on the substrate which can cause physical defects like warping and cracking [26]. It was only in the late 1990s and early 2000s that wet ceramic processing techniques like tape casting were deemed useful in the manufacture of MS-SOFCs [27],[28]. In this method, cell components are casted in layer form, stacked together and co-sintered for bonding at high temperatures. One of the prominent features of this method is the higher electrolyte densifications can be reached. However, there are several challenges associated with the use of this technique to fabricate MS-SOFCs.

Since the components of the cell fall under different material categories (metal support is a metal, and electrolyte is a metal oxide ceramic), there is a mismatch in shrinkage behaviors of these components under conventional sintering profiles. This mismatch can lead to cell cracking, warping, and layer delamination during co-sintering [29]. Similarly, the use of metal also puts a limitation on the choice of the electrolyte material; for example, cerium (IV) tends to reduce to cerium (III) in reducing atmospheres at high temperature, rendering co-sintering of SDC with metal support difficult [30]. Further, use of reducing atmosphere can create problem with cathode sintering because cathode is a perovskite which can reduce under reducing atmosphere. Even though many research groups use tape casting and co-sintering to fabricate MS-SOFCs, there are little data published related to the specifics of this fabrication method. It is clear that most of the associated challenges are related to the materials used. Hence, a better understanding of material properties, especially shrinkage behavior, can help further optimize tape casting and co-sintering to fabricate MS-SOFCs with SDC and YSZ as electrolyte.

SDC shows a higher conductivity than YSZ at lower temperatures. This means that using SDC as electrolyte with MS-SOFC can reduce the operating temperature and hence wear and tear of the cell during operation. However, as mentioned above, ceria (IV) oxide tends to reduce to ceria (III) oxide in reducing atmosphere at high temperatures. One solution might be to lower the sintering temperature of SDC which might mitigate the extent of reduction and hence distortion in ceria crystal lattice. In the past, several methods have been tried for lowering sintering temperature, with the use of sintering aid being labelled as the most effective [31]. It has been reported that copper acts as an effective sintering aid with small effect on the electrochemical properties of GDC [32]. Even though copper has already been identified as an effective sintering aid, all published works use more than 1.0 mol% doping of copper with GDC [33,34] or SDC [31]. Too high copper content

affects the ionic conductivity, and thus it is critical to study lower copper content (below 1.0 mol%). Once the effect of copper is fully characterized, copper co-doped SDC may be used as electrolyte in MS-SOFCs. Copper co-doped SDC and SS-430L can be tape casted. The casted Layers of SS-430L and copper co-doped SDC can then be stacked and co-sintered at a lower co-sintering temperature (e.g. 1100°C) in reducing atmosphere. Hence, the first objective of this research was to use copper as a sintering additive with SDC and to fully characterize the effect copper has on physical and electrochemical properties of SDC. Of particular importance is the effect on shrinkage profiles and conductivity.

To successfully use co-sintering to fabricate MS-SOFCs, it is critical to understand the shrinkage behavior of cell components. Different cell components behave differently when heated under a particular sintering profile; if the shrinkage behavior of these components is not similar it can lead to physical defects. However, the shrinkage behavior of a particular material can be slightly tuned by changing the dynamics of the sintering temperature profile. For instance, different ramping rates during sintering to same final temperature may show different shrinkage profile for same material. In the case of MS-SOFC, it is desirable to co-sinter at least the metal support and electrolyte together. Having a deeper understanding of the shrinkage behavior of metal support (ferritic stainless steel 400 series here) and electrolyte (YSZ and SDC) will help achieve defect free (no cracks, warping, or delamination) co-sintered half-cells with desirable qualities (metal support porosity, cell component thickness, electrolyte layer density, etc.). Hence, the second objective of this research is first to study the shrinkage behavior of ferritic stainless steel 400 series, YSZ, and SDC and second to study the co-sintering of half-cells.

1.4 Organization of Thesis

Chapter 1 is an introduction to the research work presented in this thesis and also gives the motivation for why the work was done. Chapter 2 gives out the literature review pertaining to both sub-projects. The first section of chapter 2 summarizes the work that has already been done in the field of MS-SOFCs. This includes details about materials used and cell structures. The second section of chapter 2 gives out details about the work done on the use of sintering aid for SDC as electrolyte. Chapter 3 pertains to the general theory of sintering which is an important aspect of this research. In both, lowering the sintering temperature of doped ceria and in co-sintering of MS-

SOFC cell components, it is important to understand the theoretical principles of sintering to later tune sintering profile for our purpose. Chapter 4 describes the experimental approach to achieve both objectives. Other than giving out the experimental plan, Chapter 4 also explains why certain experiments are necessary for this research and also discuss the underlying theory behind Electrochemical Impedance Spectroscopy (EIS) for the determination of conductivities. Chapter 4 also describes some analytical equipment used in the research like SEM, XRD etc. The exact experimental procedures for sample preparation and testing, however, are given in the result chapters (Chapters 5 and 6). Chapter 5 gives out the results of using sintering aid (copper) with SDC. In it, results pertaining to crystal structure, morphology of sintered samples, sintering dynamics of samples, and electrochemical properties are discussed. Chapter 6 presents and discusses the results of fabrication of MS-SOFC using tape casting and co-sintering method. It primarily gives the results of experiments performed in order to fabricate MS-SOFC which can be tested for performance. Chapter 7 gives out the conclusions and recommendations for future work.

Chapter 2 Literature Review

2.1 Metal Supported Solid Oxide Fuel Cells

Interest in third generation SOFCs has its roots deep in the mid twentieth century. The first attempts at MS-SOFC date in 1960s when austenitic steel was used as a support with Zirconia as electrolyte [22]. However, after this there was not much research reported until mid 1990s. This was because SOFCs at that time were still in embryonic stages and a lot of work was being directed towards materials which might perform better electrochemically. As stated previously using metal as the support comes with numerous advantages as delineated by Tucker [21], such as:

1. Reduction in material cost. Most of the support material in conventional cells like ASC, ESC or CSCs is replaced by cheaper metal.
2. Metal as support enhances the tolerance to thermal cycling and to redox cycling.
3. It makes a cell more robust and more viable for portable applications where the cell might go under physical shock.
4. It also helps reduce the resistive losses during operation by allowing the use of thin-films of all functional ceramic layers.

Since 1990s a few research groups have taken up work in the field of MS-SOFCs, with major research being done by Lawrence Berkeley National Laboratory (LBNL), Ceres Power, Riso National Laboratory, Forschungszentrum Julich, Danish Technological University (DTU), Topsoe Fuel Cells (TFC), DLR, Plansee, and the University of Toronto [35]. Groups from Korea and China have also made contributions to the development of MS-SOFCs. The addition of metal to an originally full ceramic cell creates problems due to the mismatch of material properties and these problems arise in manufacturing and during operation. Major issues with the use of metal as a support are:

1. The choice of metal to be used. Since the metal comes in contact and binds to the ceramic components, it should have physical properties similar to those of ceramics. During operation the cell is heated to high temperatures and the CTE of all components should be similar to avoid cracking or delamination of cell layers [36].

2. Co-sintering of metal support with ceramic layers (Anode Functional Layer (AFL), electrolyte, etc.) is difficult to design. Metal cannot be sintered in ambient atmosphere at conventional SOFC electrolyte sintering temperatures (1350-1500℃) [35]. Temperatures above 1200℃ can lead to physical deformation of the support; for instance it has been reported that high temperature sintering of metal support with NiO can lead to inter-layer diffusion of chromium and nickel [37].
3. Most cathode materials (mostly doped metal oxides) require oxidizing atmosphere during sintering. With metal as the support, this becomes a hurdle as metal, especially ferritic stainless steel, cannot undergo high sintering temperatures in oxidizing atmospheres. Incorporation of cathode is one of the major challenges in the development of MS-SOFCs at this stage [35].
4. Morphological changes in the metal support during operation. These are basically both physical and chemical changes where the metal grains deform (coarsen, migrate etc.); chromium migrates from the alloy structure towards functional anode or in the case of fuel cut makes chromium oxide.

All above stated issues can be categorized into two broader categories; one where the source of problem is the type of material used, and second where degradation of cell takes place during manufacturing and operation. The present literature review includes a history of what has been accomplished in the past two decades and highlights the remaining issues. For clarity, the review is divided into separate sections conforming to the major problems in the commercialization of MS-SOFCs. As of now there are four major aspects on which R&D is being carried out:

1. Choice of metal to be used as substrate. Even though the most common choice of metal is stainless-steel, researchers are also studying other metals and alloys for the purpose of support in a MS-SOFC.
2. Material to be used in MS-SOFC as the electro-catalysts. Researchers have tried a variety of anode and cathode catalyst materials. The electrochemical performance is usually measured in terms of open circuit voltage (OCV), polarization curves, stability over time, etc. and on the short term (during manufacturing) and long term (during operation) interaction of these materials with the metal support.

3. Structure of the cell. Apart from the four primary components (metal support, anode, electrolyte and cathode), researchers have worked on the effects of adding additional layers to act as barrier layers. These are done in part to solve the problem of interaction between components of the support and other layers.
4. Fabrication techniques for MS-SOFCs. There are several ways to fabricate MS-SOFC, including Plasma Spray Deposition (PSD), Pulsed Laser Deposition (PLD), Magnetron Sputtering, and tape casting. Details, however, of fabrication techniques are commonly left out of published works.

This review will first give out details about the metal materials which have been tried up till now and the most common choice based on performance. Then, the review will give out details of electro-catalyst materials for use in MS-SOFC. At the end, an overview of cell structures fabricated using tape casting and co-sintering is given.

2.2 Materials used in MS-SOFC

It was described earlier that a typical SOFC is made of at least three components, which increases to four in the case of metal supported solid oxide fuel cell. These components work together to produce electrical current, hence their compatibility with each other is vital. A schematic of MS-SOFC is shown in Figure 1.5.

2.2.1 Material for metal support

Over time several metals have been tried in MS-SOFCs. The selection criteria include:

1. Compatibility with other SOFC materials, especially during heat-up and cool down.
2. High resistance towards oxidation.
3. High resistance to thermal cycling.
4. High electrical conductivity.
5. Cost of material

Based on above requirements ferritic stainless steel has been used extensively as metal support (MS). Firstly, the CTE of Stainless-Steel (SS) 430L, in the range of 10-12 $ppm.K^{-1}$, matches closely to that of SDC and YSZ (also 10-12 $ppm.K^{-1}$) [21]. Secondly, it contains 16-18% Cr which

can form an electrically conductive protective coating of chromium oxide [35]. Thirdly, it is one of the cheaper options relative to the use of special alloys like Hastelloy X, NiCrAlY, etc.[35]. Therefore, SS-430L has become one of the most common choices to act as metal support [38–40]. Xia et al. [41] used SS-430L in their MS-SOFCs and reported a maximum power density (MPD) of 246 $mW.cm^{-2}$ at 700℃. However, some reports have also suggested against the use of SS-430L; for instance, an early study [42] showed that 16-18% Cr content is not enough to form a protective coating against oxidation when SS-430L was used as metal support for SOFC application. Even though SS-430L has been successfully incorporated in MS-SOFCs, there are still some gaps in the complete understanding of its oxidation behavior, especially under fuel side conditions (mostly humidified H_2 at 600-800℃). Although chromia scale is conductive, it is still the least conductive path between electrolyte and current collectors [35], which can somewhat increase the ohmic resistance of the entire circuit. Similarly, after a certain amount of oxidation, chromia can lead to spalling of SS-430L structure which leads to disconnected electrical paths [21]. It has been reported that a 5 micron thick layer of chromia is the threshold after which SS-430L starts to spall [28]. In [28], Tucker reported that in a 1200 hour long operation, SS-430L MS on the cathode side (air) showed a chromia scale of approximately 0.9 micron thickness. With similar growth kinetics it was concluded that the cell could run for 30,000 hours before spalling occurs. Another problem with ferritic stainless steel is the presence of silicon and aluminium. Both of these can form non-conductive oxides during operation. It has been reported previously that even 0.017 wt% Si will oxidise in stainless-steel [43].

Similar to SS 430L, other Fr-Cr alloys like crofer 22 APU, and 22 H have also been used as metal support. Both have chromium in the range of 20-24 wt% which provides a better oxidation resistance. As a comparison, the area specific resistance (ASR) of crofer 22 APU (0.02-0.03 $ohm.cm^2$) during a 200 hour exposure to air at 800℃ [44] was less than that of SS-430L (0.1 $ohm.cm^2$) after 30 hours exposure to air at 800℃ [42]. Sarasketa-Zabala et al. [45], studied the oxidation of crofer 22 APU in 50% humidified hydrogen at 800℃. They reported that chromia scale growth occurs during the first 500 hours of operation after which there is a very small growth in chromia scale thickness up to 4500 hours. The scale thickness at 3000 hours of operation was only 1.6 microns.

Other than iron-based materials, a lot of research has been focused on nickel-based materials. The choice of using nickel as the primary component is obvious since it is the most common anode electro-catalyst for SOFCs. However, there is a considerable mismatch in CTE of just nickel and most of the electrolyte materials; for instance it has been reported that the CTE of nickel is 16.5 $ppm.K^{-1}$ compared to 12.4 $ppm.K^{-1}$ for GDC [35]. This presents a major problem during cell heat-up and cool down, as well as during sintering. One way of lowering this CTE is by alloying nickel with another metal, like iron [21].

Iron has been used as the most common alloying metal with nickel metal support. Ishihara et al. [46] has done extensive work on the use of Ni-Fe alloy and concluded that 10wt% Fe gives the best performance. Molybdenum has also been used with nickel to act as metal support for SOFCs [47], [48]. High MPDs have been reported in this case; for instance, 1.196 $W.cm^{-2}$ at 750°C and 0.6 V. Further, nickel with chromium in the form of IN625 [49] alloys (Ni22Cr) and PI600 [50] (Ni:Cr:Fe = 74:16:9 wt%) have been studied at Gdansk University of Technology in Poland. They reported that addition of yittrium in the form of a protective coating, can increase the oxidation resistance substantially. Samples of PI600 without yittrium protective coating showed an increase 13 wt% in mass compared to only 2 wt% in samples which were coated with yittrium.

2.2.2 Anode

The anode is mainly responsible for facilitating electrochemical oxidation of fuel and transport of electrons to the outer circuit. The most common choice for anode electro-catalyst has been nickel [51]. Nickel is active towards the electrochemical oxidation of fuel and also acts as a catalyst in internal reforming of carbon containing fuels. However, common anode electro-catalyst is not only made of nickel, rather it contains a mixture of nickel with SDC or YSZ. The reason for adding SDC or YSZ to the anode substrate is twofold: 1) it increases the Triple Phase Boundary (TPB) of the cell and 2) it helps match the CTE of anode to that of electrolyte. Matching CTE is important so that anode and electrolyte show similar thermal expansion/compression behavior and do not crack during operation. For instance, it is reported that Yittrium Stabilized Zirconia (YSZ) and SDC have CTEs in the range of 10-12 $ppm.K^{-1}$ and that of nickel is 16.5 $ppm.K^{-1}$ [21]. This difference in CTE can lead to cell warping or layer delamination during heat up and cool down to high temperature operation, and during cool down from sintering. This is just one limitation

associated with the use of nickel as anode. With MS-SOFCs, several other problems arise which are discussed below. Hence, it is not uncommon to see a variety of combinations of anode materials being used in these kinds of cells.

The primary problem with the use of nickel containing anode electro-catalyst in MS-SOFC (MS on anode side) is the interlayer diffusion of Ni and Cr [52][53]. Chromium diffusing into the anode layer can form chromia scale on the active sites, increasing the anode polarization resistance [53]. In the same way, nickel diffusing into steel can lead to microstructural changes in steel (ferrite stainless steel changes to austenite upon reaction with nickel) [54]. Austenitic steel has different CTE than ferritic steel which can lead to physical damages to the cell during heat up and cool down. However, nickel still remains the most popular choice as anode electro-catalyst. The reason for this is that it is the most active catalyst towards electrochemical oxidation and that the above-mentioned problems maybe solved by making structural changes to MS-SOFCs like addition of micron level thin diffusion barrier layers.

Zhan Z et al. [38] have worked widely on anode catalyst materials for MS-SOFCs. They have tried using only nickel as their functional anode [38] with a 2 wt% loading. During a 12-hour operation in humidified hydrogen, the combined electrode polarization resistance increased from 2.28 to 3.5 $\Omega.cm^2$. Figure 2.1 shows impedance spectra at the start and end of 12 hours.

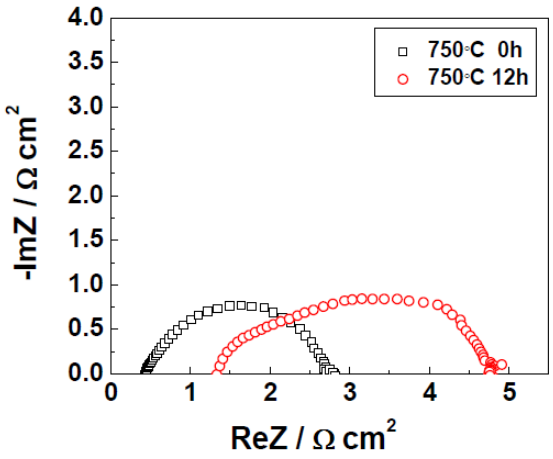

Figure 2.1: Impedance spectra of a metal supported solid oxide fuel cell with impregnated nickel as anode and Strontium Samarium Cobalt oxide (SSC) as cathode [38].

It was reported that the initial high polarization (2.28 $\Omega.cm^2$) was due to low catalyst loading and that its increase through the 12 hours period was because of coarsening of nickel particles. Based on the work of Zhan et al. [38,55,56], Table 2.1 gives a comparison between Ni, Ni-SDC, and Ni-YSZ as the anode electro-catalyst.

Table 2.1: Summary of performance of MS-SOFCs with different anode materials [38,55,56].

Anode Catalyst	MPD/Temperature ($W.cm^{-2}$)/(°C)	Combined Polarization Resistance ($\Omega.cm^2$)	Anode Polarization Resistance ($\Omega.cm^2$)	Cathode Polarization Resistance ($\Omega.cm^2$)
Ni [38]	0.38/750	2.28	-	-
Ni-SDC[55]	1.09/750	0.12	0.096	0.024
Ni-YSZ[56]	0.548/750	0.44	0.35	0.09

It can be seen that Ni-SDC shows the best performance as anode catalyst. The reason for this is the high triple phase boundary (TPB) when Ni is mixed with SDC and the mixed ionic electronic conduction (MIEC) nature of SDC. Since SDC can also conduct electrons it reduces the ohmic resistance inside the anode. Another group [57] used Ni-YSZ as the functional anode layer for MS-SOFCs. Their cell had a honeycomb microstructure for the metal support and it was reported that cell showed MPD of 0.05 $W.cm^{-2}$ at 700°C. This performance is considerably lower than that reported in the work of Zhan et al. [56]. Gadolinium Doped Ceria (GDC) is an alternate material to SDC, showing similar electrical properties [58]. Blennow et al. [59] have tried using GDC with nickel in their MS-SOFCs, which was compared with the performance when only ceria and GDC were used. The results are summarized in Table 2.2.

Table 2.2: Anode polarization resistance obtained from [59] at 650°C for different anode materials.

Anode material	Anode Polarization Resistance ($\Omega.cm^2$)
Ceria (CeO_2)	5.1
CGO20 (Gadolinium Doped Ceria)	1.2

CGO20-Ni	0.12

Comparisons of Tables 2.1 and 2.2 shows that SDC and GDC lead to very similar performance. In [59], MS-SOFCs with Ni-GDC were tested for galvanostatic durability testing and showed 5%/hour degradation. Similarly, Franco et al. [60] used Ni-YSZ for cells in mobile application. This cell was put through a galvanostatic durability testing as well, during which the cell went through thermal cycles (between room temperature and 800°C at 3°C/min) after every 100 hours of durability test. Throughout the test the cell maintained a power density of 0.15 $W.cm^{-2}$ which shows that even YSZ can be used to stablize the nickel structure. In another study [61] at Plansee-Austria, Ni-GDC was compared with Ni-YSZ as the anode functional layer. Ni-GDC showed ASR of 0.41 $\Omega.cm^2$ at 759°C [61]. They used electrochemical impedance spectroscopy (EIS) to explain the lower ASR/polarization for Ni-GDC, it was reported that Nyquist plots for Ni-GDC only had a low frequency arc whereas Ni-YSZ showed a low frequency and a medium frequency arc. The low frequency arc is mostly attributed to gas diffusion limitation and the medium frequency arc to electrode process (in this case charge transfer reactions and conduction). Lower resistance to charge transfer in the case of GDC can be attributed to the MIEC nature of ceria in reducing conditions (fuel side conditions).

It was described earlier that redox cycling and long exposure to high temperature can lead to detrimental effects on the anode material [2, 4, 5]. Normally a dedicated/standalone AFL is preferred to increase TPB, however high Ni content in a dedicated AFL can lead to cell damage because of volume change during redox cycles and nickel grain coarsening. As a solution, researchers have tried using a porous backbone/scaffold, instead of standalone anode layer, which is infiltrated with the anode electrocatalysts [28]. Bae et al. [64] used 8-24 wt% loading of nickel into an anode scaffold and reported ASR close to 1 $\Omega.cm^2$. YSZ, however, is not a good electronic conductor and hence researchers have tried different materials for the backbone [65]. In [65] $La_{0.4}Sr_{0.4}Fe_{0.03}Ni_{0.03}Ti_{0.94}O_3$ (LSFNT) was used as the backbone material in MS-SOFC. The back bone was later infiltrated with Ni-GDC precursor solution (metal nitrate solution) which was thermally broken down in to Ni-GDC. At 700°C they reported a MPD of 0.77 $W.cm^{-2}$ with Fuel Utilization (FU) of 51%. Durability testing of up to 800 hours showed a degradation of 0.151 $W.cm^{-2}$/khr in power density. Based on the above literature, it is concluded that YSZ and SDC can

stablize Ni in anode, and also decrease the anode polarization resistance. However, Ni mixed with SDC shows better performance than Ni mixed with YSZ.

As outlined earlier one of the issues with the use of nickel in MS-SOFC is the interlayer diffusion of nickel and chromium. According to Zhan et al. [66] the degradation of MS-SOFCs with infiltrated anode electro-catalyst is more affected by nickel particle coarsening than interlayer diffusion. These MS-SOFCs were run through a 1500 hour long durability test and showed degradation of only 1.3%/1000hr. To verify the effect of nickel grain coarsening and inter atomic diffusion, Scanning Electron Microscopy (SEM) and Energy Dispersive X-Ray Spectroscopy (EDX) were used. SEM of anode before and after 175 hours operation showed significant change in the microstructure, whereas EDX did not show any signs of interatomic diffusion. SEM pictures of the samples are shown in Figure 2.2.

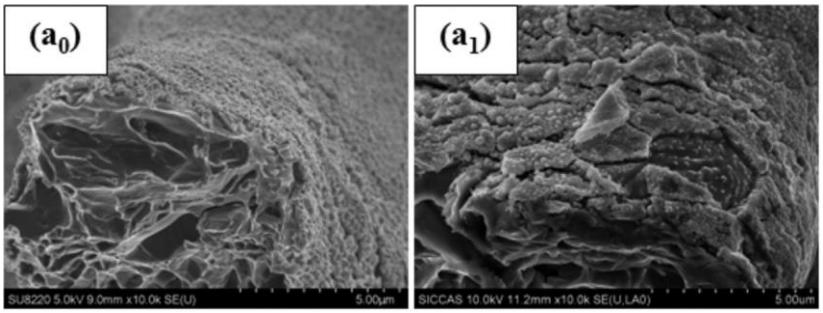

Figure 2.2: SEM image of MS-SOFC with Ni-SDC as the functional anode. (ao) before cell operation and (a1) picture after cell operation of 175 hours at 700°C [66].

However, Bae et al. [37] concluded that significant inter atomic diffusion takes place during MS-SOFCs operation. It should be pointed out though that Bae et al. used cells in which the metal support was a pre-made stainless steel plate on which an anode supported cell was sinter joined. This means that before manufacture and operation there was a segregation of stainless steel constituents in the metal support layer. There was a transition or adhesion layer between the plate and the AFL. They studied inter atomic diffusion using EDX and their results are shown in Figure 2.3.

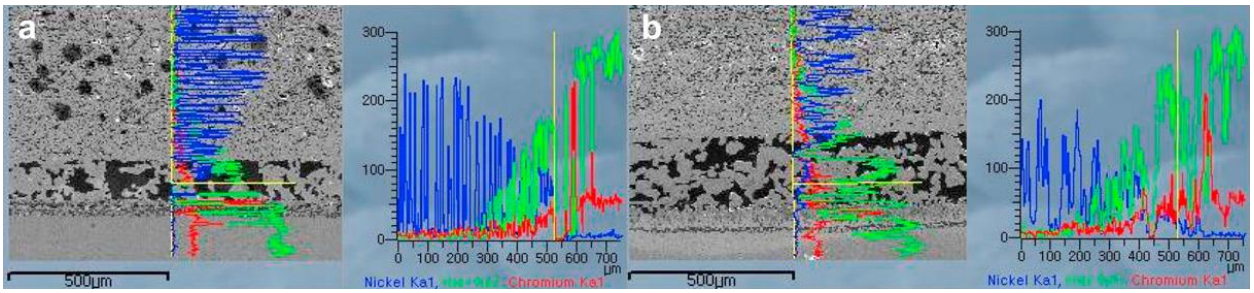

Figure 2.3: SEM image coupled with EDX spectra for MS-SOFC cells with an adhesion layer between metal support and anode (a) Image and spectra before operation (b) Image and spectra after operation [37].

Figure 2.3 shows significant diffusion of iron and chromium into the functional anode layer. Iron is initially up to the 300 µm mark inside the anode functional layer and moves to 200 µm mark during operation. The presence of iron and chromium in the anode layer prior to operation shows that iron and chromium also diffuse in the anode during manufacturing, especially during the sintering process. One solution to inhibit inter atomic diffusion is the use of a diffusion barrier layer (DBL) [53].

Nickel, although the most common choice for anode, is not the only material which has been researched. A summary of work done at Shanghai Institute of Ceramics-Chinese Academy of Science is given in Table 2.3 [67–69]

Table 2.3: Performance results for different anode materials used in MS-SOFCs at the Shanghai Institute of Ceramics Chinese Academy of Science.

Anode material	Polarization resistance	Maximum Power Density
$Sr_2Fe_{1.5}Mo_{0.5}O_{6-d}$ (SFMO)[68]	0.11 Ω.cm^2 at 800°C	0.81 W.cm^{-2} at 800°C
$La_{0.6}Sr_{0.4}Fe_{0.9}Sc_{0.1}O_{3-d}$(LSFSc) | YSZ[69]	0.21 Ω.cm^2 at 800°C	0.65 W.cm^{-2} at 800°C
$La_{0.6}Sr_{0.4}Fe_{0.9}Sc_{0.1}O_{3-d}$ | LSGM [67]	0.90 Ω.cm^2 at 800°C	0.18 W.cm^2 at 800°C

In [68] Zhan et al. also worked on the effect of anode catalyst loading and concluded that 16 wt% catalyst shows the lowest anode polarization. In Comparison to Ni-SDC (0.096 Ω.cm^2 at 750°C [55]), SFMO shows slightly higher resistance. The primary difference in cells in [69] and [67] is

the electrolyte; while the cells in [69] had YSZ, cells in [67] had LSGM as electrolyte. This might be reason for substantially lower performance of the cells in [67] as LSGM has a lower conductivity than YSZ. In [67], EIS showed that below 700°C the controlling regime at the anode was hydrogen oxidation, this was attributed to poor oxygen ion transfer from LSGM. By increasing the temperature to 800°C the ohmic resistance decreased from 7.5 $\Omega.cm^2$ to 3.11 $\Omega.cm^2$. Even more interesting is the fact that ohmic resistance reduces to 0.58 $\Omega.cm^2$ by the addition of copper. This means that high conduction/collection of electrons also reduces the resistance to hydrogen electrochemical oxidation reaction. Hence, the resistance to charge transfer reaction (hydrogen oxidation, previously labelled as controlling regime) is not because of only slow oxygen transfer between electrolyte and anode interface but may also be because of slow electron removal from anode when copper is not present. For overall electrochemical performance, cells with and without copper in LSFSc as anode were tried in humidified hydrogen as fuel; MPD for cells without copper at 800°C was 0.18 $W.cm^{-2}$ and with copper it increased to 0.54 $W.cm^{-2}$. Therefore, use of an additional electronic conducting material like copper might be useful to reduce firstly the ohmic resistance of the cell and secondly to reduce the anode polarization resistance.

Persson et al. [70] used ruthenium and nickel separately with GDC. Ruthenium showed better electrochemical performance than nickel. Cells with ruthenium had lower Area Specific Resistance (ASR) of 0.322 $\Omega.cm^2$ compared to cells with nickel (0.453 $\Omega.cm^2$). The limiting current density for cells with ruthenium was also higher than that for nickel. The polarization curves and Nyquist plots are shown in Figure 2.4.

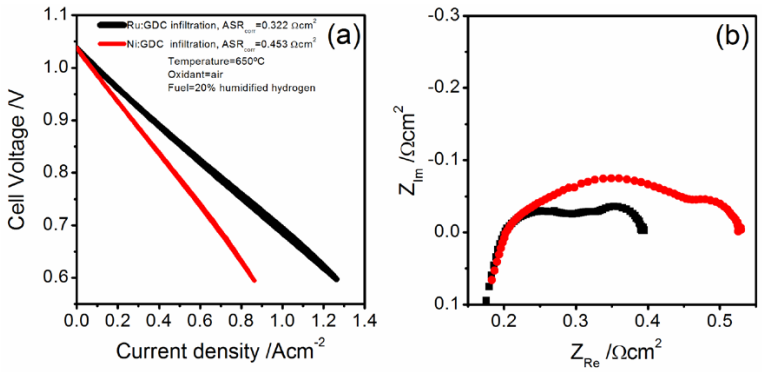

Figure 2.4: a) polarization curve for MS-SOFC with Ni-GDC (red) and Ru-GDC (black) as anode, b) impedance spectra of MS-SOFC with Ni-GDC (red) and Ru-GDC (Black) as anode [70].

2.2.3 Electrolyte

The electrolyte is the heart of a SOFC, it transports negative oxygen ions through it to complete the electrical circuit and provides oxygen ions for reaction with fuel at the anode. To have good performance there are some key requirements for the micro and macro structure of the electrolyte.

1. The electrolyte body should be dense. High density reduces the chances of fuel or oxidant gas from diffusing to the other side. This is important as crossover of these gasses will lead to reactants reacting without producing any external current. High density also ensures that there is sufficiently "connected" path available for oxygen ion transport, and thus ensures good ionic conductivity.
2. Adhesion with other layers. Electrolyte should be such that it should adhere to the anode and cathode layer. Most cells fail due to delamination of layers and cracks between layers.
3. Shrinkage of electrolyte is another important factor; during manufacturing using sintering, the shrinkage of all components should match that of electrolyte.

To satisfy the above requirements most electrolyte materials are in fact doped oxides of zirconium or cerium [38,53,57,71,72]. Oxides have fixed oxygen positions in the crystal structure which form an oxygen path in the bulk of material. By doping the oxide with a lower valent cation, oxygen vacancies along this structure are created which act as a path for oxygen ions. In most of the published literature, an OCV slightly higher than 1 V (with hydrogen as fuel) is reported for dense electrolytes.

Since there are only a few options available for electrolyte, most of the work done is on electrolyte densification opposed to the choice of material. In essence, there are two different methods for densification. First is the use of high sintering temperature and second is the use of thermal spraying deposition methods such as plasma spray deposition (PSD), magnetron sputtering or pulsed laser deposition (PLD). Table 2.4 shows results from different published articles pertaining to the type of electrolyte used, reported OCV values, and densification method.

Table 2.4: Common electrolyte materials and densification methods for MS-SOFC.

Electrolyte Material	Reported OCV	Densification method.

YSZ [38,55,56,58,66,68,73–76]	1.0-1.12 V	Sintering in reducing atmosphere (5% H_2/95% N_2) at 1300℃.
YSZ [28,77]	~1.1 V	Co-sintering in reducing atmosphere above 1300℃.
ScYSZ [59,78–80]	1.1-1.13 V	Co-sintering in reducing atmosphere.
YSZ [81]	>1.0 V	Co-sintering in reducing atmosphere at 1300℃.
YSZ [57]	1.078 V	Co-sintering at reducing atmosphere.
YSZ [82]	0.95-1.1 V	Physical vapor deposition (PVD). Improvement in OCV by increasing the number of layers of electrolyte.
YSZ [53]	0.95-1.05 V	Plasma sprayed deposition.
LSGM [39,47,83–85]	1.0-1.15 V	Atmospheric plasma spray (APS) deposition.
GDC[86]	0.95 V	Physical vapor deposition.

High sintering temperatures are required for maximum electrolyte densification, but this can lead to warping and microstructural changes in metal support and anode. To deal with this problem Franco et al. [86] have worked on the electrolyte deposition and densification aspect of MS-SOFC in collaboration with Forschungszentrum Jülich, Karlsruhe Institute of Technology (KIT), and AVL List GmbH. They have tried various state-of-the-art techniques to deposit dense thin layers of electrolyte on metal support to avoid high temperature sintering. In [86], they used a bi-layered electrolyte deposited via physical vapor deposition. The first layer (from anode side) consisted of sintered porous YSZ layer which was later coated with 1-2 µm thick layer of gas tight GDC film via PVD. In principle, YSZ is an adaption layer and acts as electron blocking layer. They obtained an OCV of 0.96 V at 823°C, which is lower than commonly reported OCV. They attributed the lower OCV to a leakage rate of 1.2×10^{-3} $hPa\cdot dm^3.(s\cdot cm^2)^{-1}$ through the electrolyte. Upon further investigation it was noticed that the OCV increased to more than 1 V when the leakage rate was decreased, but the method used to decrease the leakage was not mentioned in this article. This cell showed a maximum power density of 530 $mW.cm^{-2}$ when the current density was 0.76 $A.cm^{-2}$ at

823℃. In another work [87] they have tried using gas flow sputtering to deposit a thin dense layer of YSZ on a metal support-anode substrate followed by coating a GDC barrier layer on YSZ via magnetron sputtering. However, electrochemical performance results were not reported in this article.

Tsai et al. [39] have worked with $La_{0.8}Sr_{0.2}Ga_{0.8}Mg_{0.2}O_{3-\delta}$ (LSGM) as electrolyte. They used plasma spray deposition for coating LSGM of 30-40 µm thickness. They reported OCV of more than 1.0 V and MPD of 0.48 $W.cm^{-2}$ at 750℃ with hydrogen as fuel. In another study, Tsai et al. [84] characterized the effect of atmospheric plasma spray (APS) parameters (specifically torch power) on the electrochemical function of LSGM electrolyte. The best reported performance in this study was MPD of 0.716 $W.cm^{-2}$ at 750℃. The OCV for this cell was 0.9881 V.

Even though doped oxides of ceria have been widely used as electrolyte in all-ceramic SOFCs, their use have been limited with MS-SOFCs. This can be explained by the tendency of ceria to reduce from Ce^{+4} to Ce^{+3} in reducing atmosphere, which is the choice of atmosphere during MS-SOFC co-sintering. This change in valency can lead to changes in ceria crystal structure, which can cause cell cracking and electron short circuiting through electrolyte during operation. Still some researchers have tried using doped ceria as electrolyte in MS-SOFC by using techniques like pulsed laser deposition, plasma spray deposition and constricted sintering to successfully coat electrolyte layers. Hui et al [88] have used mono layered SDC as electrolyte and a bi-layered ScSZ-SDC as electrolyte in MS-SOFCs (performance stats shown in Figure 2.5).

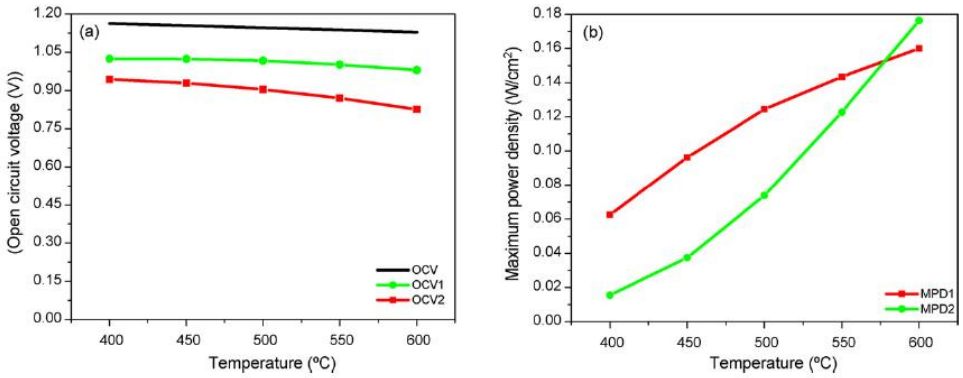

Figure 2.5: a) comparison of OCV of cells with bi-layered ScSZ-SDC as electrolyte (OCV1) and cell with just SDC as electrolyte (OCV2); b) comparison of MPD of cell with bi-layered ScSZ-SDC as electrolyte (MPD1) and cell with just SDC as electrolyte (MPD2)[88].

A cell with only SDC as electrolyte had an OCV of 0.944 V at 600°C compared 1.024 V for cell with bi-layered ScSZ-SDC as electrolyte. Cell's higher OCV is attributed to electron blocking nature of ScSZ which prevents electron short circuiting from SDC electrolyte.

2.2.4 Cathode

Cathode is responsible for reduction of oxygen to oxygen ions. Most cathode materials are doped metal oxides; used in order to provide active sites for oxygen adsorption and reduction. Up till now numerous cathode materials have been tested and ranked based on their polarization and reactivity with the electrolyte, for example LSCF [59], LSC [89], LSM [53], SBSCo [90]. Conventionally cathode is applied in slurry form which is dried, and heat treated (sintered) to attain a good adhesion with the electrolyte. Using this cathode sintering method in MS-SOFCs can lead to numerous problems which can be highlighted as:

1. Cathode materials are doped metal oxides and perovskites. At high sintering temperatures in reducing atmosphere (limitation because of metal support) these oxides can reduce and go through changes in crystal structure. This can lead to high cathode polarization, or worse, to catalyst inactivity.
2. Since YSZ is easier to process in the case of MS-SOFCs, it has been the more common choice. A lot of commercial cathode materials are reactive towards YSZ which leads to physical changes in the electrolyte layer and the cathode layer. This can reduce cell life.

The issue of cathode sintering can be solved by either decreasing the sintering temperature required by cathode material or by using cathode material which can be sintered in reducing atmosphere at high temperature. Both approaches have been tried by researchers. Bae et al. [91] . have suggested the use of barium containing cathode which can be sintered at lower temperatures (below 1000°C). They attribute the high sinterability of these perovskites to the presence of barium on 'B' site in a perovskite structure. Two different barium containing cathode materials were tried; $SmBa_{0.5}Sr_{0.5}Co_2O_{5-d}/Ce_{0.9}Gd_{0.1}O_{1.9}$ (SBSC50) and $Ba_{0.5}Sr_{0.5}Co_{0.8}Fe_{0.2}O_{3-d}$ (BSCF). Both cathode materials were in-situ sintered at 800°C during operation of cell and showed ASR of 0.02 $\Omega.cm^2$ and 0.054 $\Omega.cm^2$ for SBSC50 and BSCF respectively. They also compared sinterability of different cathode materials in [92]. Table 2.5 gives out the summary of this comparison

Table 2.5: Sinterability comparison of different cathode materials [92].

Cathode material	Adhesion at low sintering temperature (below 900°C)
LSM82	Poor
LSF82	Good
LSCF	Good
SSC40	Good
SBSC50	Excellent
BSCF	Excellent

Zhan et al. [90,93] have also worked with SBSC50 as cathode material. However, they used SBSC50 infiltrated into a SSZ [90] and a LSGM [93] scaffold as opposed to a screen printed layer in case of Bae et al. [91,92]. Their cells showed ASR of 0.413 $\Omega.cm^2$ at 550°C in case of SSZ scaffold and 0.035 $\Omega.cm^2$ at 550°C for LSGM scaffold. For cells with SBSC50 is a porous LSGM scaffold, charge transfer reaction of adsorbed oxygen was labelled as the controlling mechanism.

Blennow et al. [59,78,79,89,94] have studied the effect of in-situ sintering temperature on the performance of LSC and LSCF cathode with and without GDC. They report that addition of GDC can decrease the polarization resistance for both LSC and LSCF by increasing the ionic conductivity of the bulk material. However, GDC also requires a high sintering temperature because of its low sinterability, this implies that LSCF and LSC with GDC will need high in-situ sintering temperature (up to 900°C). Other than pure LSCF, all solid solutions, i.e, LSC, LSC/GDC, and LSCF/GDC, show small polarization values which decrease with increasing sintering temperature. At 650°C operation temperature the total polarization resistance of cathodes sintered at 800°C were ~2 $\Omega.cm^2$ for LSCF, ~0.15 $\Omega.cm^2$ for LSCF/GDC, ~0.08 $\Omega.cm^2$ for LSC, and ~0.04 $\Omega.cm^2$ for LSC/GDC.

Another approach towards reducing the cathode sintering temperature is the use of a porous scaffold on cathode side (normally made of YSZ, SSZ, LSGM etc.). In this the cathode catalyst is

infiltrated in the cathode scaffold and hence does not need a sintering process for binding to the electrolyte surface. Zhan et al. [38,55,75,76,90,93,95,56,58,66–69,73,74] have worked extensively with different cathode materials which were all infiltrated in a cathode scaffold and heat treated at 850℃ in reducing atmosphere (5% H_2/95% N_2). Table 2.6 shows a list of all the cathode catalysts they have tried.

Table 2.6: Performance comparison of infiltrated cathode catalyst (work from CAS Key Laboratory of Materials for Energy Conversion, Shanghai Institute of Ceramics, Chinese Academy of Sciences (SICCAS).

Cathode material	ASR/polarization resistance	MPD
SSC [38]	Combined polarization resistance 2.28 $\Omega.cm^2$ at 750℃.	0.38 $W.cm^{-2}$ at 750℃.
(LSFSc) [55]	Cathode ASR using symmetrical cathode cells 0.037 $\Omega.cm^2$ at 750℃ and 0.155 $\Omega.cm^2$ at 650℃.	1.09 $W.cm^{-2}$ at 750℃.
LSFSc [95]	ASR using symmetrical cathode cells 0.16 $\Omega.cm^2$ at 650℃.	0.636 $W.cm^{-2}$ at 750℃.
ESB-Ag [56]	Cathode ASR 0.09 $\Omega.cm^2$ at 750℃.	0.568 $w.cm^{-2}$ at 750℃.
ESB-Ag [73]	Combined polarization resistance is 0.10 $\Omega.cm^2$ at 750℃ with YSZ as electrolyte. Combined polarization resistance is 0.07 $\Omega.cm^2$ at 750℃ with SSZ as electrolyte.	1.3 $W.cm^{-2}$ at 750℃ with YSZ electrolyte. 1.55 $W.cm^{-2}$ at 750℃ with SSZ as electrolyte.
SFMO [75]	Cathode ASR of approximately 0.1 $\Omega.cm^2$ at 750℃.	0.316 $W.cm^{-2}$ at 750℃.
SFMO [76]	Cathode ASR of 0.09 $\Omega.cm^2$ at 750℃.	0.56 $W.cm^{-2}$ at 750℃.
SBSCo [90] with SSZ as electrolyte	For samples with catalyst calcined at 700℃ Cathode ASR 0.413 $\Omega.cm^2$ at 550℃.	1.25 $W.cm^{-2}$ at 700℃

and cathode backcone.		
SBSCo [93] with LSGM as electrolyte and cathode backbone.	For samples with catalyst calcined at 850℃ Cathode ASR 0.035 Ω.cm^2 at 500℃.	1.5 W.cm^{-2} at 600℃. This was not a MS-SOFC, the support was made of porous LSGM infiltrated with Ni as anode catalyst.

Similarly, Tucker [28,77,96] has used a porous scaffold of metal on both anode and cathode side with LSM as the cathode catalyst.

The second major problem to address is the interaction of cathode catalyst with YSZ electrolyte. Blennow et al. [78,94] have tried using a diffusion barrier layer of GDC between YSZ and Cobalt and Strontium containing cathode catalysts (LSCF, and LSM). They tried two different deposition techniques for the barrier layer, the first one was Physical Vapor Deposition (PVD), and the second was spin coating. The report that dense barrier layer deposited using PVD can effectively block the reaction between LSCF, and LSM. Similarly, Franco et al. [82] have also used a thin GDC barrier layer deposited via magnetron sputtering with LSF, LSCF, and LSM cathodes.

Another approach to reduce the interaction of cathode catalyst and YSZ is to use catalyst which do not contain Lanthanum, Cobalt or Strontium. Zhan et al. [95] have tried using different cathode catalyst, amongst which they reported that LSFSc, ESB-Ag (oxides of bismuth-erbium and silver)[56], ($La_{0.74}Bi_{0.10}Sr_{0.16}$)-$MnO_3$ (LBSM)-ESB-Ag, and GDC-LBSM-ESB[97] do not react with YSZ. A detailed comparison cathode catalyst used in their work is given in Table 2.6

Bae et al. [40] has studied the effect of Cobalt content in $La_{0.8}Sr_{0.2}Co_{1-x}Mn_xO_{3-\delta}$ (LSCM) on the performance of MS-SOFCs. It was reported that 40 mol% Cobalt gives the optimum performance, and that higher amounts of Cobalt may react with YSZ electrolyte. In further study they reported that Cobalt higher than 40 mol% in LSCM can change the CTE of LSCM which can lead to cracking [98]. As a solution to cobalt reaction with YSZ, Bae et al. [99] have tried the use of

chromium containing cathodes. Chromium content was varied in $La_{0.8}Sr_{0.2}Cr_{1-x}Mn_xO_{3-\delta}$ (LSCrM) between 0 and 80 mol%. In addition, they also used a binary cathode of LSCrM and ruthenium (5mol%). They reported that by replacing Cobalt with Chromium the cathode can be sintered in inert atmosphere. Table 2.7 shows ASR values of samples sintered in nitrogen and in air. It can be seen that ASR of LSM (without chromium) is higher than that of sample with 50 mol% chromium. It was also reported that addition of ruthenium stabilized the performance.

Table 2.7: Approximated values of ASR for different LSCrM cathodes calculated using ASR plots at 900°C [99].

Cathode	ASR ($\Omega.cm^2$) (sintered in N_2)	ASR ($\Omega.cm^2$) (Sintered in air)
LSM	~5.0	~0.1
$La_{0.8}Sr_{0.2}Cr_{0.2}Mn_{0.8}O_{3-d}$	~4.5	~45.0
$La_{0.8}Sr_{0.2}Cr_{0.5}Mn_{0.5}O_{3-d}$	~0.2	~0.2
$La_{0.8}Sr_{0.2}Cr_{0.8}Mn_{0.2}O_{3-d}$	~3.16	~23.0
$La_{0.8}Sr_{0.2}Cr_{0.45}Mn_{0.5}O_{3-d}/Ru_{0.05}$	~0.2	~0.15

2.2.5 Structures of co-sintered MS-SOFC

When using tape casting and co-sintering for MS-SOFC fabrication, a half-cell structure is co-sintered prior to the addition of electrode catalysts. This is primarily done to optimize cell performance and increase cell life. High temperature exposure to electrode catalyst can lead to grain coarsening of the catalyst particles which reduces cell performance. Another reason is the instability of conventional cathode materials in reducing atmospheres at high temperature. This means, that apart from maintaining cell mechanical integrity during co-sintering it is necessary that the cell structure be such that it can accommodate electrode catalysts. This co-sintered half-cell structure functions as a base structure on which electrode catalysts are added. Tucker et al. [28,77,96,100–103] have extensively worked with MS-SOFC fabrication using co-sintering. They have tried various half-cell structures for co-sintering, however, their symmetrical MS-SOFC structure (Figure 2.6) offers numerous advantages [28,100]. By having a metal on both sides, the

shrinkage profile mismatch between ceramic and metal does not cause cell warping during co-sintering. Similarly, it affords good mechanical strength on both sides of the cell, good current collection on both sides, and the electrode catalysts can be subsequently infiltrated into the porous anode and cathode structures. It has been reported that the cell structure and performance remain stable during 200 thermal cycles (between room temperature and 800°C) and during 20 redox cycles [28]. In a recent publication they report that this cell structure shows MPD of 1.34 $W.cm^{-2}$ at 700°C.

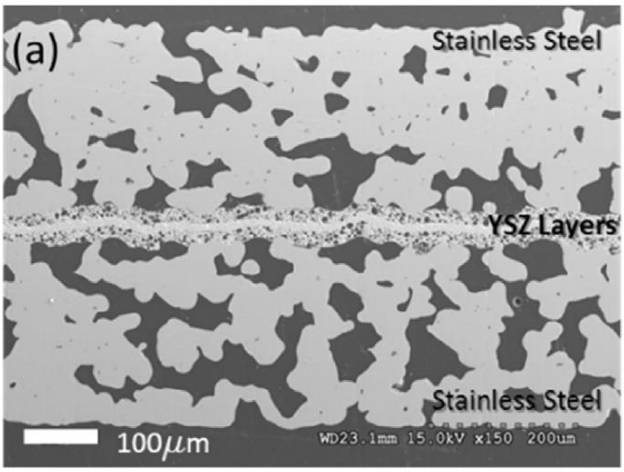

Figure 2.6: SEM image of cross-section of a symmetrical MS-SOFC [28].

Zhan et al. [38,55,73,74] have worked on a structure made of porous Stainless Steel (SS) 430L followed by dense YSZ electrolyte and porous YSZ cathode backbone layer. After co-sintering the base structure, anode and cathode catalysts are infiltrated into the porous 430L layer and porous YSZ backbone, respectively. This structure helps cathode in-situ sintering during operation as the backbone (YSZ) is co-sintered with the cell and is infiltrated with cathode catalyst. The backbone layer, hence, has enough strength to house the cathode catalyst, and maintain its original geometry. Figure 2.7 shows an SEM image of their cell structure. Zhan et al. [38,55,75,76,90,93,95,56,58,66–69,73,74] have used this structure with many different anode and cathode catalysts. Some electrochemical performance results were given in section 2.2.4.

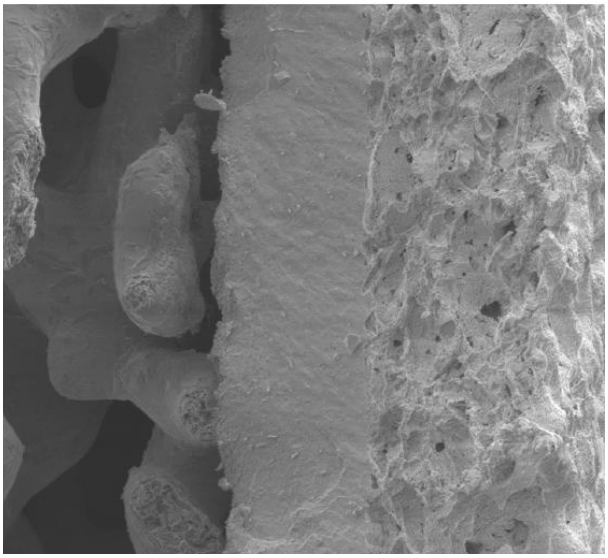

Figure 2.7: SEM image of cross-section of MS-SOFC, left to right-Porous metal support| Electrolyte| YSZ cathode backbone [38].

Blennow et al. [59,78,79,89,94] have reported a slightly different half-cell structure for co-sintering. In their work they co-sinter stacked metal support, a cermet layer (metal/YSZ mixture), and an electrolyte layer (see Figure 2.8). To add anode catalyst, they use solution infiltration whereas cathode is screen printed. In some of their work [78,94] they use a barrier layer of GDC between cathode and electrolyte. This barrier layer is deposited using PVD and spin coating [78]. They have reported MPD of 1.14 $W.cm^{-2}$ at 650°C for their cells with barrier layer [78].

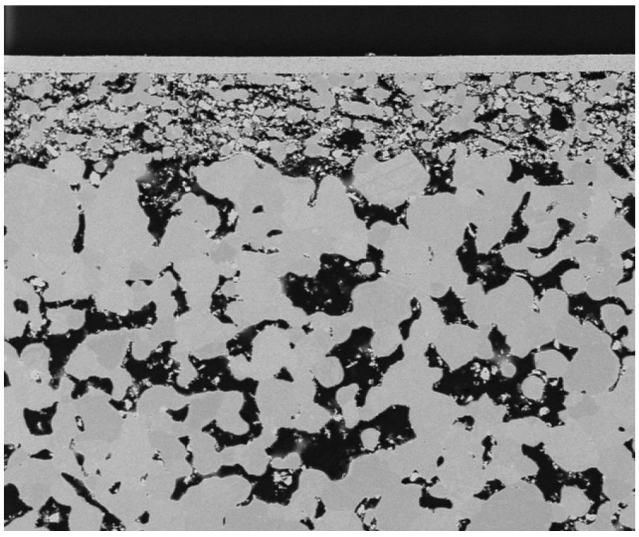

Figure 2.8: SEM of cross-section of co-sintered MS-SOFC [59].

2.2 Use of sintering aid for doped ceria electrolytes

Ceria, whether doped with samarium or gadolinium, needs a temperature of approximately 1400°C for considerable densification to prevent fuel and/or oxidant short circuiting [104]. Further, CeO_2 also shows surface and bulk reduction to Ce_2O_3 at high temperatures and reducing atmosphere [105]. This implies that co-sintering of SDC with metal support close to 1400°C in reducing atmosphere may lead to structural changes in the doped ceria electrolyte layer and may cause cracking. To limit the extent of ceria reduction the sintering temperature for SDC can be lowered, so that doped ceria does not face extremely high sintering temperatures and reducing atmosphere. Researchers have used the following methods to lower the sintering temperature:

1. Reduce the powder size through mechanical milling techniques, and/or using specific synthesis routes like Glycine Nitrate Combustion (GNC) process etc. Smaller particle size increases the driving force of sintering (reduction of surface area) [31].
2. Use of metal oxides as sintering additives to activate liquid phase sintering and increase the surface atom mobility. Researchers have used Mn_2O_3 [106], Co_3O_4 [106], Ga_2O_3 [107] Fe_2O_3[108][109], LiO[110], and CuO [33,34,111].

Sintering aid's primary purpose is to lower the sintering temperature. Sintering is a thermally activated process, which works by reducing the excess surface energy of particles by atomic diffusion through the grains and along the grain boundaries. Through sintering theory, it is known that, amongst others, particle size and particle arrangement of initial powder compact also have an effect on the sintering dynamics. For instance, it has been reported that small size pores between ultra fine particles can lead to high capillary pressure which causes low final sintered density and cracks[31]. Hence the packing and re-packing of particles during sintering is critical to achieve maximum density. Keeping this in mind, a sintering aid can affect the diffusivity of the grains of primary material and induce a closed packing. In published literature, researchers have used arguments based on this to explain how particular sintering additives work. In literature, [34], it has been reported that CuO as sintering aid with GDC can form a ternary phase Gd_2O_3–CeO_2–CuO which can melt and promote liquid phase sintering. Presence of liquid at the grain boundaries can increase the mobility of the grains [32], however it is also reported that primary solid phase should be soluble in the liquid phase for effective liquid phase sintering [112].

Among the few transition metals investigated as sintering additives for doped ceria, iron, lithium, cobalt, and copper have been the preferred choices. Amongst these, copper is of special interest due to the following reasons:

1. Copper has been identified as one the most effective sintering aids, where it can reduce the sintering temperature of GDC from 1400℃ to 1000℃ [32].
2. In [31] it was reported that copper forms an additional phase on the surface of sintered copper doped SDC. Copper oxide diffusion to the electrolyte surface on the anode side might actually be beneficial to lower the anode polarization resistance. Under anode conditions (humidified hydrogen) the copper oxide phase on SDC electrolyte can be reduced back to copper which has a high electronic conductivity. It has been reported that increase of electronic conductivity near TPB can lead to decrease in anode polarization because of fast removal of electrons [67].

Even though a lot of literature has been published on copper as sintering aid, most of the work was based on copper addition to GDC [32–34,111]. Similarly, the amount of copper used for doping was mostly 1 mol% and only a few articles showed the effect of a higher copper content on only the microstructural properties of copper co-doped ceria [31].

The addition of sintering aids have an effect on the conductivity of the electrolyte [113]. The effect a sintering aid might have on the conductivity is still unclear; Zhang et al. [31] showed that 1 mol% addition of CuO lowers the conductivity of SDC whereas Macedo et al. [34] showed that 1 mol% CuO increases the conductivity of SDC. Similarly, varied conclusions have been reported about many other sintering aids and their effect on the conductivity of SDC/GDC [31,33,109,110,114–117]. Ceria and doped oxides of ceria are a complex conduction system, as they exhibit both ionic and electronic conductivities which is labelled as their Mixed Ionic Electronic Conduction (MIEC) behavior [59]. Ceria exhibits this character because of cerium ion's tendency to reduce to a +3 valency from +4 in reducing conditions and high temperatures. Hence the evaluation of the effect of sintering aid on conductivity of doped ceria can be difficult as the sintering aid may affect both ionic and electronic conductivities. In most of the literature, the amount of sintering aid used is limited (normally close to 1.0 mol%) [31,106,113], which makes it difficult to draw concrete conclusions about the effect of a sintering aid on conductivity of SDC.

Chapter 3 Theoretical Background on Sintering

The main work in the present research is related to sintering of ceramics and co-sintering of metal and ceramics. To understand the behavior of different materials during sintering it is important to understand the fundamentals of sintering process. This section gives out the details of working principles of sintering.

3.1 Working principles of sintering

Sintering is an important step in material synthesis/processing. It consists of producing dense solid bodies from powder compacts by the application of thermal energy. The earliest application of sintering can be found in pottery, and dates back as far as the prehistoric era. Now, the major purpose of sintering is seen in powder metallurgy, where sintering is used to produce solid bodies with controlled microstructure, grain size distribution, distribution of pores and formation and distribution of secondary phases.

In principle, there are two main categories of sintering: 1) solid state sintering and 2) liquid state sintering. In solid state sintering the solid powder is sintered or formed in to a solid body at the sintering temperature, whereas in liquid state sintering the solid powder is sintered in the presence of liquid at the sintering temperature. However, other types of sintering do exist, but the primary phases remain solid and liquid. Figure 3.1 shows a general equilibrium binary phase diagram for a mixture of ‘A’ and ‘B’.

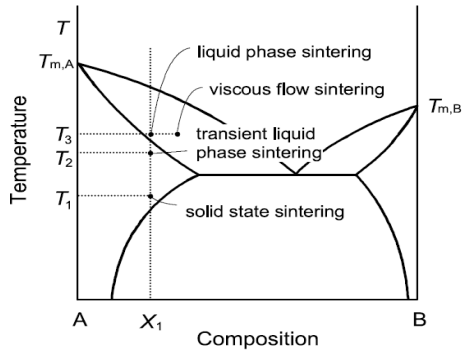

Figure 3.1: Various types of sintering on a phase diagram [118].

Four types of sintering are shown in Figure 3.1; those types are 1) solid state sintering, 2) transient liquid phase sintering, 3) liquid phase sintering, and 4) viscous flow sintering. At the composition X_1 different sintering mechanisms might occur at different temperatures. At temperature T_1, anywhere along the composition the mixture is well below the eutectic point and solidus lines for A and B, which means that upon heating to sintering temperature (T_1), there is no chance of liquid formation. Hence, at this composition the compound will remain solid throughout the sintering process and will undergo solid state sintering. At temperature T_2 the temperature is above the eutectic point and below the solidus. If the distributed phase, that of 'B', shows diffusivity into 'A', there will be a transient liquid formed of 'B' phase. After 'A' phase reach equilibrium composition between 'A' and 'B' the remaining pure 'B' phase segregates on the surface and solidifies. This type of sintering is called transient liquid phase sintering. At temperature T_3 the temperature is between solidus and liquidus, however the composition mark is closer to solidus compared to liquidus. This means that there will be more solid phase present compared to liquid phase during sintering, this type of sintering is termed liquid phase sintering. Another approach is to add a low melting temperature third phase in the mixture of 'A' and 'B'. By moving the composition mark towards liquidus, the amount of liquid phase present during sintering can be increased. If the amount of liquid is such that it can flow in the solid matrix, the sintering is termed viscous flow sintering.

The driving force for sintering is the change in the total interfacial energy of the sample. Interfacial energy is the energy which is present in excess at the surface compared to the bulk and is expressed as the product of surface energy, γ ($J.m^{-2}$), and surface area, A (m^2). The total change in surface energy, hence, can be described mathematically as [118]:

$$\Delta(\gamma A) = \Delta\gamma A + \gamma\Delta A \qquad (3.1)$$

From Eq. 3.1 it can be seen that the change in total interfacial energy or sintering depends on two different paths, where the first term on the right-hand side represents densification and second term represent grain coarsening. The first term on the right-hand side of Eq. 3.1 is termed as the densification and the second term represents grain coarsening. Densification refers to the change in energy associated with replacement of solid/vapor interface by solid/solid interfaces, whereas grain coarsening is the growth of grains. A schematic of sintering is shown in Figure 3.2.

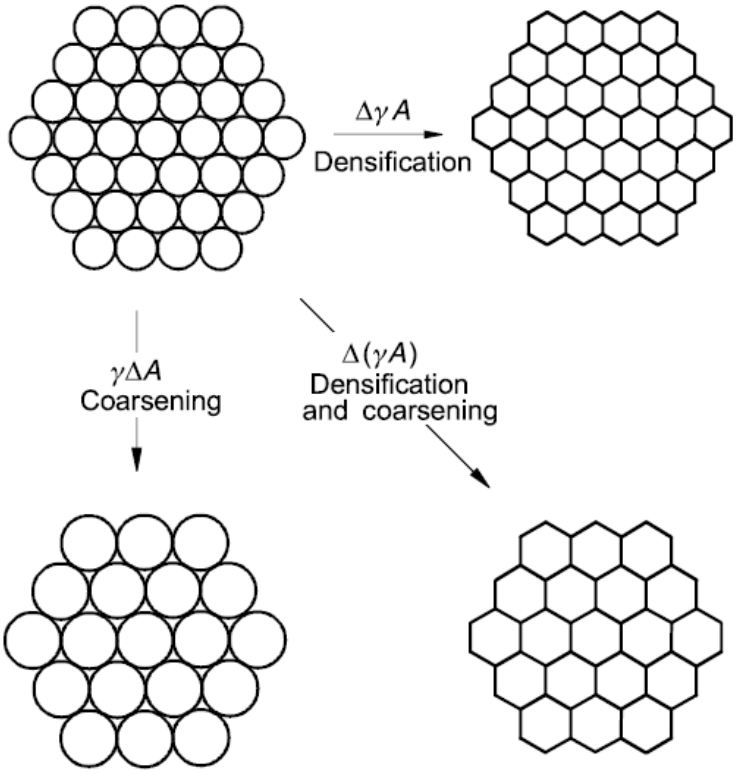

Figure 3.2: Illustration of densification and grain growth, the two paths for sintering [118].

Like any other processes, sintering is dependent on a few material and system variables. The chemical properties of the materials, including the composition, and the physical properties, including powder size distribution, greatly affects the sintering process. Similarly, temperature, and pressure have an effect on the process too.

Sintering takes place by the movement of atoms in the crystal lattice structure. In scientific terms this can be labeled as atomic diffusion or *random walk*, following the same principles underlying Ficks laws for diffusion.

$$J = -D\frac{dC}{dx} \qquad (3.2)$$

Where 'J' is the flux of atoms ($mol.m^{-2}.s^{-1}$), 'D' is the diffusivity ($m^2.s^{-1}$), 'C' is the concentration of species ($mol.m^{-3}$), and 'x' is the direction of movement (m). In the case of atomic diffusion, however, the mechanism of diffusion or movement of atoms is actually accompanied by jumping through lattice sites. While moving between two different positions an atom takes a higher energy

level intermediate site and then moves on. Hence, the energy required in taking that jump is dependant on the energy barrier of the intermediate position. By the use of Einstein formula, we can calculate the diffusion constant by:

$$D = \frac{<x^2>}{6t} \qquad (3.3)$$

where $< x^2 >$ is the mean square displacement of an atom. Since the movement of an atom is random, the mean displacement can be replaced by the product of number of jumps 'n' and the square of mean displacement an atom moves in one jump 's'. In that case Eq. 3.3 becomes.

$$D = \frac{ns^2}{6t} \qquad (3.4)$$

Similarly, the diffusion coefficient has been shown to take other forms as well. It is shown in [119] that the diffusion coefficient can also be expressed mathematically as:

$$D = D_o \exp\left(\frac{\Delta h}{KT}\right) \quad (3.5)$$

Where, Δh is the enthalpy of inter atomic diffusion, 'K' is the Boltzmann constant ($1.38064852 \times 10^{-23}$ $m^2.kg.s^{-2}.K^{-1}$), 'T' is the temperature (K) and D_o is the reference diffusivity ($m^2.sec$). The reference diffusivity can be expressed as:

$$D_o = \frac{\upsilon\lambda^2}{6} \exp\left(\frac{\Delta s}{k}\right) \quad (3.6)$$

where υ is the vibrational frequency of an atom in all six orthogonal directions, λ is the distance between two adjacent planes and Δs is the change in entropy for inter atomic diffusion. In the derivation of the above equation it is assumed that an atom jumps from one plane to the adjacent plane which is a distance λ apart.

However, sintering is a special case of diffusion. Sintering is the inter-atomic diffusion which can have many driving force gradients rather than just concentration gradients. In the past, a lot of work [119–121] has been performed to derive diffusion equations for sintering by taking chemical potential as the gradient, since changes in chemical potential can be attributed as the set containing all possible gradients driving diffusion.

As shown in Figure 3.2, sintering is the densification and grain growth of a powder mass. The major driving force for the densification process is the surface curvature or more accurately the chemical potential gradient because of surface curvature.

Imagine a surface containing convex and concave parts, as shown in Figure 3.3. Due to the presence of compressive stress beneath the convex surface, atoms are pushed out of from under that surface. Similarly, more vacancies are present under a concave surface. Hence, there is a vacancy concentration gradient between these points and if appropriate energy is supplied the vacancies start to move from concave to convex surface making it flatter or reducing the surface area.

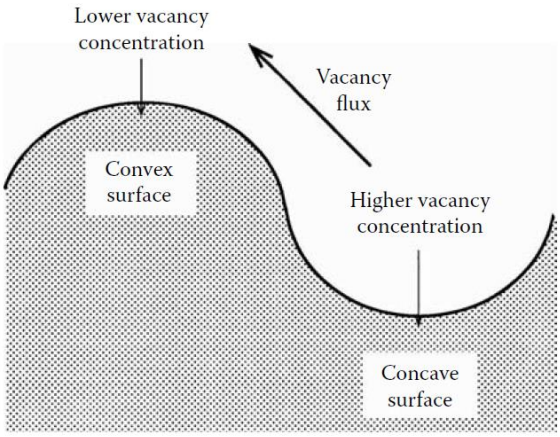

Figure 3.3: Surface curvature showing vacancy movement in solids [119].

The chemical potential can be related to three possible driving forces; external pressure, surface curvature and concentration difference by:

$$\mu_v = \mu_{ov} + (p + \gamma_{sv}K)\Omega + kTlnC_v \qquad (3.8)$$

Eq. 3.8 is for vacancies and, in a similar way, the equation for atoms can be written down as:

$$\mu_a = \mu_{oa} + (p + \gamma_{sv}K)\Omega + kTlnC_a \qquad (3.9)$$

In the above equation μ is the chemical potential and the subscript denotes whether it is for atom 'a' or vacancy 'v', p is the external applied pressure, γ_{sv} is the surface energy of the material, Ω is the molar volume. 'K', the curvature of surface, in Eqs 3.8 and 3.9 is expressed as:

$$K = \frac{1}{R1} + \frac{1}{R2} \qquad (3.10)$$

where R_1 and R_2 are the principal radii of a curved surfaces. The atomic flux, expressed as proportional to gradient in chemical potential, can now be used instead of only concentration gradient. However, a key question in sintering relates to the time required to achieve the desired microstructure. In principle, sintering can occur through six paths, each contributing to either densification or grain coarsening. Grain coarsening is the expansion in size of the grains whereas densification is the replacement of solid/vapor interfaces by grain boundaries. Those six paths are 1) surface diffusion, 2) lattice diffusion (from the surface), 3) evaporation vapor transport, 4) grain boundary diffusion, 5) lattice diffusion (from the grain boundary) and 6) plastic flow. Those six paths are shown in Figure 3.4.

Lattice diffusion (atoms from surface), surface diffusion and vapor transport are the mechanisms that help in grain coarsening while lattice diffusion (atoms from grain boundaries) and grain boundary diffusion are the mechanisms that help in densification of the powder sample. The sixth step, plastic flow diffusion, can help in both densification and grain coarsening.

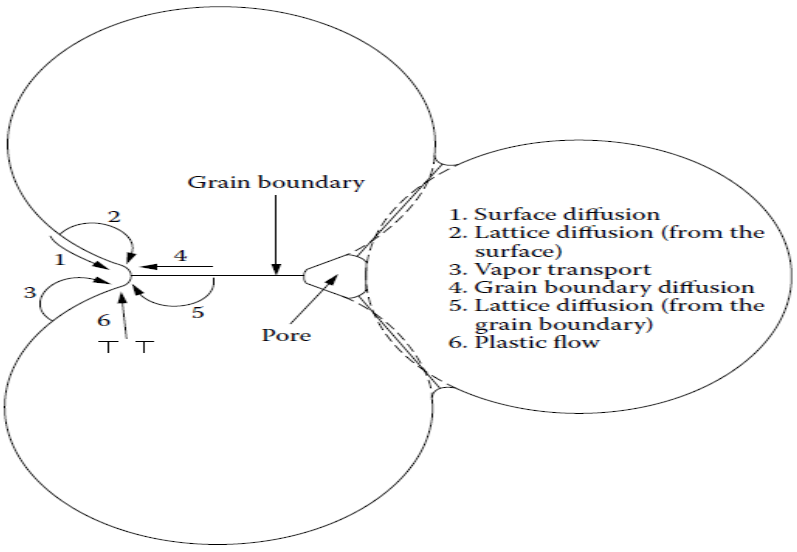

Figure 3.4: Solid state sintering mechanisms [119].

In our case the most important mechanisms are those that contribute to densification.

3.2 Enhanced sintering through sintering aid

There are four different ways in which the sintering of a particular compound can be enhanced [122]:

1. Process conditions: Reduction in particle size of initial powder, use of higher sintering temperature, and longer sintering times.
2. Changing defect features of the compound to increase atomic diffusivity.
3. Application of external force.
4. Use of sintering aids.

All of the above stated factors govern the microstructure of the sintered product. Although such a detailed analysis of sintering is not within the scope of this project, some aspects will be explained as they are important when determining sintering parameters. Herring [123] showed that, according to his scaling law, the time required for sintering increases with increasing particle size. Smaller particle size means more surface to volume ratio and hence more curvature. This leads to larger difference in chemical potential as discussed earlier. It has been reported that higher sintering temperature and longer sintering time lead to better mechanical properties, due to high densification, for sintered metal powder compacts [120]. The composition of the material affects the atomic diffusion coefficient, which in turn impacts the transport of atoms through the crystal lattice. A higher diffusion coefficient means that atoms will travel faster under the same driving force and hence will require lesser time. Increasing defect features in material by alloying, radiation treatment, etc. can lead to higher diffusion coefficients leading to higher sintering activity [122].

Sintering aid (a.k.a sintering additive) works by inducing either liquid phase sintering or activated solid state sintering in the base material being sintered. The secondary phase, belonging to sintering aid, provides a short-circuit low energy diffusion path to the atoms of the base material. Diffusion rates within a solid are scaled along the melting temperature, hence a compound with higher melting temperature will need higher sintering temperature. Sintering aids have lower melting temperature than the base material and hence higher diffusion rates which lead to enhanced sintering.

It is important, however, to carefully select the sintering additive because the choice and amount of sintering aid govern the dynamic of shrinkage and have an effect on the physical properties of the sintered product. The following criteria should be considered in the selection of sintering aid:

1. Solubility of base material in sintering phase: For effective use of the low energy diffusion path provided by the sintering aid phase, the base material should be soluble in the sintering aid phase. In contrast, the sintering aid phase should not be soluble in the base material phase, as it leads to swelling. It has been reported that for aluminium oxide-iron system, the solubility of aluminium in iron is higher and leads to swelling of grains upon heating [122].
2. Segregation of sintering aid phase on grain boundaries: To use the low energy diffusion path provided by the sintering aid phase, base material atoms have to dissolve in the sintering aid phase. Since base material's atoms transfer across the grain boundary into the sintering aid phase, the presence of sintering aid phase along grain boundaries is important. The higher the amount of grain boundary covered the higher the dissolution of base material's atoms.
3. Diffusivity of sintering aid phase: The sintering aid phase should have lower activation energy of atomic diffusion compared to the base material. Since, generally, the diffusion rates are inversely related to the melting temperature, the sintering aid should have a lower melting temperature than base material.

It was stated above that addition of sintering aid can induce both liquid phase sintering and activated solid state sintering. The difference between the two is that in liquid phase sintering, the sintering aid phase melts into a liquid phase whereas in activated solid state sintering the sintering aid remains in solid phase. Liquid phase sintering is more effective than activated solid state sintering. Firstly, the liquid phase automatically segregates on the grain boundaries, because of higher wetting characteristics than a solid. Secondly, liquid phase also exerts capillary pressure on adjoining grains which leads to a closer re-packing of the base material's grains. Thirdly, the presence of liquid phase increases the grain boundary thickness which further lowers the resistance to atomic diffusion. Figure 3.5 shows the presence of liquid phase along grain boundaries.

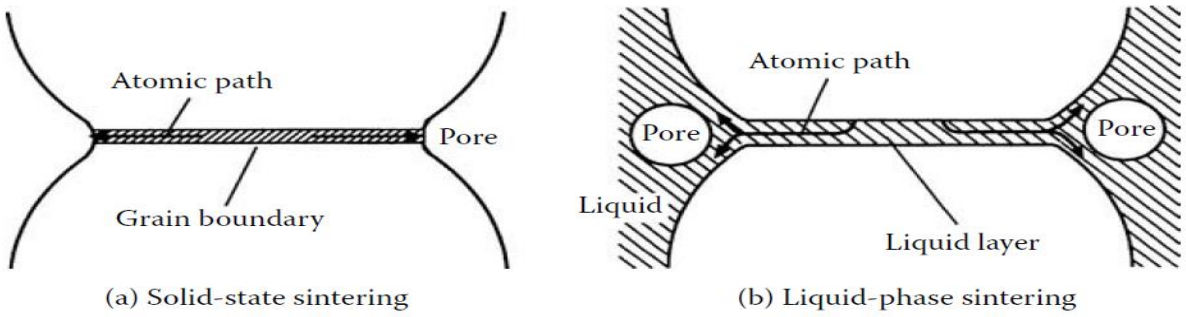

Figure 3.5: Grain boundary diffusion in a) solid state sintering and in b) liquid-phase sintering.

Chapter 4 Experimental methods

This chapter gives out the details of the experimental approach and experimental procedures used in conducting this research. As such, this chapter is divided into three sections:

1. Use of Sintering aid: In this section, details are given for making SDC with and without sintering aid (copper) and for further processing of the manufactured powder for different analytical experiments for microstructure, shrinkage and electrochemical characterization.
2. Fabrication of MS-SOFC via tape casting and co-sintering: In this section, details are given for the fabrication of MS-SOFC with YSZ and SDC as electrolyte using tape casting and co-sintering. Sub sections are given for processing of individual components (metal, electrolyte, etc.) followed by the procedure used to put all the components together for co-sintering. Since this part deals more with manufacturing of cells, different analytical experiments will also be discussed to assess the appropriate manufacturing method and conditions.
3. Apparatus and techniques used: This section gives out details about the apparatus used for analysis including XRD, SEM, dilatometry, and electrochemical testing station.

4.1 Use of sintering aid:

Copper was used as the sintering aid for SDC in this work. Since copper addition can affect physical properties, including crystal structure, shrinkage behavior, and conductivity, of SDC, experiments were chosen in a way to satisfy the objectives listed below:

1. Determine whether copper takes up space inside the fluorite crystal structure of ceria and/or segregates on the boundaries. If it dissolves in crystal structure, then is there a solubility limit after which further addition of copper will lead to a secondary phase precipitation on the grain boundaries of fluorite crystal structure of ceria?
2. Does copper, as sintering aid, help in enhancing the sintering of SDC, that is, does it lower the sintering temperature and time? Does the amount of copper used has any effect on the enhancement of SDC sintering?

3. How does copper addition affect the conductivity of SDC? and does it have an effect on a specific conduction mechanism of solid electrolytes (e.g. grain boundary conduction, grain interior conduction)?

To get a clearer picture of how copper interacts with the SDC crystal structure, a wide range of copper content (0, 0.1, 0,.5, 1.0, 3.0, 5.0 mol%) was considered. The analysis was divided into two categories; material property analysis, and conductivity analysis.

In material property analysis the structure of the samples (micro and macro) and the shrinkage dynamics of the samples were studied. For this purpose, following techniques were used:

1. X-Ray diffraction: To study the effect of copper addition on the crystal structure of SDC. This can help identify the number and types of phases formed, crystal structure parameters (lattice constant) and bulk density.
2. Scanning Electron Microscopy (SEM) coupled with Energy Dispersive X-Ray (EDX): This was used to study the macro structure of sintered samples. This can help in observing the apparent density of sintered samples, identification of different phases, and can also give an idea of the composition of phases involved.
3. Dilatometry: Dilatometry was used to study the shrinkage dynamics of samples for a given sintering profile. Dilatometry can be used to record the maximum shrinkage of samples at a given sintering temperature, shrinkage set-off temperature, time required for maximum shrinkage, and calculation of Coefficient of Thermal Expansion (CTE).

For conductivity analysis, Electrochemical Impedance Spectroscopy (EIS) was used. Through EIS total conductivity of the samples can be evaluated along with conductivity through different mechanisms (grain boundary and grain interior).

4.1.1 Fabrication of the electrolyte

The electrolyte material (SDC), with and without copper, was synthesized in lab using Glycine Nitrate Combustion (GNC) process. This is an auto-thermal combustion method where glycine is used as a complexing agent and as a fuel. Glycine (NH_2-CH_2-COOH) has zwitterionic nature where one end of the molecule has a carboxylic acid group and the other end has an amine group. This character of glycine helps in dissolution of metal salts in aqueous solution and also prevents

metal salt precipitation when the aqueous solution is heated/dried. Metal nitrates hydrates are mixed with glycine in De-Ionized (DI) water and heated on a heating plate. Over time, excess water evaporates leaving a high viscous gel. This gel is then combusted on a hot plate leaving ash of metal oxide behind.

The balanced reaction for the GNC process in the case of SDC is given below.

$$0.2\,Sm(NO_3)_3 + 0.8\,Ce(NO_3)_3 + \frac{5}{3}NH_2CH_2COOH + \frac{1}{5}O_2 \rightarrow Sm_{0.2}Ce_{0.8}O_{1.9} + \frac{7}{3}N_2 + \frac{10}{3}CO_2 + \frac{25}{6}H_2O \quad (4.1)$$

The amount of copper was set with respect to the cerium content and hence appropriate changes were made to equation (4.1). For example, if the copper content is set to 1 mol% then the assumed stoichiometric equation is:

$$0.01\,Cu(NO_3)_2 + 0.2\,Sm(NO_3)_3 + 0.79\,Ce(NO_3)_3 + \frac{5}{3}NH_2CH_2COOH \rightarrow Sm_{0.2}Ce_{0.79}Cu_{0.01}O_{1.9} + \frac{7}{3}N_2 + \frac{10}{3}CO_2 + \frac{25}{6}H_2O \quad (4.2)$$

It should be noted that such small amount of copper does not lead to significant changes in the required amount of glycine. Commercial metal nitrate hexahydrates (Alfa Aesar-VWR, Canada) of all cations were used. Stoichiometric amounts of metal nitrate hexahydrates were dissolved in 250 mL of DI-water followed by the addition of glycine (Alfa Aesar-VWR, Canada). The prepared solution was heated and stirred overnight at 90°C, using a heating plate (VWR, USA), until the solution turned into a viscous gel. This gel was then transferred to a ceramic crucible which was covered with a glass tube. Since the combustion reaction is vigorous and produces high amounts of gasses, the glass tube was covered with a perforated mesh to allow for the passage of gasses and retention of most of the powder formed. The crucible and glass tube assembly was placed on a hot plate (Salton Canada, Canada) using a lab stand and the gel was allowed to combust. Figure 4.1 shows a picture of the apparatus used for combustion process.

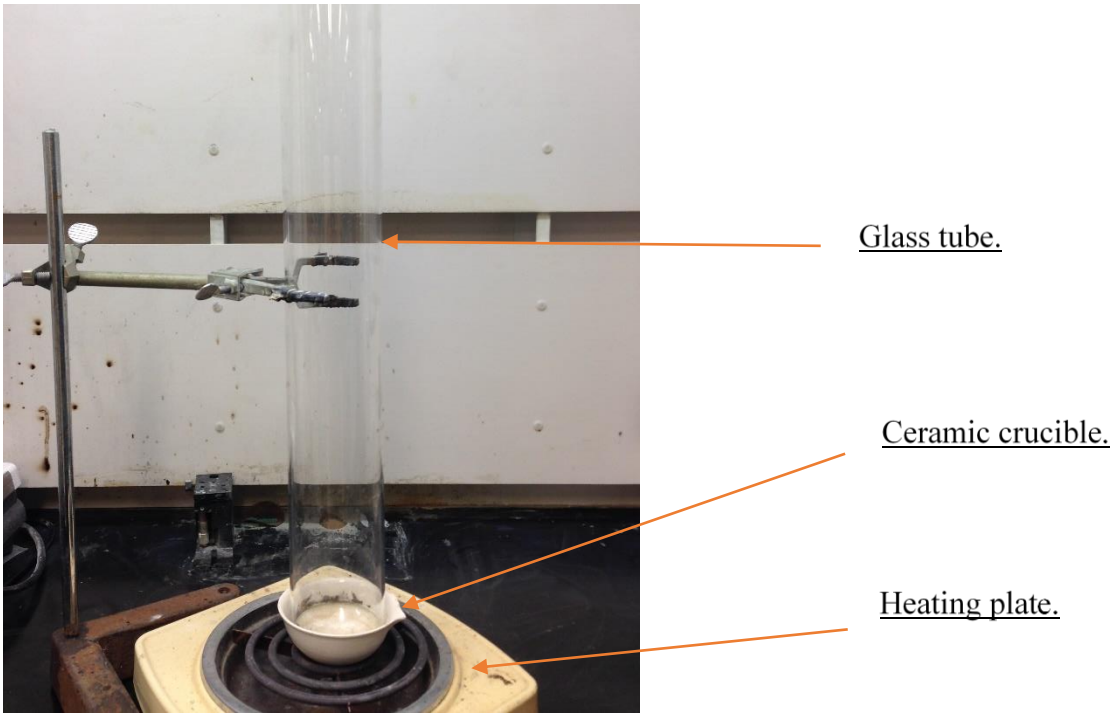

Figure 4.1: Picture of apparatus used for GNC process.

Once the reaction is complete, the powder was collected in a ceramic crucible and calcined. Calcination was done to remove any residual moisture, volatile and residual carbon materials in the powder. For calcination, a muffle furnace (Barnstead Thermolyne, USA) was used. The calcination temperature for all powders was kept at 700°C with a dwell time of 2 hours.

Once the powders were calcined, they were processed in different ways for analytical experiments. Figure 4.2 shows the sequence of experiments done to characterize the samples.

4.1.2 Sample preparation for physical properties characterization

For XRD, calcined powder was used as is. For SEM, calcined powder was pressed into circular disk of 20 mm diameter, using a hydraulic press, at a pressure of 250 MPa for 2 minutes. Pressed samples were then sintered in a high temperature furnace. Conventionally, sintering temperature of 1300-1400°C is used for SDC. In this study, two different sintering temperatures were used based on dilatometry results. A more conventional sintering temperature of 1350°C was used for plain SDC and a lower sintering temperature, 1100°C, was used for samples with copper. This was

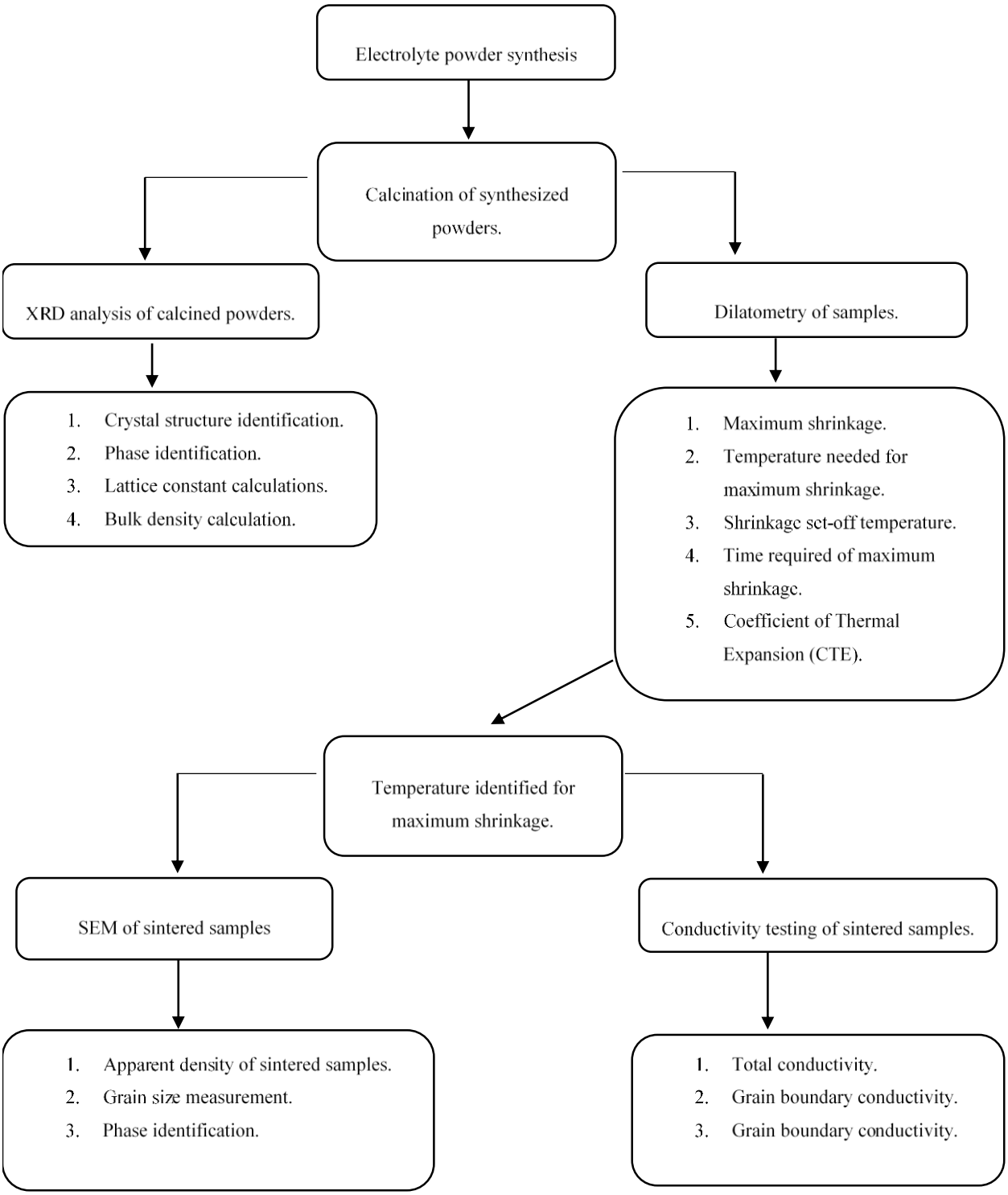

Figure 4.2: Sequence of experiments conducted to study the effect of copper as sintering aid with SDC.

done so that a fair comparison can be established between the microstructures of samples with sintering aid and the sample without sintering aid sintered at a conventional sintering temperature. For dilatometry, calcined powder was pressed into samples with rectangular cross-section (6 mm x 8 mm) at a pressure of 250 MPa for 2 minutes.

For conductivity analysis, calcined powder was pressed into 20 mm diameter circular disks at 250 MPa for 2 minutes. These disks were then sintered in a high temperature furnace. Similar to samples prepared for SEM, samples for conductivity analysis were sintered at different temperatures. SDC sample (without copper) was sintered at 1350℃ for 5 hours, and copper co-doped SDC was sintered at 1100℃ for 5 hours. Once the samples were sintered, silver paste was applied on both sides of the sample using a simple paint brush technique. In this, 6 pieces of scotch tape were stacked together and a hole, of 6 mm diameter, was punched in the stacked tape. The stacked tape was then placed on the surface of sintered sample so that the punched hole was aligned with the center of the surface. The silver paste was then applied on the punched hole and levelled off. Once the silver paste was dry, similar procedure was used to paint silver paste on the other surface of the circular sintered sample. Samples with silver paste were then sintered at 820℃ for 2 hours in air for adequate bonding of silver paste with sample surface. These samples were then used in an electrochemical testing system (details given later) for electrochemical impedance spectroscopy (EIS).

4.2 Fabrication of MS-SOFC via tape casting and co-sintering.

In this section, details are given for the experimental approach used in the study of MS-SOFC fabrication using tape casting and co-sintering. In tape casting, layers (tapes) of a material are casted by using a slurry of the material. The slurry, which can be organic or aqueous depending on application, is dropped on a substrate and then spread across the substrate using a blade. This results in a layer of the material of required thickness. Co-sintering is a high temperature sintering process where more than one material is stacked and sintered together.

4.2.1 Experimental approach

In the case of MS-SOFCs, cell components are casted using tape casting and then layers of these components are stacked together for co-sintering. Hence, the structural and chemical integrity of the final cell is dependant on the materials used, the quality of tape casting, and the effectiveness of co-sintering. Therefore, the approach used in this study relates to the following:

1. Selection of material for metal support and electrolyte which are compatible. YSZ and SDC were used as electrolyte, and a choice between Stainless-Steel (SS)-430L and 410L was made, based on compatibility with YSZ.
2. Tuning of tape casting procedure. This includes formulation of casting slurries which are stable i.e. the particles should be uniformly distributed, there should be no particle agglomeration, the particles should not sediment, and the slurry should not crack upon casting and drying.
3. Tuning of co-sintering temperature profile. This includes the study of behavior of individual cell components under different sintering temperature profiles. This leads to a better understanding of shrinkage behavior of cell components which can be used to tune the co-sintering profile to obtain defect free co-sintered cells.
4. Optimization of cell structure to reduce the amount of material used while achieving as simple cell structure as possible.

Once the sintering temperature profile is tuned, electrode catalysts (anode and cathode electro-catalysts) can be incorporated in the sintered cells for testing. Figure 4.3 shows the sequence in which the experiments were conducted.

Some of the experiments are coupled in iterative loops, i.e. based on the results of a subsequent experiment in that loop, the first experiment may be modified. This is the case with slurry formulation and tape casting. Once the layers are tape casted, based on the final form of layers, the slurry composition may be changed.

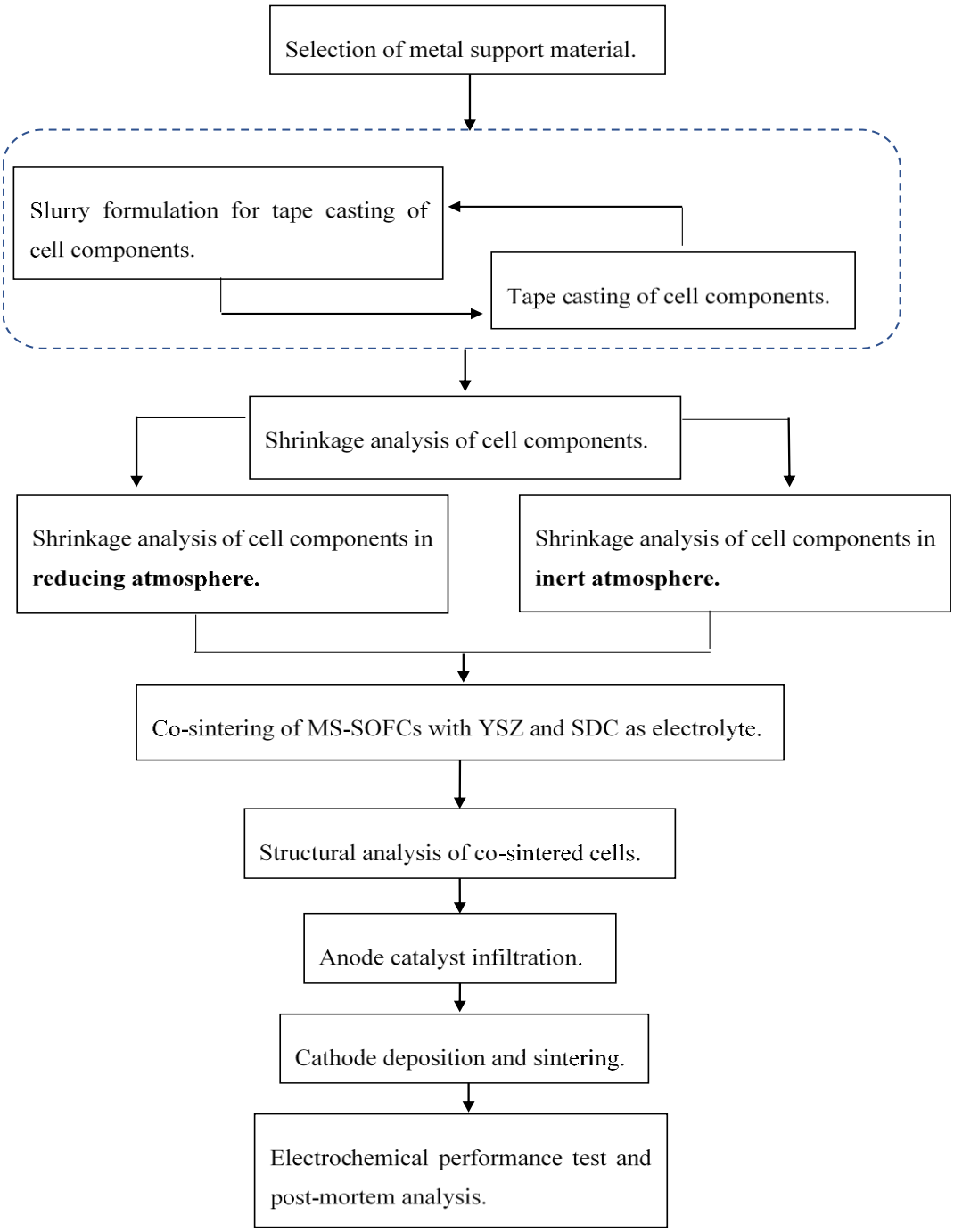

Figure 4.3: Sequence of experiments conducted in study of tape casting and co-sintering for MS-SOFC.

Selection of metal support material.

A choice between SS-430L and SS-410L was made based on their shrinkage compatibility with YSZ. For this purpose, dilatometry was used to study the shrinkage dynamics of both SS-430L and SS-410L. Commercial powder (VWR, Canada) for both materials of size 325 mesh (44 micron) were mixed with Poly Vinyl Butryl (PVB), Di-Octyl Phathalate (DoP), PMMA, and ethanol. The solution was ball milled overnight for complete mixing and then dried at 60°C for 6-8 hours. The resulting powder was ground using a ceramic mortar and pestle. Dried powders were pressed, at 343 MPa for 2 minutes, using a hydraulic press and a molding die set with a rectangular cross-section (6mm by 8mm). Pressed samples were then heat treated at 800°C in reducing atmosphere (5% H_2/95% Ar) to remove the organics. Burnt out samples were then run in a dilatometer in reducing atmosphere at a temperature of 1400°C. A high sintering temperature was used to study the complete shrinkage spectrum of the samples.

Slurry formulation and tape casting of cell components.

During fabrication of MS-SOFCs using tape casting and co-sintering, only a half-cell structure is co-sintered. This half-cell consists of the porous metal support, transition layers, and the electrolyte. The transition layers provide a smooth transition between metal support and electrolyte, and also act as a porous scaffold for anode catalyst. In this study three different types of transition layers were tried; the first one contained a 50/50 mass ratio of metal and electrolyte, the second one contained a 30/70 mass ratio of metal and electrolyte, and the third one contains only electrolyte mixed with pore former. Hence, slurries for 5 different layers were made:

1. Metal support.
2. 50/50 transition layer.
3. 30/70 transition layer.
4. Porous YSZ transition layer.
5. Dense YSZ electrolyte layer.

Even though different layers were casted the general requirements for all layer types from slurry formulation and tape casting were similar. It should be noted that slurry formulation and tape casting are co-dependant and hence results of tape casting were used to tune the slurry composition. The following are the requirements for slurry formulation and tape casting:

1. The slurry should be stable. That means that the particles should be uniformly distributed in the slurry, there should be no agglomeration of particles, and the particles should not sediment.
2. The slurry should have a viscosity which can be used with tape casting. That means that it should not be too viscous that it cannot be spread using a doctor blade, and it should not have too low viscosity so that it spreads by itself.
3. Upon drying the casted layer should not crack. This is governed by the type and amounts of organics in the slurry.

Numerous slurry compositions were tried for tape casting and the slurry composition was tuned accordingly each time. For brevity, only the final compositions of the slurries are given in Chapter 6. The effect of pore former content on the final porosity of metal support was also studied. It is critical that metal support be porous enough to allow for sufficient diffusion of fuel gas.

Tuning of sintering profile.

In co-sintering it is important that the materials being co-sintered attain similar shrinkage at the end of co-sintering. In case of MS-SOFC, a metal layer is stacked with a cermet (metal and ceramic) and a ceramic layer (electrolyte) and co-sintered. Hence it is important to study the shrinkage behavior of individual components (metal and ceramic) and the effect of sintering profile on their shrinkage behavior. As a requirement of metal in MS-SOFC the sintering atmosphere cannot be oxidizing (air) as it would lead to metal corrosion. This leaves the possibility of either inert or reducing atmosphere. Therefore, tuning of co-sintering profile requires both, the study of effect of sintering temperature profile and the sintering atmosphere. To achieve this, dilatometry of metal samples and ceramic samples was done in inert and in reducing atmosphere. The difference in sintering temperature profile was that of ramping temperature between 1000℃ and sintering temperature (1350℃). The reason for change only after 1000℃ is that neither metal (SS-430L) nor ceramic (YSZ) shrinks below 1000℃. Through this type of experiment the following information is evaluated:

1. Temperature at which shrinkage starts for metal support and YSZ under different ramping rates and sintering atmospheres.

2. Temperature required to reach maximum shrinkage for metal support and YSZ under different ramping rates.
3. Calculation of shrinkage rates of metal support and YSZ samples under different ramping rates and atmospheres.
4. Shrinkage of metal support and YSZ upon reaching the sintering temperature (1350°C) under different ramping rates and atmospheres.
5. Final shrinkage of samples after dwell at the sintering temperature.

The above information can be used to tailor a co-sintering profile which can be used for co-sintering of the metal support and YSZ so that the cells are free of physical defects (warping, delamination, cracking, etc.)

Co-sintering of MS-SOFC half-cells and structural analysis

Once the co-sintering profile is determined based on dilatometry analysis of individual components, MS-SOFC half-cells were co-sintered. This, in a way, is the application of information gained from dilatometry to real scenario. Since the shrinkage dynamics of individual component are different than that of stacked component during co-sintering, tuning of the co-sintering process of stacked half-cell might be necessary. The required changes in the co-sintering procedure were based on the physical appearance of the co-sintered samples (e.g. cracks, delamination, direction of warping).

MS-SOFCs with YSZ and SDC as electrolyte were both fabricated. The procedure of making green samples for co-sintering is given in Chapter 6.

Anode catalyst infiltration and cathode deposition.

The anode catalyst was infiltrated into the porous metal support using vacuum solution infiltration which was followed by printing of cathode ink on the YSZ surface of co-sintered samples.

The anode electro-catalyst was infiltrated into the porous metal support using vacuum assisted solution infiltration. Aqueous solution containing nitrate salts of the anode catalyst (nickel) and samarium and cerium (1:4 molar ratio for samarium and cerium, and 55:45 for nickel and samarium-cerium) was vacuum impregnated into the porous metal support. Figure 4.4 shows a labelled picture of the apparatus used for vacuum infiltration of anode electro-catalyst.

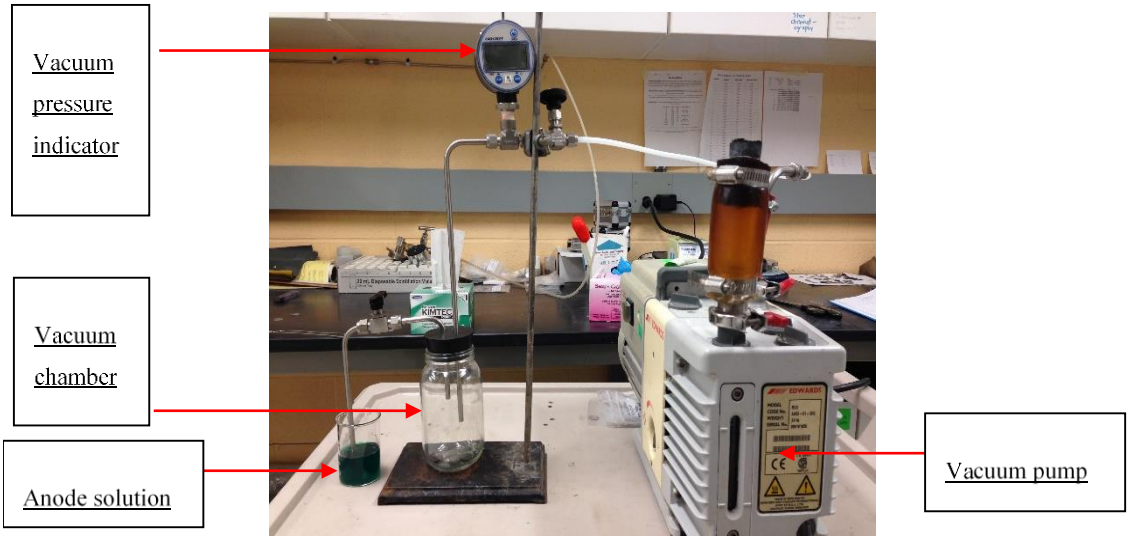

Figure 4.4: Picture of apparatus used for anode electro-catalyst infiltration.

The infiltrated samples were heat treated at 400℃ for 5 minutes to thermally break down the nitrates to form oxides. Infiltration and heat treatment cycle was repeated until a 10 mass % loading, based on mass of co-sintered half-cell, was achieved. Characterization of the resulting cell was done to evaluate the following:

1. Whether the nitrate salt solution turns to metal oxide powder of desired composition. This was done by heat treating metal nitrate solution and running the resulting powder in XRD.
2. Mass gain per infiltration cycle. This was done by weighing the sample before infiltration and then again after heat treatment. The difference in mass represents the mass of electro-catalyst loaded into porous metal support and transition layer.
3. Since heat treatment after every infiltration is done in air, its effect on metal support is important. Hence TGA of porous metal support was done to assess the effect of heat treatment cycle on the extent of oxidation of metal during these cycles.
4. To assess the efficacy of solution infiltration (whether NiO/SDC powder is uniformly distributed), SEM, coupled with EDX, of the cell cross-section was used.
5. To assess the effect of cathode sintering (1100℃ for 2 hours in argon) on the anode electrocatalyst powder, SEM-EDX of anode side full cells was done after cathode application and sintering. Since cathode sintering is at high temperature, it may lead to

micro-structural changes in NiO/SDC powder in the porous metal support and transition layer.

For cathode, a simple printing method was used. In this method, two pieces of scotch tape were stacked together and then a hole (6 mm diameter) was punched. The hole was placed in the center of the electrolyte surface, and the cathode ink was dropped on the hole. Dropped ink was then leveled off using a blade and the tape was removed. This left a circular printed cathode on the electrolyte surface. Ex-situ sintering in inert atmosphere at 1100℃ for 2 hours was used for cathode bonding to the electrolyte. Micro-structural analysis of the cathode was done using SEM for a full cell cross-section.

Electrochemical Performance testing

Full MS-SOFCs were tested for electrochemical performance. Tests were done with hummidified H_2 as fuel and air as oxidant and the operation temperature was 700℃. OCV measurement, polarization curve measurement and EIS were used to assess the performance of the fabricated cells. The setup of testing station is described in section 4.3 under the heading electrochemical testing.

4.2.2 Experimental procedure and details for slurry formulation and tape casting

As mentioned previously, different types of cell component layers were used in the fabrication: the metal support, the transition layers, and the electrolyte layer. The procedure and the chemicals used in the synthesis of the transition layers and electrolyte were similar as opposed to metal support layer. The primary reason for different procedures is that metal particles are denser (7.7 g/cm^3) compared to YSZ particles (6.1 g/cm^3), which tends to make the metal particles' sedimentation easier. Also, the way YSZ (metal oxide) particles interact with the organics used in the slurry is different than that for stainless-steel particles. Since the research is not about interaction of these particles in a colloidal system, no quantitative work was done to characterize these suspensions.

Slurry formulation for the metal support layer.

Stainless steel powder of 430L grade (Alfa Aesar, VWR-Canada) was used in the metal support. The slurry for tape casting was based on Acetonitrile and Poly Ethylene Oxide (PEO), which was used as the binder and viscosity increasing agent. Since the density of bulk SS-430L is high the sedimentation of powder can happen quickly (approximately in one hour). However, the viscosity of the solution (acetonitrile and PEO) can be varied to control the sedimentation of the powder. Also, the amount of SS-430L powder used will influence the density of the casted layer. After trial and error, the composition of slurry was fixed based on visual inspection: agglomeration or not of particles, sedimentation, and slurry viscosity. The particles in the slurry should not agglomerate and settle down. Also, the slurry should have the right viscosity; if the viscosity is too high the slurry will have difficulty spreading, and if it is too low it will overspread. First, PEO was mixed with acetonitrile in a mass ratio of 1:14 and ball milled for 24 hours. The mixed slurry was labelled "MS-Preliminary Slurry". This ratio gave a MS-Preliminary Slurry with a honey like consistency. Then, in 12 grams of MS-Preliminary Slurry, 7.2 grams of SS-430L powder was mixed using a variable frequency vortex mixer (VWR, Canada). To induce pores in the metal support structure an organic pore former, Poly (methyl methacrylate) PMMA, was used. 12.5 mass % with respect to the mass of SS-430L powder was used for pore former. Pore former was added to the slurry while mixing on a vortex mixer. The reason for this was to avoid any agglomeration of PMMA particles. The slurry was allowed to sit for one minute to remove any air bubbles before casting.

Slurry formulation for transition and electrolyte layer

The electrolyte and transition layer slurries were based on ethanol and toluene. Poly Vinyl Butyral (PVB), Santicizer S-160, and Hypermer KD-1 were used as binder, plasticizer and dispersant, respectively. The slurry synthesis was carried out in two steps where a "preliminary slurry" was made in parallel to a "base slurry". The preliminary slurry is a slurry containing the binder and plasticizer, whereas the base slurry contains the powder of desired material and dispersant. The base slurry is made separately with only dispersant and powder of desired material so that the particles are well distributed by the action of dispersant. If all the components were mixed together from the start there might be some particle's agglomeration because of the presence of binder and plasticizer. The preliminary slurry is a mixture of solvents (ethanol and toluene), PVB, and Santicizer S-160 ball milled for 24 hours. The base slurry is a mixture of solvents (ethanol and

toluene), Hypermer KD-1 (dispersant), and base powder (YSZ in case of electrolyte and YSZ-stainless-steel in case of transition layer). For the base slurry, ethanol and toluene were mixed with Hypermer KD-1 first to achieve a homogeneous solution, and then YSZ was added to the slurry. This slurry was ball milled for 24 hours. After separately ball-milling the preliminary and base slurries, they were mixed together for 6 hours using a ball mill.

For the electrolyte slurry, once the preliminary slurry and base slurry were mixed for 6 hours, the slurry was tape casted to a thickness of 150 microns.

In the case of the transition layer only the required percentage of YSZ was added to the base slurry initially. SS-430L was only added at the end, when the base slurry and preliminary slurry are already mixed for 6 hours. The reason for this is uniformity of the final slurry; it was observed that if SS-430L powder is added to the base slurry with YSZ the base slurry becomes very viscous and it is difficult to mix it with preliminary slurry afterwards. Hence, SS-430L powder and pore former (PMMA) were added to the mixture of the base slurry and preliminary slurry while mixing on a vortex mixer.

As in the case of metal support slurry, this was an iterative process. Hence only the final slurry composition is reported in Chapter 6.

Details of tape casting parameters

A table top tape caster (MTI corp., USA) was used for tape casting the samples. Silicon coated mylar sheet was used as the tape casting substrate. Table 4.1 gives out the casting thickness of all cell components.

Table 4.1: Casting thickness of cell components.

Cell component	Casting thickness (microns)
Metal support	750
50/50 MS/YSZ transition layer	300
30/70 MS/YSZ transition layer	300
Porous YSZ transition layer	300

Dense YSZ for electrolyte	150

The details of the materials used in this work are given in table 4.2

Table 4.2: Details of chemicals used.

Material	Vendor
Stainless Steel (400 series)	Alfa Aesar, VWR-Canada
YSZ tape casting grade powder	Fuel Cell materials, USA
SDC tape casting grade powder	Fuel cell materials, USA
Polyethylene Oxide (PEO)-400000	Sigma Aldrich
Poly(methyl methacrylate) (PMMA)	Scientific Polymers Inc., USA
Poly Vinyl Butyral (PVB)	Scientific Polymers Inc., USA
Santicizer S-160	Tape Casting Warehouse Inc., USA
Hypermer KD-1	Tape Casting Warehouse Inc., USA
Acetonitrile	Chem-Store-University of Waterloo
Ethanol	Chem Store-University of Waterloo

4.3 Apparatus and techniques used

This section gives the details of the apparatus used in the physical and electrochemical characterization of SDC with and without copper, and of MS-SOFC.

4.3.1 X-Ray Diffraction

X-ray diffraction was used to identify the crystal structure including the basic crystal type and crystal lattice parameters. The measurement was conducted using Bruker D8 Focus X-Ray diffractometer (Bruker, Germany) available at the chemical engineering department at University of Waterloo. SDC with and without copper, and NiO/SDC synthesized for MS-SOFC were

analysed through XRD. Powders of each sample was distributed on the sample holder using a glass slide to make the surface even. Later, the sample holder was loaded on the sample holder tray (attached to the equipment). The tray could carry 8 samples at the same time. The tray was then recalled into the equipment. For XRD measurement the X-Ray generator was supplied with a voltage of 40 kV and a current of 40 mA. CuKα radiations, with a wavelength (λ) of 1.5425 Å, were used and the sample was rotated between 2Θ values of 5-110°.

Eva software was used to identify the crystal structure, and peak positions from the generated XRD spectra.

4.3.2 Scanning Electron Microscopy (SEM)

Essentially, SEM-EDX was used for sintered samples of electrolyte disks (SDC with and without copper) and cross-sectional analysis of co-sintered half-cells for MS-SOFC. Preparation of SDC samples with and without copper for use in SEM is given in section 4.1.2 whereas preparation of the half and full MS-SOFCs is given in Chapter 6.

SEM Zeiss Ultra Plus, SEM LEO 1530 and ESEM available at the Waterloo Advanced Technology Lab (WATLab) were used for SEM and EDX analysis. All samples were coated with a 10 nm thin gold layer using sputtering equipment available at WATLab. Secondary Electrons (SE) and Back Scattered Electrons (BSE) were used to take SEM images of varying magnifications.

4.3.3 Dilatometry Analysis

Dilatometry (DIL 402 dilatometer, Netzsch) was used to study the shrinkage behavior of SDC with and without copper, metal support used in MS-SOFC (made from SS-430L), and YSZ for electrolyte in MS-SOFC. The results obtained gave data pertaining to time, temperature and linear shrinkage of samples. Linear shrinkage is the dimensional change as a percentage or fraction of initial dimension of sample (eq. 4.3).

$$Linear\ Shrinkage = \frac{\Delta L}{L} \qquad (4.3)$$

Results were analyzed based on plots between linear shrinkage and temperature and linear shrinkage and time. The plots were used to identify the sintering set off temperature, shrinkage rate, temperature at which maximum sintering is achieved, time required for sintering, and Coefficient of Thermal Expansion (CTE).

Shrinkage rate was taken as the change in linear shrinkage per unit time.

4.3.4 Electrochemical Testing

Electrochemical testing was done using the electrochemical testing station available in the lab. Essentially, it is composed of a reaction tube housed in an electrically heated furnace, gas mass flow controllers connected to the reaction tube, and current collectors from the reaction tube connected to the electrochemical testing stations (solartron 1287 and 1260). Figure 4.5 shows a schematic of the testing assembly (setup of reaction tubes). The electrochemical testing equipment can run regular electrochemical tests like cyclic voltammetry, polarization testing, potentiostatic measurements, galvanostatic measurements, and EIS.

The electrical furnace houses two reaction tubes, one for the anode side and one for the cathode side. Each reaction tube is made of two concentric tubes. The inside tube is made of quartz while the outside tube is made of alumina (Arklay S Richard Inc, USA). The inside quartz tube is used for flow of gasses to the cell and the annulus space (between inside and outside tube) is for the flow of gasses coming from the cell. Both reaction tubes are fixed in a special Swagelok fitting on outer ends, while the inside ends (inside end is inside the furnace) is attached to the cell. The swagelok fitting has a spring fitted inside on which the inside quartz tube, in both reaction tubes, sit. The purpose of the spring is to provide some forward push to the quartz tube so that it makes firm contact with the cell on the other end of the reaction tube. This also means that without a sample the quartz tube slightly protrudes outwards from the alumina tube. To make electrical connections, the inside end of the quartz tube (the end in contact with the cell) is covered with a silver mesh. The silver mesh is in contact with a silver wire which goes in to the actual electrochemical testing station (Solartron 1260 and 1287). There is a slight difference in the procedure for securing symmetrical electrolyte sample for conductivity analysis and that for full cell electrochemical testing.

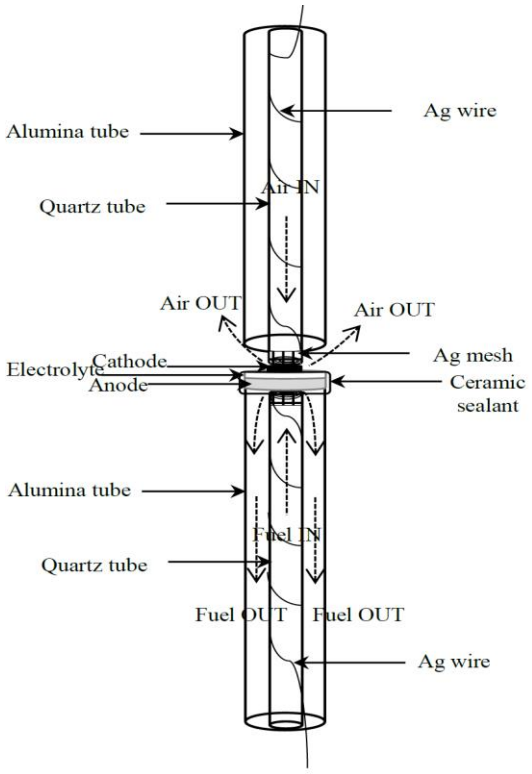

Figure 4.5: Schematic of reaction tube assembly for EIS and Electrochemical testing.

Assembly for symmetrical electrolyte samples

EIS for electrolyte was done in air. Symmetrical cell with silver paste was placed between the top and bottom reaction tube. The inside ends of the quartz tubes were covered with mesh and touching the silver paste on either side of the sample. The furnace housing was sealed and ramped to 400℃. Tests were conducted between 400-800℃ with an interval of 50℃.

Assembly for MS-SOFCs

In electrochemical performance testing, H_2 is used on the anode side and air on the cathode side. To avoid any leakage of fuel to the cathode side, the anode side of the cell (metal support side) was sealed to the bottom the reaction tube. Once the cell was placed on the reaction tube, cermabond (Aremco, USA) was used as a sealant to seal the cell to the bottom reaction tube. The seal was dried in ambient air for 1 hour before curing at 92℃ for 2 hours first and then at 262℃ for 2 hours. Once the seal was in place, the top reaction tube was placed on the cell such that the inner quartz tube was touching the printed cathode. The temperature of the furnace was ramped up

to 700°C with 80 mL/min flow of dry H_2 on the anode side and 86 mL/min flow of air on cathode side.

Once at the operating temperature electrochemical performance tests were performed.

Electrochemical Impedance Spectroscopy (EIS)

Electrochemical Impedance Spectroscopy (EIS) is a frequency dependant electrochemical characterization technique. In the case of solid electrolyte, the current passes through the electrolyte using two different pathways, through grain interior and through grain boundary. Both mechanisms have different time constants and hence behave differently (i.e. show different resistances). Using AC voltage bias with varying frequencies it is possible to differentiate between the resistance or impedance behavior of these two mechanisms. In the experiments, a frequency-based AC voltage signal was applied which can be written mathematically as:

$$E' = E_o \sin(\omega t) \qquad (4.4)$$

In the above equation E' is the actual voltage signal, E_o is the set voltage bias, t is the time, and ω is the angular frequency ($\omega = 2\pi f$). When this signal is applied across the sample a resulting current passes through the system of the magnitude:

$$I' = I_o \sin(\omega t + \varphi) \qquad (4.5)$$

Where I' is the actual current passing through the sample, I_o is the output current signal, and φ is the phase angle. Analogous to DC circuit relation between voltage-current-resistance, a relation can be constructed for AC voltage and current.

$$Z = \frac{E'}{I'} \qquad (4.6)$$

Where Z is the impedance of the system. This relation, in time domain, can be converted to a complex number in frequency domain [124] as:

$$Z = |Z| \exp j\varphi = |Z| \cos(\varphi) + j|Z| \sin(\varphi) = Z' + Z'' \qquad (4.7)$$

In the above equation Z' is the real part of impedance and $Z^{"}$ is the imaginary. EIS can be used for conductivity measurement of electrolytes and for ohmic and polarization resistance measurement for a full cell under working conditions.

In case of conductivity measurement using EIS, the Nyquist plot can be plotted between imaginary and real impedance. Figure 4.6 below shows a typical Nyquist plot for electrolyte materials [125].

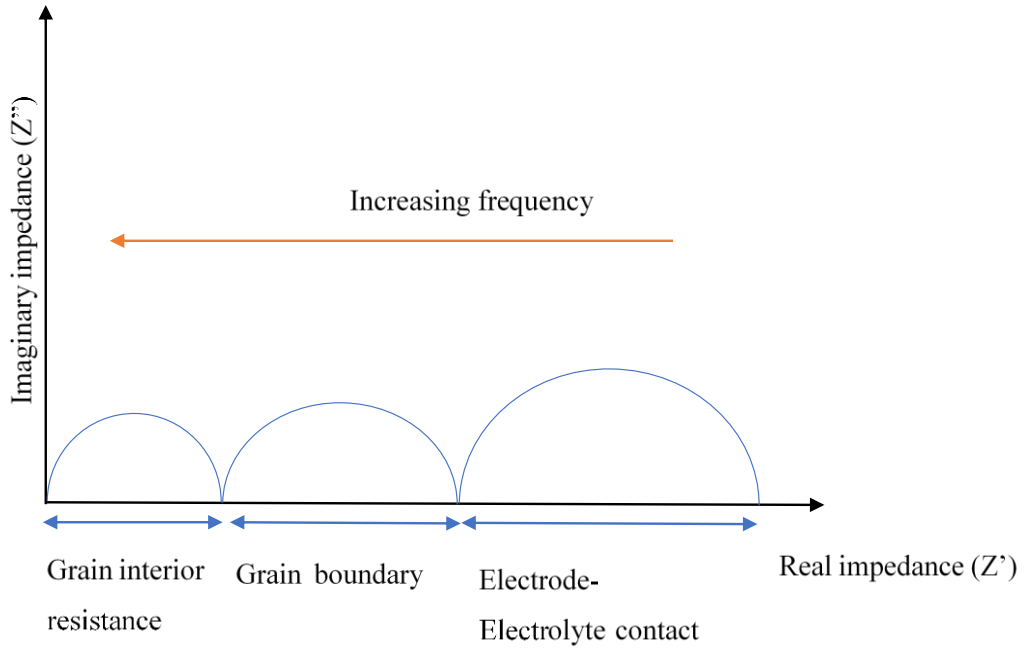

Figure 4.6: Typical Nyquist plot for a solid electrolyte.

In a Nyquist plot each semicircle represents a different conduction mechanism, realized based on its time constant. In the case of a solid electrolyte the first semicircle represents grain interior conduction, the second semicircle represents grain boundary and the third semicircle represents electrode-electrolyte interface/contact resistance. Values at the x-intercepts are used as the resistance values. From the Nyquist plot, equivalent circuit data fitting is used to predict the actual resistance values. Equivalent circuits are normal RC circuits with both active and passive electrical components sequenced in a way which produce same impedance response as that of the test sample. In principle an equivalent circuit is the reflection of conduction mechanism of a material on to electrical circuit components. In the case of solid electrolytes, commonly used circuit elements are inductor, resistor, and Constant Phase Element (CPE). CPE represents the capacitance

or charging of material. Every semicircle can be represented by a parallel combination of resistor and CPE and the entire Nyquist plot can be represented by a series combination of all the parallel resistor-CPE circuits. For analysis, Z plot and Z view (Scribner Associates, USA) software were used. Figure 4.7 shows an example of equivalent circuit used in this study.

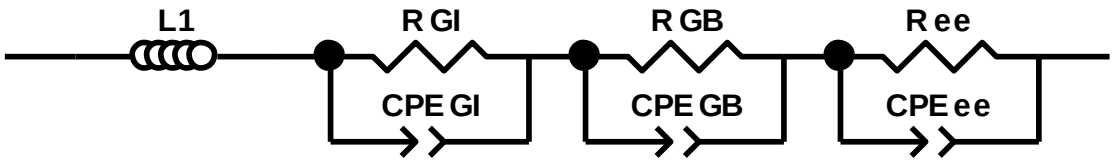

Figure 4.7: An example of equivalent circuit.

In the present study, during EIS experiments an AC voltage bias of 10 mV in the frequency range of 0.1 Hz to 1 MHz was used. The temperature range for experiment was set between 400-800°C in air atmosphere. In air it is assumed that oxygen ion conduction would be dominant whereas in inert or reducing atmosphere (low oxygen partial pressure) electron conduction can become significant. The dependence of conductivity in MIEC like doped ceria on oxygen partial pressure is given by

$$\sigma = \sigma_O + \sigma_e.(P_{O_2})^{-\frac{1}{4}}$$

In the above equation 'σ' is the total conductivity and subscript 'o' and 'e' represent oxygen and electron conductivity. Conductivity of a sample can be calculated using resistances calculated through EIS using the equation:

$$\sigma = \frac{l}{R.A}$$

Where 'l' is the sample thickness, 'R' is the resistance and 'A' is the active area. In our case the active area was taken as the area of the silver paste which was equal to 0.283 cm^2. The conductivity had the units of $S.m^{-1}$ or $S.cm^{-1}$. Sample calculation for electrolyte conductivity and conduction activation energy is given in Appendix B.

In case of full cell ohmic and polarization resistance measurement using EIS, Nyquist plot shows two semi-circles. The one at higher frequency is attributed to the ohmic resistance of the cell and the one at lower frequency is attributed to the polarization resistance. In case of a full cell ohmic resistance represents the resistance to charge conduction through a cell component and at the interface of two components. Polarization resistance, on the other hand, is a reflection of resistance to electrode process like charge transfer reactions, etc.

4.3.5 Porosity measurement

Porosity measurement of sintered metal support samples was done using vacuum assisted oil impregnation. Sintered samples were weighed, and the mass was recorded as dry mass. The samples were placed in a chamber and vacuum was induced in the chamber using a vacuum pump. Samples were left in vacuum for 5 minutes before filling the chamber with oil of known density. Vacuum was slowly increased to atmospheric pressure and samples were left in the oil for 20 minutes. The samples were then taken out of the oil and a non-absorbing paper was used to wipe the excess oil on the surface. The samples were weighed again, and the mass recorded as wet mass. The difference between wet mass and dry mass is that of the impregnated oil. Using the density of SS-430L and oil, and the mass of SS-430L and oil, volume of each phase and porosity was calculated (sample calculation shown in Appendix A). The apparatus used for oil impregnation was the same as that used for anode electro-catalyst infiltration for MS-SOFCs. A picture of the apparatus is shown in Figure 4.4.

Chapter 5 Use of Sintering Aid with SDC Electrolyte

5.1 Introduction

In conventional methods, electrolyte materials used in SOFCs, be it YSZ, SDC or others, are sintered at high temperatures, up to 1400°C, to allow for maximum densification of the electrolyte. The reason behind this is to make the electrolyte gas tight so that there is no short circuiting of reactants, which leads to inefficiencies. Reaching this high temperature contributes to the manufacturing cost which acts as a hinderance in the commercialization of this technology. Also, with advances made in third generation SOFCs, or MS-SOFCs, high sintering temperature can be a problem in cases where the metal support is pre-sintered. Similarly, for MS-SOFC the use of reducing atmosphere for sintering can lead to reduction of cerium (IV) oxide to cerium (III) oxide. To reduce the exposure of metal support and SDC to high temperature, complex techniques like Plasma Spray Deposition (PSD), Pulsed Laser Deposition (PLD), and sputtering have been employed. Thermal spray deposition techniques are normally used with a pre-sintered metal support. Although they have been more popular there are some limitations to the use of these techniques in case of MS-SOFCs. It has been reported that electrolytes deposited using thermal spray deposition like atmospheric plasma spraying are not fully dense leading to inefficiencies in cell performance[24,25]. Also, the use of focused plasma can lead to localized hot spots on the porous metal substrate which can lead to metal support warping[26]. Another smaller limitation is the long processing times required, where it has been reported that processing rate can be as low as 1-2 µm/hr[126]. Hence, it would be desirable to derive a procedure using conventional ceramic processing technique to lower the sintering temperature, while minimizing negative effect on cell performance. Since SDC has been known to show a comparable conductivity at lower temperatures in comparison to YSZ, this work deals with the reduction of sintering temperature of SDC. As outlined in chapter 2 numerous methods can be used to reduce the sintering temperature; however, the use of sintering aid has been labelled as effective in the past [31]. It is important to fully characterize the system of electrolyte when using sintering aid; that is microstructure, shrinkage behavior and electrochemical properties should be fully characterized. In the past, several different transition metals have been employed as sintering aids including iron [109],

cobalt[115,127], lithium[125], bismuth[114], zinc[116], and copper [33,34,111]. Amongst these, cobalt, iron and copper have been the popular choices. The cost of cobalt, however, makes it a difficult choice as a sintering aid. In the case of iron oxide as sintering aid it has been reported that low amounts of iron doping (less than 0.5 mol%) can lower the total conductivity slightly. In the case of copper most of the work done in the past has been on copper content of 1 mole % with Gadolinium Doped Ceria (GDC) [31,33,34,111]. Hence copper was chosen as the sintering aid in this study where copper content was varied between 0 and 5.0 mol%. The objective of the study is to shed light on how copper content affects the crystal structure, sintering dynamics, and conductiity of SDC.

The first task of this work is the study of the crystal structure resulting from sintering aid incorporation to SDC powder. The objective of this task is to establish whether copper ions go inside the cubic fluorite crystal structure of ceria and if there is a solubility limit. The second task is the characterization of the microstructure and the shrinkage behavior of the sintered samples. Microstructure is characterized through SEM-EDX and gives a general idea about observable porosity or surface porosity of the sintered samples, about the presence or not of secondary phases and information about grain size and shape. The shrinkage behavior, on the other hand, deals with the dynamics of the sintering process. With the help of the shrinkage curves, sintering set-off temperature, sintering time, maximum shrinkage, temperature required for maximum shrinkage and CTE can be measured. The last task is the characterization of effect of copper sintering aid on the electrochemical performance, more particularly, the determination of the electrolyte conductivity.

5.2 Experimental procedure

Copper was used as sintering aid with SDC in this work. Varying content of copper in the form of copper nitrate hydrate was added to a metal nitrate-glycine solution of samarium and cerium. Electrolyte powders were prepared in lab using Glycine Nitrate Combustion (GNC) process. Nitrate hydrates (from VWR, Canada) of desired metals were mixed with glycine in De-Ionized (DI) water. Glycine in this reaction is used as an oxidant and a fuel at the same time. The solution was heated over night at 90°C to form a gel. This gel was later transferred to ceramic crucibles and

combusted on a heating plate. For comparison purpose, undoped Plain Samarium Doped Ceria (PSDC), 0.1 mol% copper doped SDC (0.1CSDC), 0.5 mol% copper doped SDC (0.5CSDC), 1.0 mol% copper doped SDC (1.0CSDC), and 3.0 mol% copper doped SDC (3.0CSDC), and 5.0 mol% copper doped SDC (5.0 CSDC) were prepared. After combustion the powders were calcined at 700℃ for 2 hours in air.

The characterization of samples can be organized into two categories; physical and conductivity.

5.2.1 Physical Characterization

For physical characterization, XRD, SEM, and dilatometry were used. For XRD analysis, calcined powder for all samples were run in Bruker D8 Focus X-Ray diffractometer (Bruker, Germany). Diffraction angles (2Θ was fixed between 5-110°) were used with CuKα radiation with a wavelength (λ) of 1.5425 Å. For SEM analysis, calcined powders of different samples were pressed into circular disks of 20 mm diameter at 250 MPa for 2 minutes and were sintered at 1100℃ for 5 hours in air. Sintered samples were then observed under SEM. Additional PSDC sample was also sintered at 1350℃ to act as a standard reference sample. For dilatometry, samples with rectangular cross section were pressed using the calcined powder. The dimensions of the cross-section are 6 mm by 8 mm. The samples were pressed at 250 MPa for 2 minutes. Pressed samples were then used in a horizontal push rod dilatometer (DIL 402 C, NETZSCH). The sintering profile used for dilatometry tests is given in Table 5.1.

Table 5.1: Temperature profile used for dilatometry analysis.

Step Number	Step description
1	Heat up to 400℃ in air at 3℃/min.
2	Dwell at 400℃ for 30 minutes.
3	Heat up to 1000℃ at 3℃/min.
4	Dwell at 1000℃ for 10 minutes.
5	Heat up to 1350℃ at 2 ℃/min
6	Dwell at 1350℃ for 5 hours.

High sintering temperature was used to allow for comparison between a standard PSDC sample sintered at a more conventional sintering temperature of 1350℃. Key parameters identified through the dilatometry analysis were sintering set-off temperature, temperature needed to attain maximum shrinkage, time to achieve maximum shrinkage, and CTE.

5.2.2 Conductivity Characterization

For conductivity analysis calcined powders for different samples were pressed into circular disks of 20 mm diameter at 250 MPa for 2 minutes. Pressed samples with copper were then sintered at 1100℃ for 5 hours whereas PSDC was sintered at 1350℃ for 5 hours. Sintering temperature of 1350℃ for PSDC was chosen so that PSDCs performance is not compromised. This means that electrochemical performance of copper doped samples should be tested against SDC sample which is sintered at conventional sintering temperature. Once the samples were sintered, silver paste was applied on both sides using 'printing', as described next. 6 pieces of scotch tape were stacked together and a hole (6 mm diameter) was punched in the stacked tape. Punched-stacked tape was then carefully placed on the cell so that the hole is in the center of the surface of the sintered samples. Silver paste (Electrochemical Systems Inc.) was then applied and levelled off on the punched hole. The applied paste was dried before turning over the cell and applying the silver paste on the opposite surface. Once the silver paste was deposited on both sides of the cell, it was heat treated at 820℃ for 2 hours in air to allow for bonding between the silver electrodes and the electrolyte disk. After sintering the samples were mounted on the test rig. A schematic of the test rig is shown in Figure 5.1.

A more detailed description of the testing station is given in chapter 4. The test rig consists of two concentric tubes on both sides of symmetrical cells. Outer tube is made of alumina and inner tube is made of quartz. The annulus space acts as the outlet passage for gasses while gasses flow in through the quartz tube. The test rig is placed in a vertical tubular furnace so that tests could be conducted at higher temperatures.

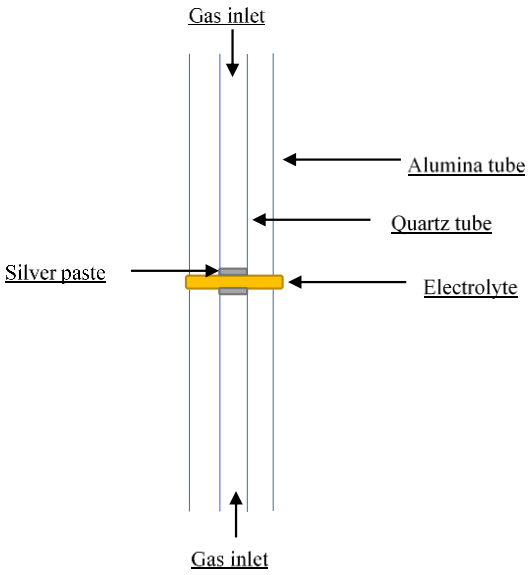

Figure 5.1: Schematic of test for rig for electrochemical testing.

For conductivity analysis, ionic conductivity was characterized using Electrochemical Impedance Spectroscopy (EIS). During EIS experiments A.C. potential bias of 10 mV was used between a frequency range of 0.1 Hz to 1Mhz. Generally, for ceramics or metal oxides Nyquist plot contains three consecutive semicircles where each semicircle represents a unique conduction mechanism (grain interior, grain boundary, and charge transfer between electrolyte and electrode). In a Nyquist plot, frequency decreases along the positive x-axis. The second x-intercept of each semicircle is taken as the impedance of that specific mechanism. In case of metal oxides the arc/semicircle corresponding to the highest frequency is for grain interior, the arc at medium frequency is for grain boundary and the arc at lowest frequency is for electrode-electrolyte interface [116]. To determine the impedance values from experimental results equivalent circuit fitting is used to find out conductivity components of grain interior, grain boundary and electrode-electrolyte interface. Each conductivity mechanism is represented by a parallel combination of Resistor (R_i)-Constant Phase Element (CPE_i) and overall each component is placed in series. Subscript ‘i’ stands for the component, in that ‘gi’ represents grain interior, ‘gb’ represents grain boundary, and ‘ee’ represents electrode-electrolyte. Once the resistance values are known the following equation is used to calculate the conductivity values.

$$\sigma = \frac{l}{R.A} \qquad (5.1)$$

EIS testing of symmetrical electrolyte samples was conducted between 400-800℃.

5.3 Results and Discussion

5.3.1 Physical characterization

Physical characterization of the samples comprises the studies of crystal structure, microstructure of sintered samples, and shrinkage behavior of samples in a given sintering profile.

Crystal Structure Analysis

The first step in physical characterization was to run the calcined powders of electrolyte under XRD for crystal structure characterization. The purpose was to see any obvious changes in the crystal structure as indication of whether copper goes inside the crystal and/or stays outside the crystal structure and segregates on the boundaries. Other than peak identification on the spectra, lattice parameter was also calculated to see the effect of copper content on the crystal structure. Table 5.2 shows the ionic radii of all cations involved in the crystal structure of SDC with and without copper.

Table 5.2: Ionic radii of cations in copper doped SDC [33][113].

Cation	Ionic radius (Å)
Cerium (IV)	0.97
Samarium (III)	1.08
Copper (II)	0.73

The crystal lattice parameter of ceria (CeO_2) is 0.541 nm [128]. The replacement of cerium ion with a bigger ion will lead to a stretch in the crystal structure which will increase the lattice constant, and vice versa. Figure 5.2 shows XRD spectra for PSDC, 0.1CSDC, 0.5CSDC, and 1.0CSDC, 3.0CSDC, and 5.0CSDC. From Figure 5.2 it is evident that there are no apparent

changes in the crystal structure of SDC when it is doped with copper up to a content of 5 mol %. Major peaks form at the same 2Θ values and there are no additional peaks in comparison to the fluorite crystal structure of ceria (same as that for PSDC).

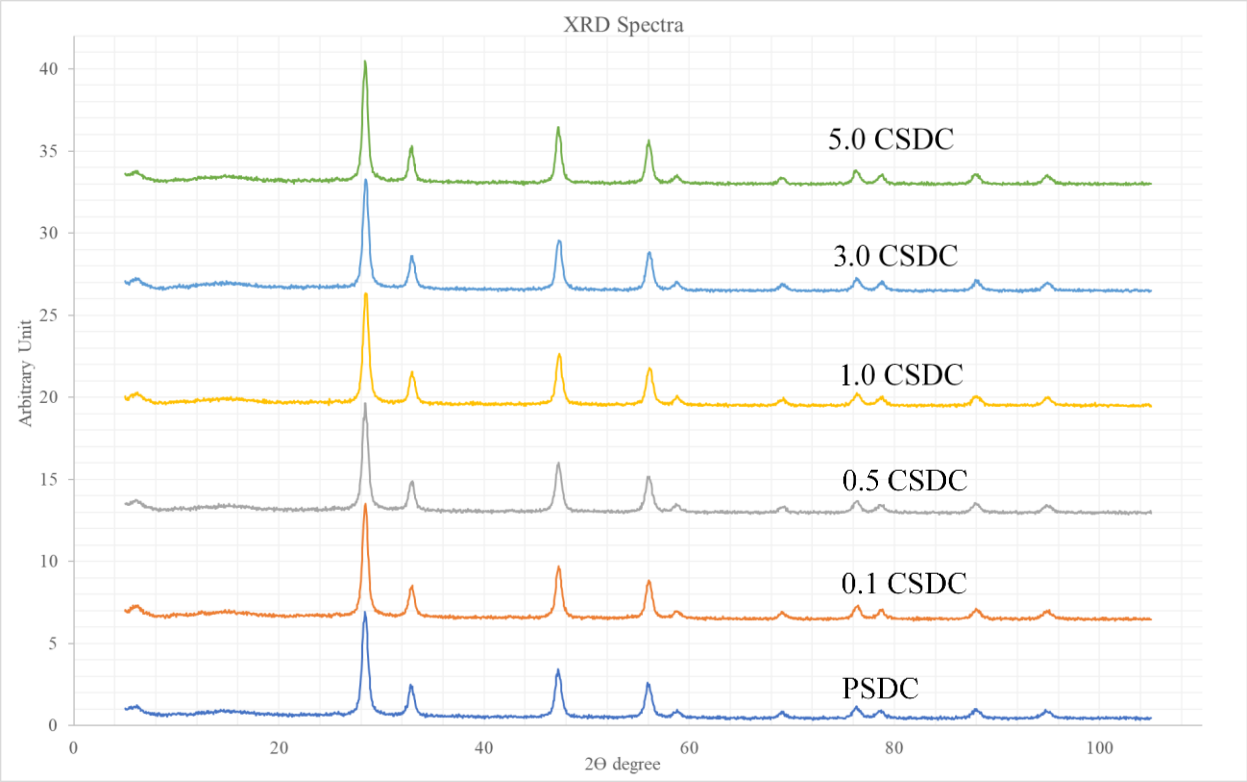

Figure 5.2: XRD spectra of different electrolyte samples.

It appears from XRD spectra and the lattice constant shown in Table 5.3 that copper forms a solid solution with ceria as there is no additional peak formation relative to XRD spectra of PSDC (Figure 5.2).

Table 5.3: Lattice constant for SDC with and without copper.

Sample ID	Lattice constant (nm) using peak (1,1,1)	Lattice constant (nm) using peak (2,0,0)
PSDC	0.5446	0.5455
0.1 CSDC	0.5436	0.5431

0.5 CSDC	0.5436	0.5429
1.0 CSDC	0.5435	0.5428
3.0 CSDC	0.5435	0.5426
5.0 CSDC	0.5427	0.5425

Increasing the amount of copper leads to a slight progressive decrease in the lattice constant. This points to the fact that copper ions are replacing cerium ions in the crystal structure as the ionic radius of copper ion is smaller than that of cerium ion (Table 5.2). It has been previously reported that lattice constant for SDC ranges between 0.5411 and 0.5450 nm depending on the calcination temperature and sintering [113]. Lattice constant calculated here falls within this range. Literature reporting the use of copper as sintering aid also shows a similar slight decreasing trend with the addition of copper [33][34]. GDC samples with 1 mol% copper addition has been reported to have a lattice constant of 0.54177 nm [34] and 0.54086 nm [33]. It can be seen that these values are smaller compared to lattice constant values for 1.0 CSDC determined here. The reason might be the use of gadolinium instead of samarium in the literature; gadolinium has a smaller ionic radius (1.05 Å) [109] than samarium (1.08 Å) [113]. The lattice constant for GDC (0.5425 nm) [109] is smaller than SDC (0.5450 nm)[113] to begin with. However, the addition of copper up to 5.0 mol% does not significantly decrease the lattice constant (only 0.35% decrease from SDC lattice constant).

The theoretical density is also an important parameter to see the effect of copper on the crystal structure of the material. Since it is assumed that both samarium and copper ions are replacing cerium ions in the crystal lattice and keeping in mind that ceria has cubic fluorite crystal structure the following equation can be used to compute the theoretical density [113].

$$d_{th} = \left(\frac{4}{Na.a^3}\right)\left((1-x-y)(M_{Ce} + xM_{Sm} + yM_{Cu} + \left(2 - \frac{(x+y)}{2}\right)M_O\right) \qquad (5.2)$$

where x and y are molar fractions of samarium and copper in a single crystal, respectively; M_i is the atomic weight of component 'i', Na is the Avogadro's number (6.022×10^{23}), and 'a' is the lattice constant. The calculated theoretical densities for each electrolyte are given in Table 5.4.

Table 5.4: Theoretical density of different samples.

Sample ID	Theoretical Density using (1,1,1) peak / ($g.cm^{-3}$)	Theoretical Density, using (2,0,0) peak / ($g.cm^{-3}$)
PSDC	7.10	7.06
0.1 CSDC	7.13	7.15
0.5 CSDC	7.12	7.14
1.0 CSDC	7.10	7.13
3.0 CSDC	7.03	7.07
5.0 CSDC	6.99	7.00

It is clear from Table 5.4 that theoretical density of samples first increases (addition of 0.1 mol% copper) and then decreases as the copper content is increased. When a dopant lighter and smaller in size than cerium is added to the ceria structure it can affect the density through two different ways. Firstly, it can increase the density by decreasing the lattice constant or unit cell volume and secondly it can decrease the density by decreasing the mass of unit cell. As seen in Table 5.3 the lattice constant does not change appreciably with copper addition, only 0.35 % change noticed with 5.0 mol% copper addition. However, the theoretical density does show a more significant change, a decrease of 1.42 % between PSDC and 5.0CSDC. This shows that copper shows a more pronounced effect on mass of a unit cell.

Microstructure of Sintered Samples

SEM was used to observe the microstructure of sintered samples and see whether they are fully dense or not. Figure 5.3 shows SEM images of electrolyte samples sintered at 1100°C in air for 5 hours. Pure SDC and 0.1CSDC sample are not fully dense, as many pinholes can be observed (Figures 5.3a and 5.3b). On the other hand, the 0.5, 1, 3, and 5 CSDC sample shows that the material has fully densified.

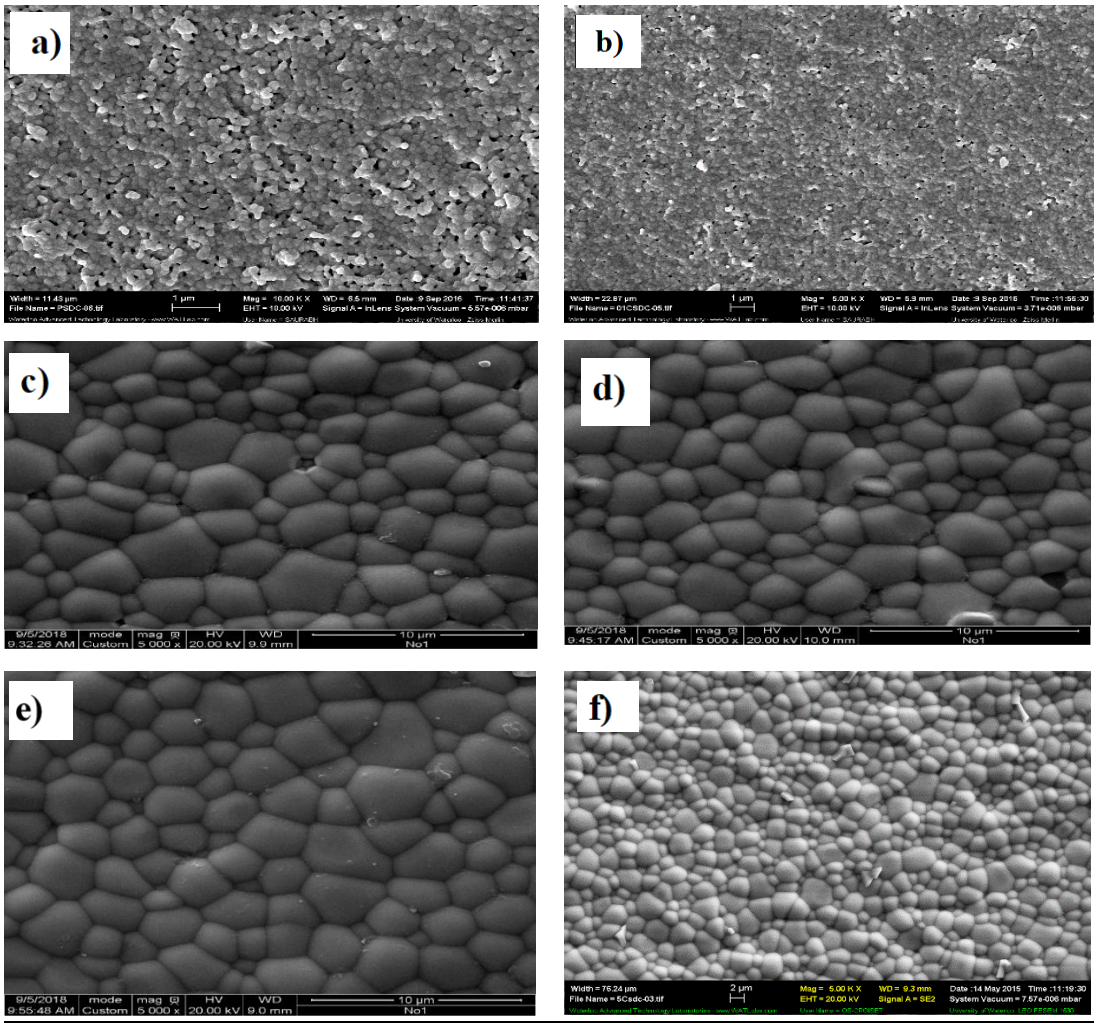

Figure 5.3: SEM images of electrolyte samples sintered at 1100°C; a) Pure SDC sample, b) 0.1 CSDC sample, and c) 0.5 CSDC sample, d) 1.0 CSDC, e) 3.0 CSDC, and f) 5.0 CSDC.

For PSDC and 0.1 CSDC not much grain coarsening is observed at 1100°C compared to other samples. Samples with 0.5 mol% and more copper show very similar microstructure and bi-modal grain size distribution after sintering. This is an indication of final stage of sintering, which commonly happens after the maximum contact is established between particles. During the final stage of sintering grain coarsening is observed where the bigger grains keep on increasing their size by "consuming" smaller grains. In our case, indication of final stage sintering for samples containing 0.5 mol% and more copper implies that either sintering starts at a lower temperature and/or shrinkage is faster than that for PSDC and 0.1 CSDC. From Figure 5.3 it is clear that 0.5 mol% copper doping is sufficient to enhance sintering of SDC so that near full density is achieved

at 1100°C. For comparison PSDC sample was also sintered at 1350°C (conventional sintering temperature) in air for 5 hours. Figure 5.4 shows the SEM image of the sintered sample.

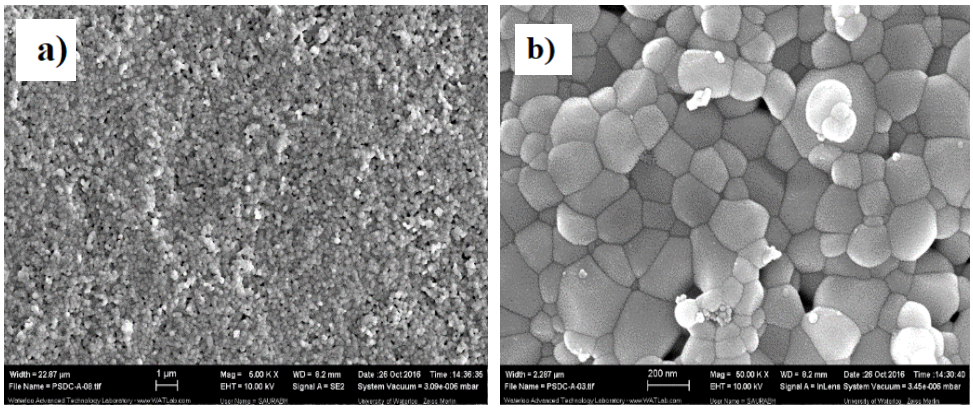

Figure 5.4: SEM of PSDC samples sintered at 1350°C; a) 5 KX magnification and b) 50 KX magnification.

Even at 1350°C sintering of PSDC does not show full density. From Figures 5.3 and 5.4 it appears that using 0.5 mol% copper in SDC can greatly decrease the sintering temperature (up to 200°C). Even though XRD results showed no additional phase for copper oxide, SEM showed an additional phase which was identified as copper oxide using EDX (see Figures 5.5 and 5.6). Back Scattered Electron (BSD) function can be used for phase identification in SEM. In this, electrons fired on the sample are back fired to the BSD detector. Bigger atoms back scatter electrons with more energy (due to higher chances of elastic collision) as opposed to smaller atoms.

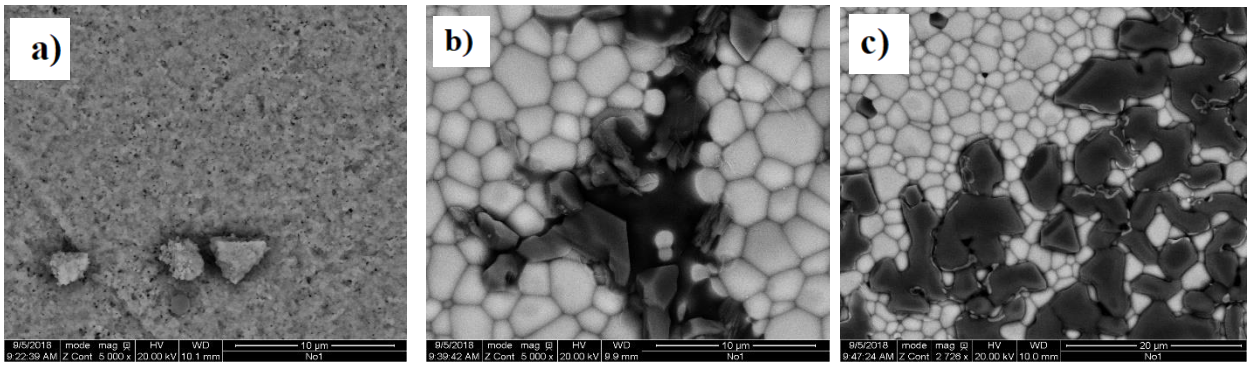

Figure 5.5: SEM in Back Scattered Electron (BSD) mode for a) 0.1 CSDC, b) .0.5 CSDC, and c) 1.0 CSDC sintered at 1100°C for 5 hours.

Based on the higher intensity of electrons back scattered from heavier atoms the image formed for heavier atoms is brighter compared to lighter atoms. Hence BSD can be used to identify different phases in a sample based on the color of the image. Figure 5.5 shows BSD images of samples containing 0.1, 0.5, and 1.0 mol% copper. In Figures 5.5b and 5.5c, SEM-BSD shows images with two different colors. Since cerium is heavier than copper, the ceria phase appears brighter. The dark colored phase is identified as copper oxide. Another feature visible in Figures 5.5b and 5.5c is the difference in shape of grains for doped ceria phase and copper oxide phase. Where doped ceria grains appear more spherical, the copper oxide seems to have faces. EDX was performed on Figure 5.5c to verify and assess the identity of the darker colored phase. This is shown in Figure 5.6. The presence of copper oxide phase implies that copper oxide promotes sintering of SDC by promoting liquid phase sintering. It has been reported that copper oxide forms a ternary phase with GDC [34], similarly it forms a ternary phase with SDC in this case. Transient liquid phase is formed during formation of this phase at high sintering temperature.

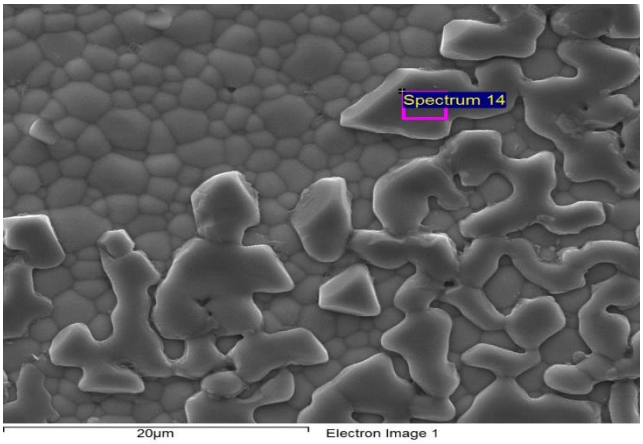

Element	Weight %	Atomic %
O K	14.74	41.83
Cu K	78.25	55.92
Ce L	5.85	1.9
Sm L	1.17	0.35

Figure 5.6: SEM and EDX of 0.5-CSDC sintered at 1100°C for 5 hours.

Since the basic requirement from SDC or SOFC electrolytes is oxygen conduction; the effect of formation of a secondary phase (CuO), and the dissolution of copper in crystal structure on the conductivity should be studied. In the first case, where copper forms an additional copper oxide phase at the grain boundaries the total conductivity of the sample might change. The reason for this is that copper oxide phase might exhibit a different conductivity than doped ceria phase. Another reason maybe the interaction of copper oxide with the surface of doped ceria. Presence of copper oxide on the surface can lead to changes in the defects present at the surface of doped ceria

which can lead to changes in conductivity at the grain boundary. In the second scenario if copper does not form an additional phase and continues to replace cerium in the crystal lattice, it might hamper the oxygen diffusion/conduction due to increased association enthalpy of oxygen vacancies [109]. This will happen as Cu^{+2} has a smaller ionic radius than Ce^{+4} (see Table 5.2). Even though 0.5 mol% copper addition seems enough for sintering, higher copper content is used to see whether increasing the amount of copper increases the conductivity of SDC and/or further lowers the sintering temperature.

Shrinkage Analysis of Samples

Dilatometry was used to study the dynamics of sintering for different samples. Figure 5.7 shows shrinkage curves of samples sintered up to 1350°C in air.

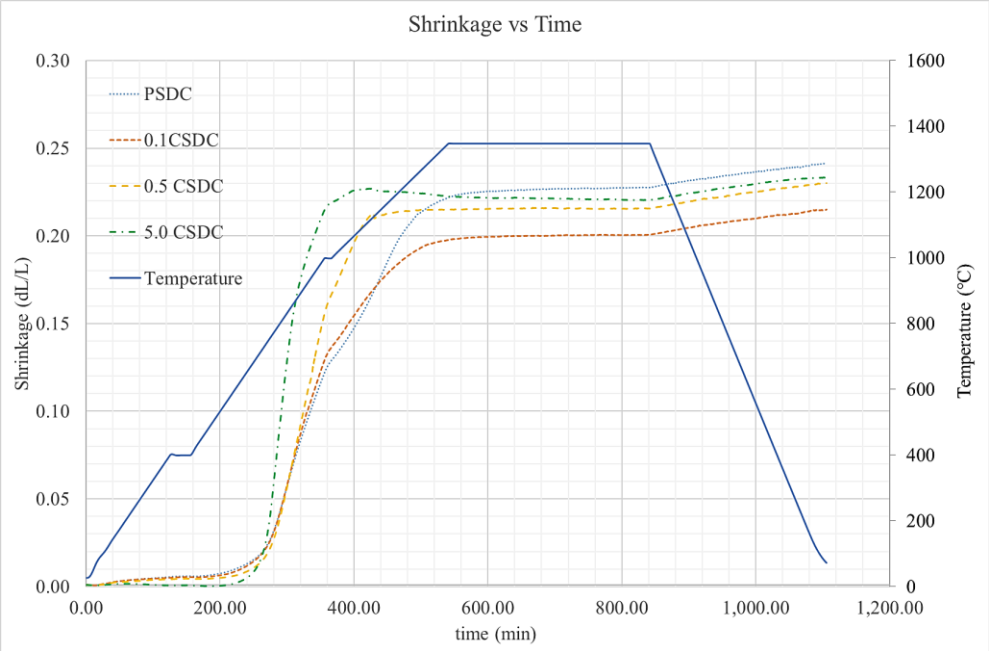

Figure 5.7: Shrinkage curve for SDC with and without copper doping; PSDC, 0.1 CSDC, 0.5 CSDC, and 5.0 CSDC.

The sintering set-off temperature is similar for all samples (slightly above 700°C). 0.1CSDC shows very similar trend to PSDC, where the sintering set-off temperature, and shrinkage rate are identical. The only difference in PSDC and 0.1CSDC is the maximum shrinkage; PSDC shrinks to a maximum value of ~23% whereas 0.1CSDC shrinks to a maximum value of ~20%. However, the rate of shrinkage increases for 0.5 mol% or more copper. This leads to copper doped samples

with more than 0.5 mol% copper attaining maximum shrinkage in a shorter time and before reaching the maximum sintering temperature used here (1350°C). The maximum shrinkage for all samples, with and without copper, is between 20 and 25%. The results from dilatometry experiments are summarized in Table 5.5 below.

Table 5.5: Maximum shrinkage and temperature required to attain maximum shrinkage.

Sample ID	Maximum Linear Shrinkage (%)	Temperature for maximum shrinkage (°C)
Pure SDC	22.6	1350
0.1 CSDC	20.0	1350
0.5 CSDC	21.5	1180
5.0 CSDC	22.0	1050

Table 5.5 indicates that copper is an effective sintering aid and can reduce sintering temperature substantially. In the extreme case, 5.0 mol% copper can lead to a reduction of 300°C in conventional sintering temperature. A better presentation of shrinkage dynamics can be seen through a plot of shrinkage rate against temperature (Figure 5.8). The shrinkage rate increases with increasing copper content, but the shrinkage set-off temperature remains the same (in the vicinity of 700°C). However, for all samples (with exception of 0.5 CSDC) the peak shrinkage rate is attained close to 800°C. Although the 0.5 CSDC sample reaches a maximum shrinkage rate near 800°, unlike the other samples it retains that shrinkage rate for a wider range of temperature (up to 1000°C). Since the maximum shrinkage rate is achieved in the earlier stage of sintering profile, it is concluded that the majority of shrinkage happens during the initial sintering stage for copper doped SDC. 5.0 CSDC has a shrinkage rate which is almost 2.5 times higher than shrinkage rates for other samples (Figure 5.8). This means that 5.0 CSDC can reach the maximum attainable shrinkage much earlier during sintering. Through Figure 5.8 it can be seen that the majority of the shrinkage in the case of 5.0 CSDC takes place before the isothermal step at 1000°C. It can also be pointed out that during the isothermal step at 1000°C the shrinkage rate rapidly declines. Since the shrinkage rate declines during the isothermal step at 1000°C and then increase again when temperature is increased, it can be concluded that shrinkage is more dependant on temperature as

opposed to time. This means that shrinkage in the case of SDC is more affected by temperature than time, at least at 1000℃.

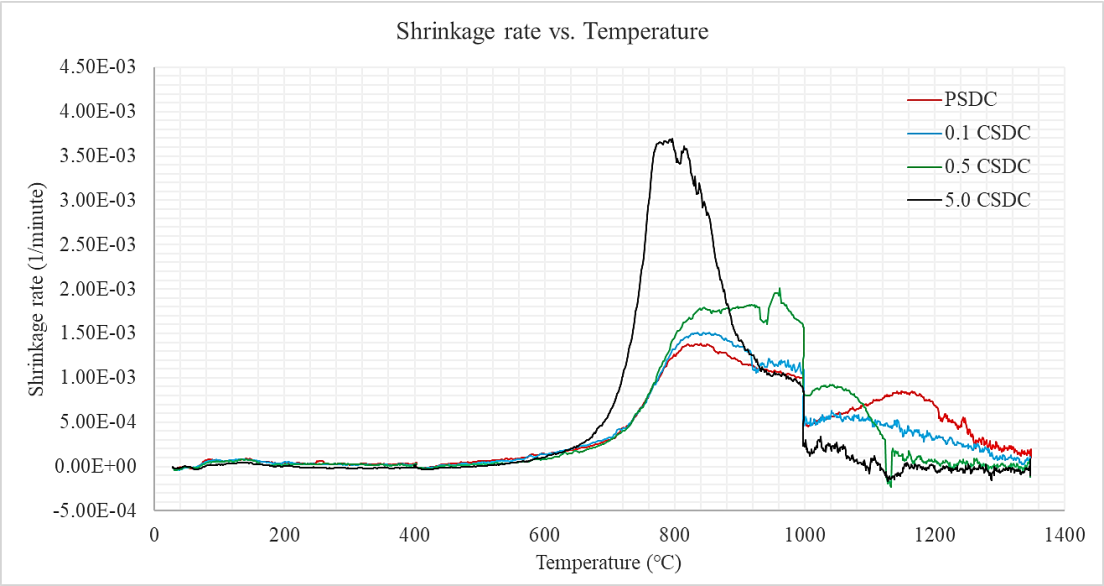

Figure 5.8: Shrinkage rate versus temperature for electrolyte samples.

Another important information which can be extracted from Figure 5.7 is the Coefficient of Thermal Expansion (CTE). Since all the samples reach maximum shrinkage, they experience compression during the cool down period with dimensional changes corresponding to that of a bulk solid of that material. It can also be seen that the shrinkage data during cooling (which starts close to 900 minutes) for all the samples have almost the same gradient, and those data were used to calculate the CTE, which is around 10 ppm.K^{-1} for all samples.

5.3.2 Conductivity Characterization

In the case of doped ceria, oxygen ions travel through oxygen vacancies present in the bulk of material and on the grain boundaries. Once copper is added to SDC it can change both bulk and grain boundary conductivities. When copper segregates as copper oxide on the boundaries (see Figure 5.5 and 5.6) it can add to the resistance at the grain boundaries. When copper goes inside the crystal lattice, because of decrease in lattice constant the association energy of oxygen vacancies may increase leading to a difficulty in oxygen ion conduction. Hence it is critical to

study the effect of copper on the total conductivity, the grain bulk conductivity, and the grain interior conductivity. EIS was used to study/calculate all these parameters.

Figure 5.9 shows the Arrhenius plot of total conductivity.

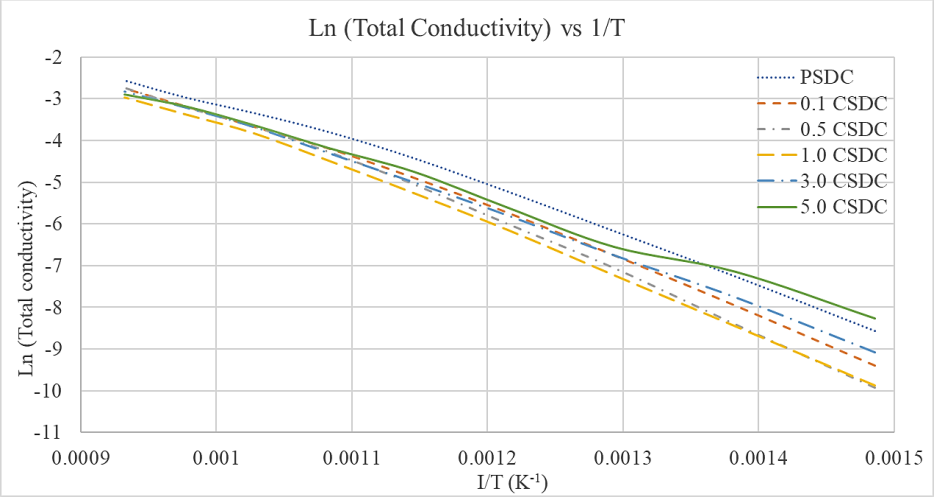

Figure 5.9: Arrhenius plot of total conductivity for different electrolyte samples.

The conductivity of pure SDC remains higher than all the other samples with copper. For instance, at 800℃ the total conductivity of PSDC is 0.077 $S.cm^{-1}$ as opposed to other samples which show a maximum of 0.0642 S/cm at 800℃ (in the case of 0.5 CSDC). It has been reported that SDC made through GNC (similar procedure as used in this work) showed a conductivity of 0.082 $S.cm^{-1}$ at 800℃ [129]. Liu et al. [130] also reported that SDC made using same preparation method shows a conductivity of 0.075 $S.cm^{-1}$ at 800℃. However, other reported values of conductivity vary a lot, as a conductivity of 0.0065 $S.cm^{-1}$ at 800℃ [33] and that of 0.0061 $S.cm^{-1}$ at 800℃ [113] for SDC have also been reported. Similarly, in the case of copper doped GDC, it has been reported that 1 mol% copper doped GDC shows a total conductivity of 0.026 $S.cm^{-1}$ at 600℃[33]. In another report with 1 mol% copper doped GDC the total conductivity is reported as 0.0155 $S.cm^{-1}$ at 600℃ [34]. In our work 1.0 CSDC shows considerably lower total conductivity (0.006 $S.cm^{-1}$ at 600℃). By increasing the amount of copper, the conductivity continues to decrease in which the sample with 5 mol% copper shows a conductivity of 0.055 $S.cm^{-1}$ at 800℃. The exception to this trend is 1.0 CSDC with conductivity lower than all other samples (0.0514 $S.cm^{-1}$ at 800℃).

The effect of copper on grain bulk and grain boundary conductivity was studied by separately plotting grain boundary and grain bulk conductivities. At higher testing temperatures (shown in Table 5.6) the Nyquist plot does not realize two semicircles for grain bulk and grain boundary polarization, and electrode-electrolyte interface. Instead, there was only one semicircle corresponding to electrode-electrolyte interface. This means that the first intercept of that semicircle is the sum of grain boundary and grain interior resistance and hence above a certain temperature the grain boundary and grain interior conductivity can not be calculated separately. Another implication of this is the change in equivalent circuit used for fitting. It was described in Chapter 4 that a parallel combination of resistor and CPE is used to reflect a given conduction mechanism when that conduction mechanism is realized as a semicircle on Nyquist plot. At high temperatures, when the grain boundary arc disappears the parallel combination of grain boundary resistor and CPE is replaced by a resistor only. Figure 5.10 shows Nyquist plot at different temperatures along with the equivalent circuits used (shown as sub figures).

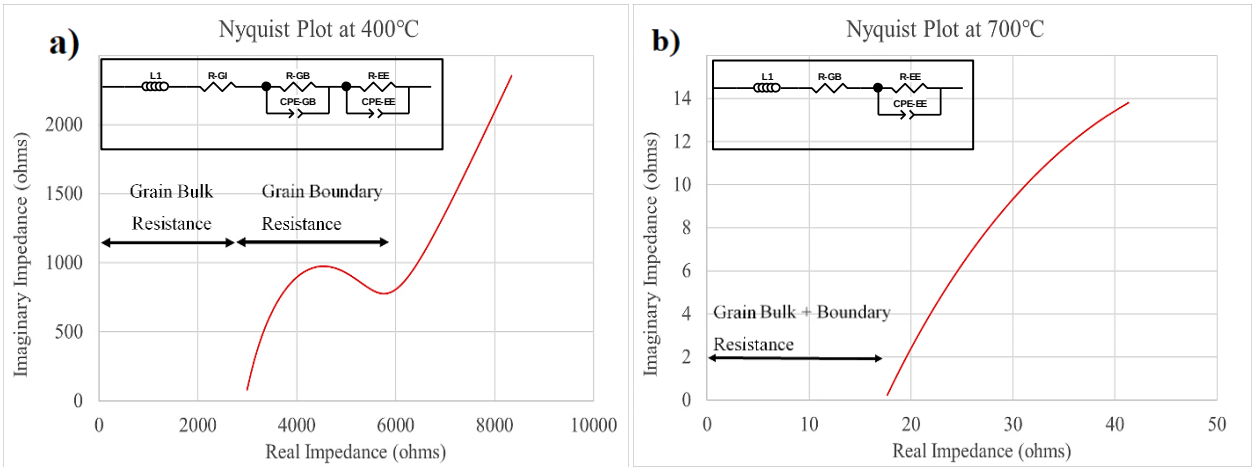

Figure 5.10: Nyquist plot for 0.1 CSDC at a) 400°C and b) 700°C.

Figure 5.10 shows that the first semicircle in Figure 5.10a (for grain boundary resistance) disappears at 700°C (Figure 5.10b). At higher temperature due to reduced impedance and chemical capacitance, even at high frequencies the arcs for grain boundary cannot be captured. Table 5.6 shows the temperature at which the grain boundary arc disappears for each sample.

Table 5.6: Temperature above which grain boundary arc disappears.

Sample ID	Temperature (℃)
PSDC	700
0.1 CSDC	600
0.5 CSDC	600
1.0 CSDC	600
3.0 CSDC	750 except for 500
5.0 CSDC	Does not disappear till 800

The grain boundary arc disappears at 600℃ for samples up till 1 mol% copper addition. For a higher copper percentage, the grain boundary semicircle does not disappear till a higher temperature (750℃ for 3.0 CSDC and 800℃ for 5.0 CSDC). This maybe explained by the formation of a more continuous phase of copper oxide, which has a different time constant than grain boundary conduction of SDC, on the grain boundary as the copper content is increased. Figure 5.11 shows the SEM images of samples at low magnification.

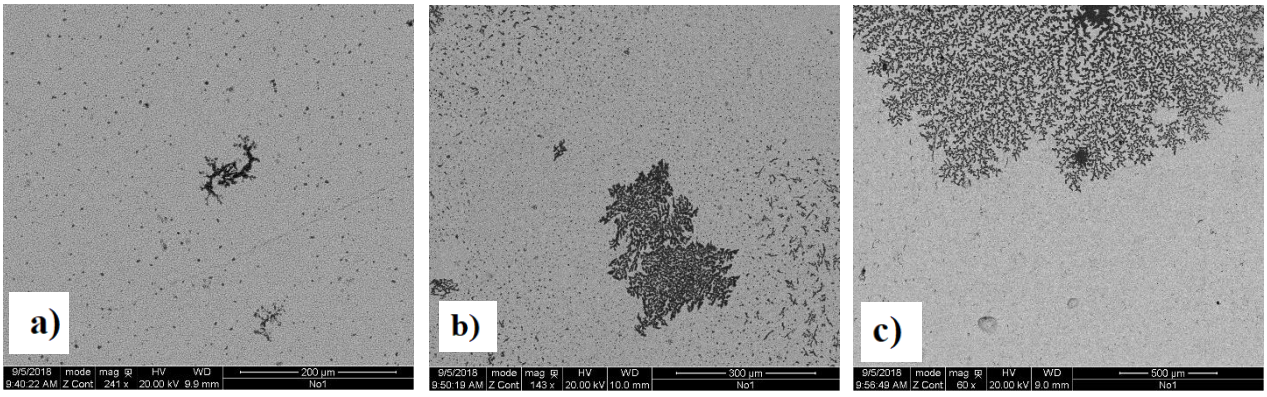

Figure 5.11: SEM image of a) 0.5 CSDC, b) 1.0 CSDC, and c) 3.0 CSDC.

It is evident that copper oxide starts forming a continuous network (dark in color) when the percentage of copper is increased. This implies that the grain boundary semicircle present at higher copper percentage may actually represent a third mechanism of conduction which is conduction through copper oxide. Activation energies for grain interior conduction and grain boundary

conduction, which will be different depending on copper content, can be used to verify this. Using Arrhenius law to describe intrinsic conductivity of a compound, a plot between natural log of conductivity and reciprocal of temperature can be used to calculate activation energies. The Arrhenius law for conductivity is given in the equation below:

$$\sigma = \sigma_0 \exp\left(\frac{-E_a}{kT}\right) \qquad (5.3)$$

In the above equation 'σ' is the conductivity, 'E_a' is the activation energy, 'k' is the Boltzmann constant, and 'T' is the temperature. Figure 5.12 shows Arrhenius plot for grain interior and grain boundary conductivity. For samples between 0.1 and 1.0 mol% copper the grain boundary semicircle disappears before 600°C due to which their grain bulk and grain boundary conductivity were only measured till 550°C. Both grain bulk/interior and grain boundary conductivity for SDC is higher than all other samples. There is a higher difference in grain boundary conductivity between SDC and 3.0CSDC and 5.0CSDC samples as compared to grain bulk conductivity. This also points to the fact that higher copper content leads to more copper oxide deposition on the grain boundary of SDC grains.

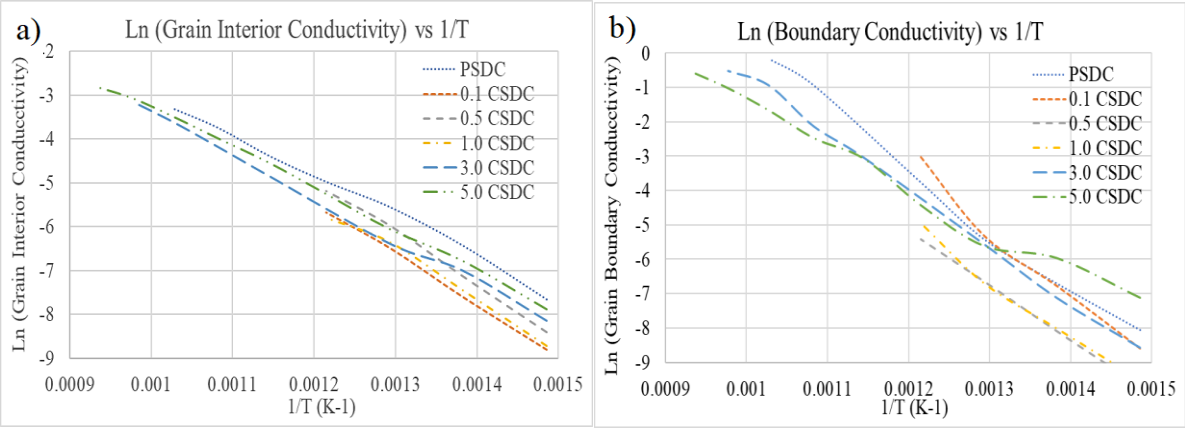

Figure 5.12: Arrhenius plot of conductivity; a) grain bulk conductivity, and b) grain boundary conductivity.

Based on the plots shown in figure 5.12 and 5.9 activation energies for all samples were computed. Figure 5.13 shows the activation energies for total conductivity, grain bulk conductivity, and grain boundary conductivity. In all cases activation energy initally increase with an increase in copper content. For grain bulk conductivity the lowest activation energy is for PSDC and for 5CSDC. The

activation energy for this mechanism first increases and then gradually decreases. The initial increase (at low copper content up to 0.5 mol%) is attributed to increased association energy of oxygen lattice sites due to decrease in crystal lattice constant. Further addition of copper, causing

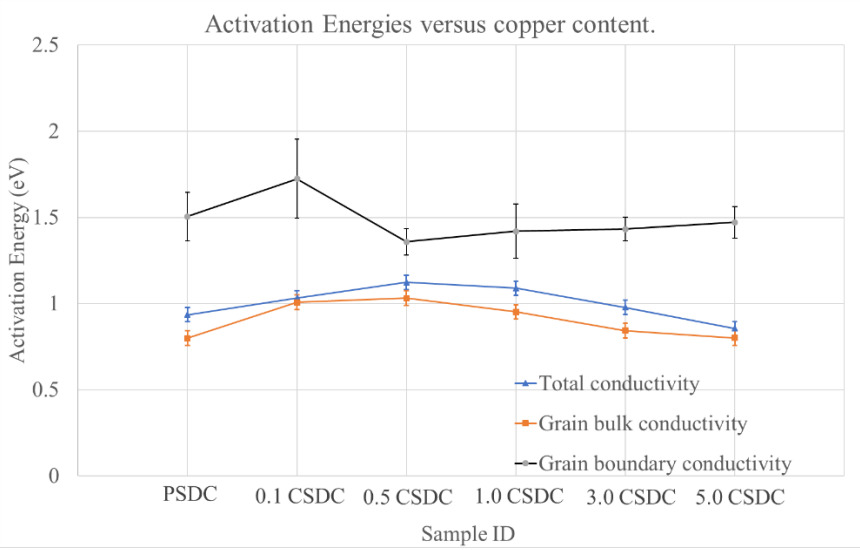

Figure 5.13: Activation energy as a function of copper content of SDC.

a further decrease in lattice constant, may lead to loaclized distortion of the lattice. In this some parts of the crystal structure come under compression because of reduced lattice constant resulting in some expansion (distant from copper sites) to balance the internal stress. Oxygen lattice sites which lie in the exapnded part of the crystal structure will have lower association energy and hence lower activation energy for conduction.

For grain boundary conduction, activation energy increases by adding 0.1 mol% copper. However, it then decreases suddenly at 0.5 mol% copper and then gradually increase again up till 5.0 mol% copper. This in a way verifies that copper starts forming an additional phase on grain boundaries at 0.5 mol% copper and higher. Since the activation energy keeps increasing, it indicates that the amount of copper oxide formed increases with increasing copper content.

Summary

The effect of copper as a sintering aid for SDC was studied. A wider spectrum of copper content, between 0.1 and 5.0 mol%, was used to better understand how copper interacts with SDC. Glycine

Nitrate Combustion (GNC) process was used successfully to incorporate copper with SDC. To assess the effect of copper; physical characterization, which comprises the study of crystal structure, microstructure of sintered samples, and shrinkage behavior of SDC with and without copper, and conductivity characterization was done.

Copper is soluble in ceria crystal structure, i.e. that copper ions replace the positive cations in the ceria crystal structure indicated by the gradual decrease of crystal lattice constant. However, after a certain copper content (0.5 mol% and more), an additional phase, copper oxide, appears on the grain boundaries. Since the crystal lattice constant decreased gradually from 0 to 5.0 mol% copper (indicating the continued dissolution of copper), it appears that there is a thermodynamic balance between the additional copper phase formed and the copper dissolved in the crystal structure of ceria. Using dilatometry analysis, it was seen that copper acts as an effective sintering aid where 5.0 mol% copper doping can lead to a decrease in sintering temperature of up to 300°C. Samples with 5.0 mol% copper attained maximum shrinkage at 1050°C whereas samples without copper attained maximum shrinkage at 1350°C. However, the addition of copper does not change the maximum shrinkage attained by the samples (maximum shrinkage of samples with and without copper is between 20-23%), and in our work no particular trend was observed. Combining the results of SEM and dilatometry it can be concluded that samples with 0.5 mol% or more copper will show similar final shrinkage values. As, through SEM, it was established that 0.5 mol% copper gives a very dense structure and any addition further of copper does not change the microstructure of sintered samples, i.e. the visible surface porosity, grain shape, and grain size are same for samples containing 0.5 mol% and more copper.

Conductivity analysis, which comprised computation of total conductivity, grain interior conductivity, grain boundary conductivity, and activation energies, showed that copper decreases the conductivity of SDC. There was a progressive decrease in total conductivity with progressive increase in copper content where SDC without copper showed a conductivity of 0.077 $S.cm^{-1}$ and SDC with 5.0 mol% copper showed a conductivity of 0.055 $S.cm^{-1}$ at 800°C. It was also observed that copper has a more pronounced effect on grain boundary conductivity compared to grain interior/bulk conductivity. Computed activation energies for grain bulk conductivity showed that increasing copper content to 1.0 mol% copper increases the activation energy of grain interior and further increase in copper decreases activation energy up till 5.0 mol% copper content. Similarly,

for grain boundary conduction, activation energy first increased up till 0.1 mol% copper and then suddenly decreased at 0.5 mol% copper. Further increase in copper increased the activation energies of grain boundary conduction up till 5.0 mol% copper. This is also in line with the SEM analysis of samples with and without copper. The additional copper phase appeared as distributed grains on the grain boundaries of sintered sample at 0.5 mol% copper content. Increasing the copper content gave a more uniform and connected copper phase on the grain boundaries. Since the copper phase starts to become more continuous and larger, its effect on grain boundaries will be higher.

It is concluded that 0.5 mol% copper is a sufficient amount to be used as a sintering aid with SDC. Firstly, it increases the density of SDC to the same extent as when higher copper content was used and secondly a minimum additional copper phase is formed with 0.5 CSDC. Further, the decrease in conductivity in the case of 0.5 mol% is the lowest, sample with 0.5 mol% copper showed a conductivity of 0.0642 $S.cm^{-1}$ at 800°C.

Chapter 6 Fabrication of Metal Supported-Solid Oxide Fuel Cells using Tape Casting and Co-Sintering

6.1 Introduction

This chapter pertains to the study of tape casting and co-sintering used for fabrication of MS-SOFCs. Tape casting consists of casting layers of desired materials using a slurry and a tape caster. Sintering is a thermally activated high temperature process used to form consolidated solid bodies from shaped powders. Co-sintering is when more than one material are stacked and sintered together for bonding. In case of MS-SOFCs, metal support is co-sintered with electrolyte to form a half-cell structure before anode and cathode electro-catalysts can be added to the cell. Specific to SOFCs is the high sintering temperature requirement (up to 1400℃) for maximum densification of common electrolyte materials, such as YSZ and SDC. Mismatch of material properties (especially shrinkage) during this high temperature co-sintering may lead to physical defects (cell cracking, layer delamination, and warping), thus rendering the processing difficult. Presence of metal in cell creates material limitations during co-sintering. For example, metal cannot be sintered in oxidizing atmosphere due to corrosion problem, as even stainless steel goes through oxidation at temperatures above 500℃ in air [131]. Hence, MS-SOFCs co-sintering must be done in reducing or inert atmosphere.

It was initially planned to use SDC as electrolyte because of its higher ionic conductivity at lower operating temperature (600-700°C), but sintering SDC in reducing atmosphere leads cerium ion in ceria to undergo reduction from Ce^{+4} to Ce^{+3}, even at the relatively low sintering temperature of 1100°C when sintering aid is used. This created significant issues, such as cracking, which could not be resolved. Therefore, the more conventional YSZ electrolyte was chosen as the electrolyte in MS-SOFCs studied in this thesis. Another issue in MS-SOFC is that of cathode deposition. The cathode is normally made from metal oxides and perovskites but cannot be treated at high temperatures in reducing atmosphere due to the chances of reduction. Hence using conventional sintering technique for the manufacture of MS-SOFC presents many challenges.

A detailed study of material properties, including shrinkage behavior of cell components and microstructure analysis of co-sintered cells was done to fine tune the fabrication method. This chapter gives results for:

1. Material selection (between SS-430L and SS-410L) for metal support based on the shrinkage compatibility with YSZ.
2. Study of shrinkage dynamics of SS-430L (chosen as metal support) and YSZ (electrolyte) to fine tune the co-sintering profile (includes temperature profile and sintering atmosphere).
3. Cell structure analysis.
4. Application of electrode catalysts. The anode electro-catalyst was infiltrated as solution in the porous metal support whereas the cathode was printed on YSZ surface.
5. Electrochemical performance tests results of fabricated MS-SOFC.

The objective of this study was to fine tune the tape casting and co-sintering methods for fabrication of MS-SOFCs and to add NiO/SDC as anode electro-catalyst and LSCF/GDC as cathode electro-catalyst to the sintered MS-SOFCs.

6.2 Experimental

6.2.1 Selection of materials for metal support

SS-430L and SS-410L commercial powders were mixed with PVB, DOP, PMMA, and ethanol and ball milled for 24 hours. After milling the solution was left to dry at 60℃ for 6 to 8 hours in ambient air. Once the solution was dry the remaining mixture was ground using ceramic pestle and mortar. The ground powder was then pressed at 343 MPa for 2 minutes using a mold into cylindrical disks of 6 mm diameter. These disks were first heat treated in reducing atmosphere (5% H_2/95% Ar) at 800℃ for 30 minutes and then run in a dilatometer (DIL 402 Netzsch, Germany). A sintering temperature of 1400℃ was used because it is similar to conventional sintering temperatures for YSZ and SDC. The temperature profile used had an isothermal step at 400℃ for 60 minutes for removal of organics. The sintering profile used is shown in Figure 6.1. The results of dilatometry were used to make a selection between SS-430L and SS-410L.

6.2.2 Slurry synthesis for tape casting

Slurries for tape casting of cell components were organic based. Essentially, three different components were tape casted; the metal support, transition layers, and the electrolyte. The procedures for making electrolyte and transition layer slurries were similar and based on similar organics compared to metal support slurry. The procedure for slurry synthesis for cell components is described in detail in chapter 4. The tuning of slurries compositions was an iterative process, where the slurry composition was changed based on slurry's viscosity and visual inspection of the quality of the tape casted layers. If the viscosity is too high the slurry will have difficulty spreading, and if it is too low it will overspread. Also, the casted layers should not show particle agglomeration, and should not have cracks upon drying. The final composition of the slurries used in this study are listed in Tables 6.1-6.4. An electronic mass balance was used for weighing, the uncertainty in each measured value was ± 0.001 grams.

Table 6.1: Composition of slurry for metal support.

Component	Mass (%)
Acetonitrile	55.72 ± 0.005
PEO	3.98 ± 0.005
SS-430L	35.82 ± 0.004
PMMA	4.48 ± 0.005

Table 6.2: Preliminary slurry for transition layers and electrolyte.

Component	Mass (%)
Ethanol	17.11 ± 0.006
Toluene	26.88 ± 0.005
Santicizer	36.50 ± 0.008
PVB	19.51 ± 0.007

Table 6.3: Base powder slurry for transition layers.

Component	Mass (%)		
	50/50 transition layer	30/70 transition layer	Porous YSZ layer
Ethanol	9.53 ± 0.009	9.53 ± 0.009	9.53 ± 0.009
Toluene	13.96 ± 0.008	13.96 ± 0.008	13.96 ± 0.008
Hypermer	1.99 ± 0.008	1.99 ± 0.008	1.99 ± 0.008
PMMA	12.42 ± 0.009	12.42 ± 0.009	12.42 ± 0.009
SS-430L	31.05 ± 0.009	18.63 ± 0.007	-
YSZ	31.05 ± 0.009	43.47 ± 0.009	62.10 ± 0.006

Table 6.4: Base powder slurry composition for electrolyte layer.

Component	Mass (%)
Ethanol	10.96 ± 0.01
Toluene	16.06 ± 0.01
Hypermer	1.56 ± 0.009
YSZ	71.42 ± 0.007

These casted layers were used for different purposes:

1. Shrinkage analysis of cell components.
2. Effect of pore former content on final porosity of sintered metal support.
3. Fabrication of button cells:
    a. Half-cells (co-sintered metal support, transition layer, and electrolyte) were used for structural analysis using SEM-EDX.
    b. Electrochemical performance tests.

6.2.3 Shrinkage analysis of cell components

For tuning the sintering profile, dilatometry was run on samples of metal support (SS-430L) and electrolyte (YSZ) made via tape casting. Rectangular pieces (6mm by 8mm) were cut from the casted layers of metal support and electrolyte. These rectangular pieces were stacked together (20 pieces in one sample) and pressed at a pressure of 343 MPa for 2 minutes. The samples were then heat treated in reducing atmosphere (5% H_2/95% Ar) at 800℃ for 30 minutes to remove all the organics and also to provide sufficient strength for further sample handling. These samples were then run in a dilatometer (DIL 402 Netzsch, Germany). Sintering temperature of 1350℃ was used in dilatometry because this falls in the range of conventional sintering temperature of YSZ and SDC (1300-1400℃). The temperature profile had isothermal steps at 400℃ for 30 minutes to burn-out the organics, and at 1000℃ for 10 minutes to ensure that the sample is at uniform temperature before actual shrinkage.

Different sintering atmospheres (reducing and inert) and ramping rates (2.5, 5.0, 7.5℃/min) between 1000 and 1350℃ were used to study the effect of sintering profile on shrinkage dynamics of SS-430L and YSZ.

To assess compatibility of SDC with SS-430L, shrinkage profile of SDC (given in Chapter 5) was used.

6.2.4 Effect of pore former content on final porosity of sintered metal support

To study the effect of pore former content on the porosity of the sintered metal support, circular disks of 20 mm diameter were punched from the metal support casted layer. These disks were stacked together (4 disks per sample) and pressed at 343 MPa for 2 minutes. These disks were then sintered in reducing atmosphere (5% H_2/95% Ar) using the fine-tuned sintering profile (given in results section). Once the metal support disks were sintered, oil impregnation was used to measure the porosity. Samples were weighed after sintering and then after impregnation of oil using vacuum impregnation. The surface of the impregnated sample was wiped with a non-absorbing paper to remove extra oil on the surface before weighing the impregnated sample. The difference in samples' mass before and after impregnation is mass of the impregnated oil. Knowing the densities

of SS-430L and oil, and their respective masses, one can calculate the volume of solid SS-430L and oil, and hence, the porosity. A sample calculation is shown in Appendix A.

6.2.5 Fabrication of MS-SOFC using tape casting and co-sintering.

Half-cell fabrication with YSZ as electrolyte.

For half-cell fabrication 20 mm diameter disks were punched out of casted sheets of metal support, transition layer and electrolyte layer. Different structural designs, based on the number and type of transition layers, were tested. These disks were stacked together according to the respective cell structure and then pressed together at 343 MPa for 2 minutes. For example, for cell structure # 1 - 4 disks of metal support, 1 disk of 50/50 transition, 1 disk of 30/70 transition, one disk of PYSZ, and 1 disk of electrolyte were pressed together (see Figure 6.19). Once the samples were pressed, they were co-sintered according to the fine-tuned sintering profile (given in detail in the results section).

Half-cell fabrication with SDC as electrolyte.

For half-cell fabrication with SS-430L as metal support and SDC as electrolyte, disks (20 mm diameter) were punched out from casted layers of metal support, 50/50 transition layer and 0.5 mol% copper doped SDC. These layers pressed together at a pressure of 343 MPa for 2 minutes and co-sintered at 1100°C for 5 hours in reducing atmosphere.

Once half-cells with YSZ and SDC as electrolyte were made their structural analysis was done. For structural analysis, the co-sintered samples were studied through SEM and EDX.

Electrochemical performance testing

For electrochemical performance testing, the electrode catalysts were added to the co-sintered samples.

For anode, solution infiltration through vacuum was used. A solution of nickel nitrate, samarium nitrate, and cerium nitrate in DI-water was used as the infiltration solution. Co-sintered samples were sealed in a chamber and vacuum was created up to -750 mmHg. The samples were allowed to stay in the vacuum for 5 minutes before filing the chamber with anode solution (see Figure 4.4

in Chapter 4). The vacuum pump was turned off at this point and the chamber was allowed to reach atmospheric pressure and then stay at that pressure for another 5 minutes (a total of 30 minutes). The samples were then taken out of the solution and heat treated at 400℃ for 5 minutes in air. The heat treatment is used to thermally break down the metal nitrate to oxides. The infiltration and heat treatment is marked as one complete anode infiltration cycle. The procedure was repeated to attain an anode mass equivalent to 10% of the initial cell mass (which needed up to 5 cycles). To verify that nitrates are breaking down to oxides, the anode solution was heat treated independently at 400℃ for 5 minutes and the resulting powder was analysed using XRD.

This was followed by application of the cathode. Commercially available cathode ink for LSCF/GDC (Fuel Cell Materials, USA) was used for this purpose. The ink was printed on the electrolyte surface (printing method described in section 4.2 under the heading 'anode catalyst infiltration and cathode deposition') and sintered at 1100℃ for 2 hours in argon. These cells were then fixed to the testing rig and heated up to 700℃ for electrochemical performance testing.

6.3 Results

6.3.1 Selection of material for metal support

YSZ was chosen as the primary electrolyte in this research. This means that the metal support should exhibit shrinkage close to that of YSZ when sintered to conventional sintering temperatures (up to 1400℃). Shrinkage curve from dilatometry for SS-430L and SS-410L in reducing atmosphere are shown in Figure 6.1.

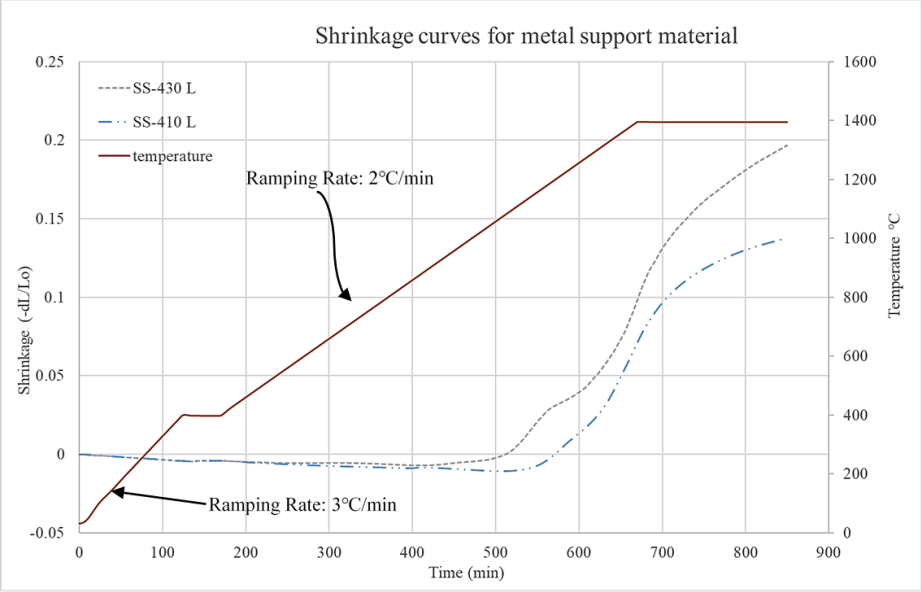

Figure 6.1: Shrinkage curve for SS 430-L and SS 410-L and temperature profile used for dilatometry tests.

The primary y-axis in Figure 6.1 shows shrinkage along positive y-direction and expansion along negative y-direction. SS-430L and 410L both expand initially before the actual shrinkage. In case of SS-430L shrinkage starts around 1000°C compared to almost 1150°C for SS-410L. SS-430L also shows higher shrinkage (almost 20%) which is closer to YSZ shrinkage [52] as opposed to SS-410L (almost 14%). It was, therefore, decided to use SS-430L as the metal support for further work.

6.3.2 Effect of pore former content on final porosity of sintered metal support

The porosity of the sintered metal support is an important parameter as it affects the diffusion of fuel gas to the anode active sites. When tape casting is used, pore formers are used in the slurry to induce porosity. In this study PMMA was used as the pore former. Figure 6.2 shows the effect of pore former content on porosity. The porosity experiment was conducted twice to assure accuracy. It can be seen in Figure 6.2 that the trend is same in both data sets. There is an initial increase in porosity with increasing pore former content, as expected, but followed by a decline once the pore former content is increased from 15 to 20%.

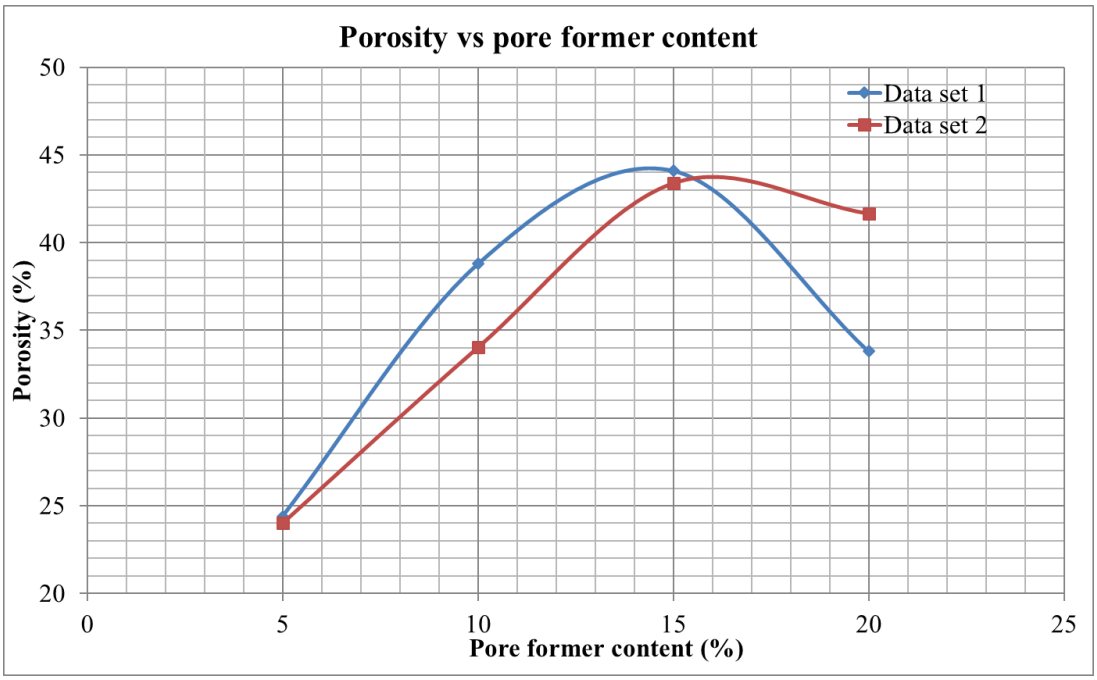

Figure 6.2: Porosity percentage versus pore former content in metal support slurry. Porosity measurements were done twice; first trial is labelled Data Set 1 and second trial is labelled Data Set 2.

The reason for this decline might be that at 20% pore former content the open porosity or open passages through the cross-section are so big that they do not hold the impregnation liquid (oil in this case) as well, affecting the measured mass, and thus calculated porosity. In the past, researchers have commented that up to 40% porosity is adequate for fuel transport in MS-SOFCs[35,55,76,132]. Based on this recommendation, a pore former content of 12.5% was used in this work. According to Figure 6.2, 12.5% pore former content will induce 39-43% porosity in the sintered metal support.

Upon repeating experiment twice with 12.5 wt% pore former the calculated porosity was 39.75 ± 0.25 %.

6.3.3 Shrinkage analysis of cell components

Co-sintering analysis was mostly based on the results of the dilatometry for metal support and electrolyte (YSZ). It is evident in Figure 6.1 that metal starts to shrink only after 1000°C and hence

the difference in temperature profiles used in dilatometry was essentially in the ramping rate from 1000°C to the actual sintering temperature. Three different ramping rates were studied; 2.5, 5.0, and 7.5°C/min. Furthermore, the effect of atmosphere (reducing or inert) on shrinkage of each component was also studied. Results of the dilatometry tests were used to identify:

1. Temperature at which sintering starts.
2. Shrinkage rate with different ramping rates.
3. Maximum shrinkage of each component.
4. Shrinkage of each component when the component reaches the actual sintering temperature during testing.

Figure 6.3 shows the three different sintering temperature profiles used in this study.

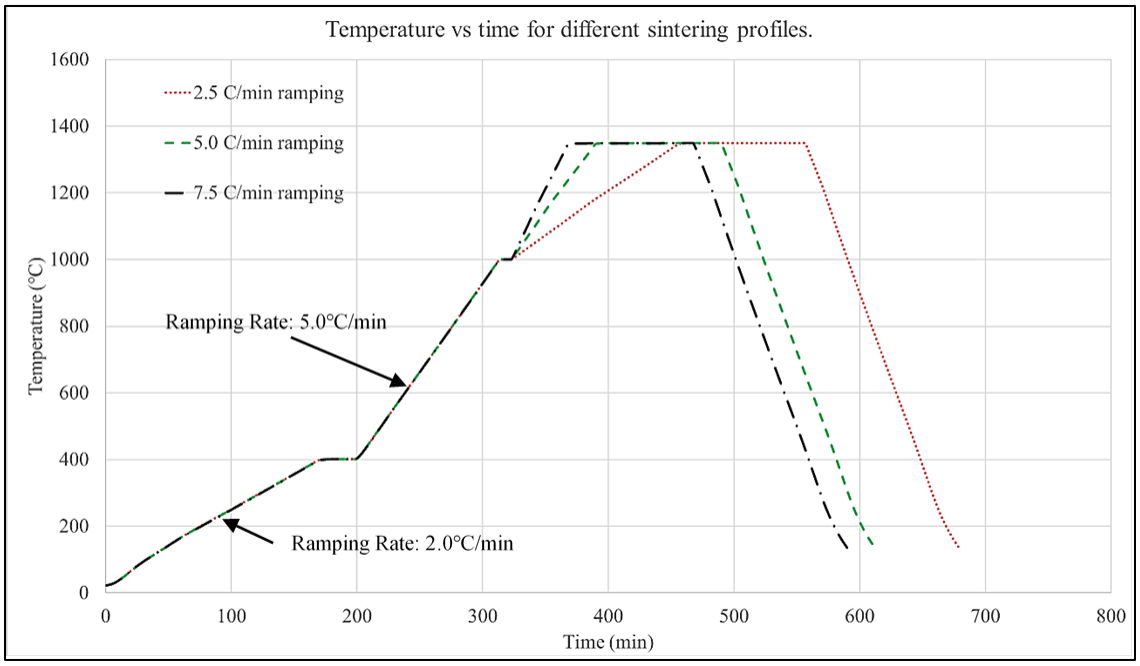

Figure 6.3: Sintering temperature profiles used for dilatometry analysis.

There are three isothermal steps in the temperature profile. The first one is at 400°C for 30 minutes and the second is at 1000°C for 10 minutes. The first one serves the purpose of a burn-out step where all the organics in the pressed cell are burned off. The second one is a temperature stabilization step so that cell attains a uniform temperature, same as that of the furnace, before

heating up for actual sintering. The third one is the actual sintering step, with a sintering temperature of 1350℃. The dwell time at 1350°C was set to 90 minutes.

Dilatometry results in reducing atmosphere

Figure 6.4 shows the shrinkage curves for SS-430L under different sintering profiles. The legend uses entries in the format "ramping rate-atmosphere". For example, a sample which underwent 2.5℃/min ramping between 1000 and 1350°C in reducing atmosphere will be labelled as "2.5 C/min – reducing gas".

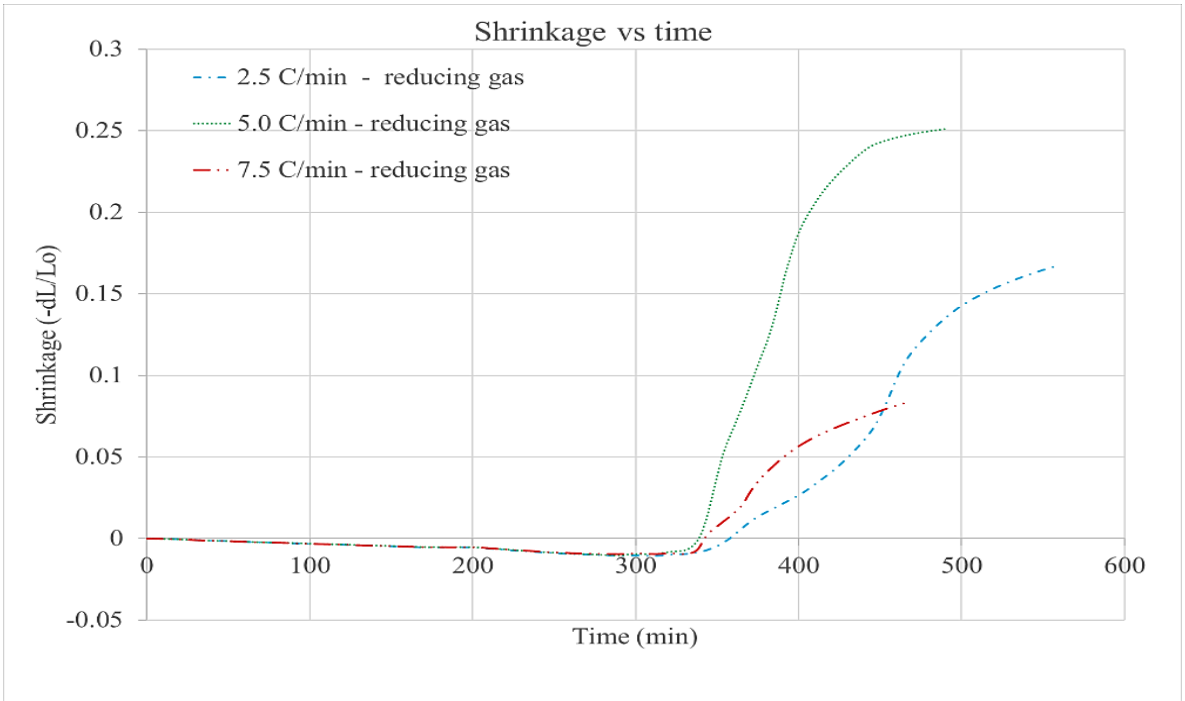

Figure 6.4: Shrinkage profiles for SS-430L under different ramping rates in reducing atmosphere.

The start of sintering is the same for all ramping rates and occurs shortly after 1000℃ or after 320 minutes. The extent of shrinkage, however, is different for the different sintering temperature profiles. The highest shrinkage is shown by samples with a ramping rate of 5.0℃/min, where the shrinkage is slightly more than 25%. In Figure 6.4 sample with 7.5℃/min shows very low shrinkage of up to 8%. This result seems unrealistic and due to unavailability of the dilatometer a re-run was not possible. Later in the shrinkage analysis in inert atmosphere it will be seen that the

shrinkage percentage increases with increasing ramping rate. Hence, for further discussion the sample with 7.5℃/min ramping rate in Figure 6.4 is considered as an outlier.

A better representation of shrinkage dynamics is possible through a plot of shrinkage rate versus temperature. Figure 6.5 shows plots of shrinkage rate versus sintering temperature for two ramping rates (2.5 and 5.0 °C/min).

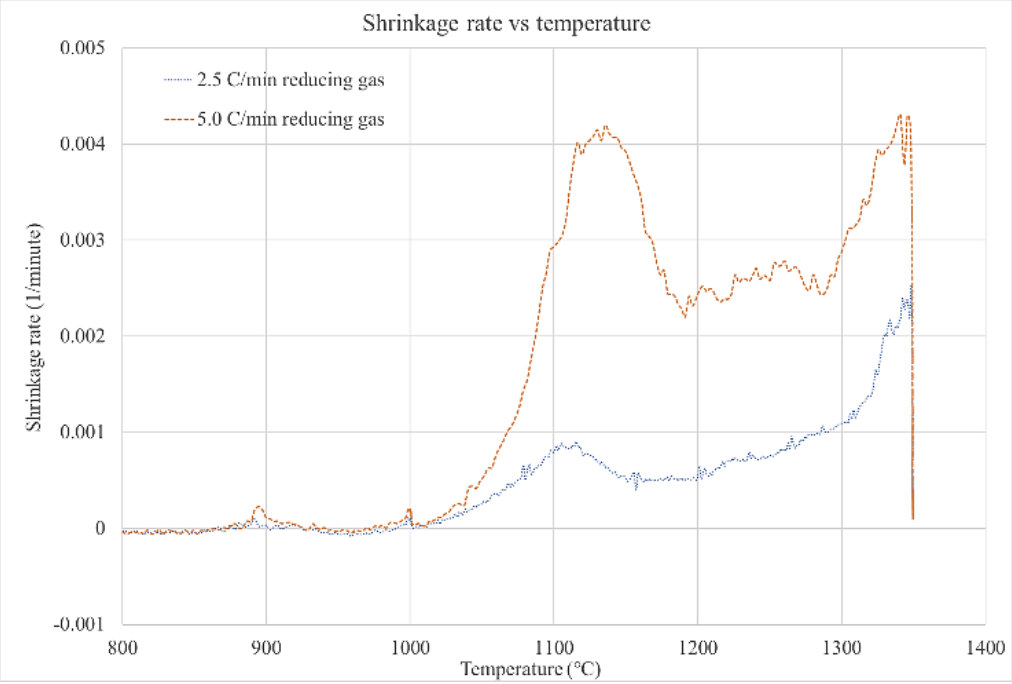

Figure 6.5: Shrinkage rate versus temperature for SS-430L with 2.5, and 5.0℃/min ramping rate in reducing atmosphere (5% H2 / 95% Ar).

The shrinkage rate for 5.0℃/min is considerably higher than that for samples with 2.5℃/min. The peaks formed are similar for both samples, where shrinkage rate increases between 1100 and 1150℃ and then increases again close to the sintering temperature (1350℃). Similar peak positions, regardless of the ramping rate, shows that shrinkage of SS-430L only starts after reaching a certain temperature. This implies that shrinkage for SS-430L is strongly dependant on temperature. Since a higher ramping rate provides a higher driving force per unit time (larger temperature difference per unit time) the shrinkage rate of samples with higher ramping should be higher. For metal support (SS-430L) sintering in reducing gas, shrinkage seems to occur in two phases. The first one between 1100℃ and 1150℃ and the second one close to sintering

temperature. The abrupt decrease in shrinkage rate as soon as the samples reach the sintering temperature also shows that sintering is more temperature dependant that time dependent. Further, it can be assumed that close to 1350℃ the shrinkage will be close to its maximum extent which means that even a small change in shrinkage will need more time as the sample is close to equilibration.

Figure 6.6 shows shrinkage profile of YSZ samples up to 1350°C, at different ramping rates and in reducing environment (5% H_2 / 95% Ar).

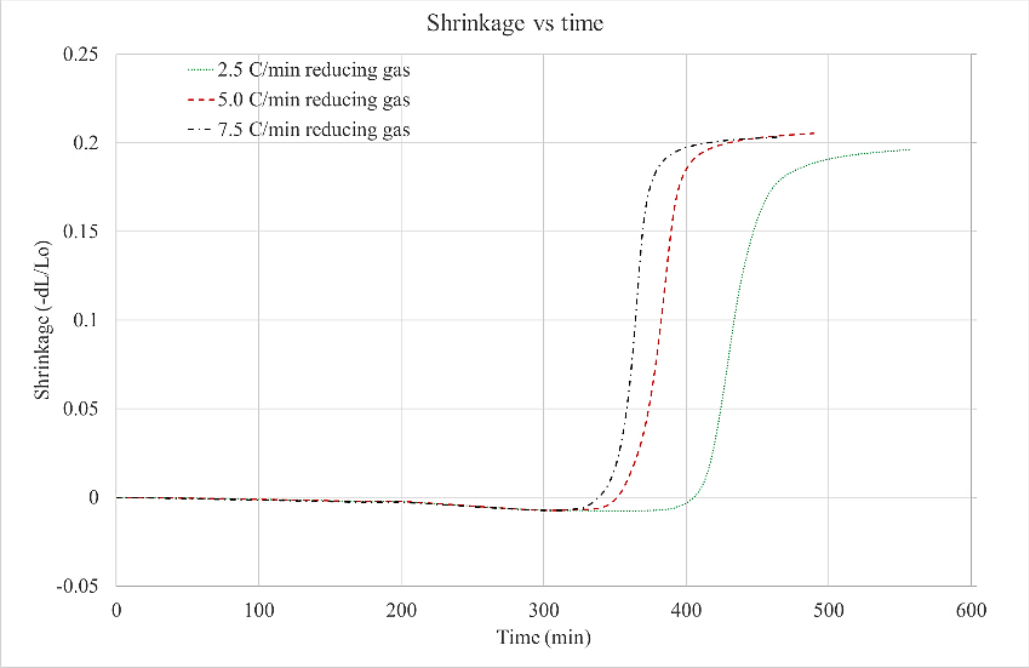

Figure 6.6: Shrinkage profile of YSZ with 2.5, 5.0, and 7.5℃/min ramping between 1000℃ and 1350℃ in reducing atmosphere (5% H2/ 95% Ar).

From Figure 6.6, all sintering profiles have similar S-shape, except that they are shifted toward lower time as the ramping rate increases. Figure 6.7 shows the shrinkage rate profile of YSZ as a function of temperature. It can be seen that shrinkage starts at different temperatures, depending on the ramping rate. For sample with 2.5℃/min ramping rate shrinkage begins slightly after 1150℃, for sample with 5.0℃/min ramping rate shrinkage begins slightly after 1050℃, and for sample with 7.5℃/min ramping rate shrinkage starts slightly before 1050℃. This points to the fact

that higher ramping provides a higher driving force per unit time for shrinkage and hence shrinkage starts earlier.

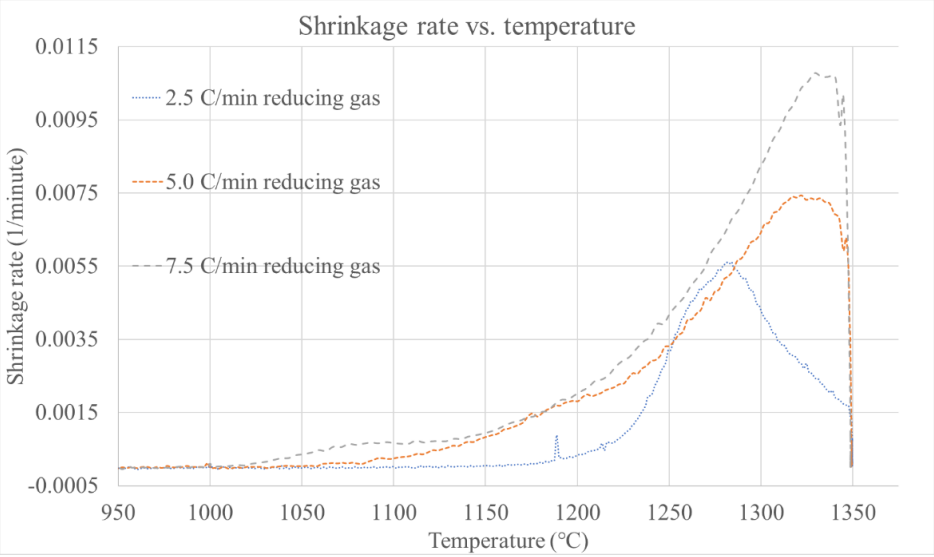

Figure 6.7: Shrinkage rate for YSZ samples versus temperature with different sintering temperature profiles in reducing atmosphere.

Another important feature, evident through Figure 6.7, is the prolonging of sintering for YSZ samples with increasing ramping rate. The shrinkage rate peak for samples with higher ramping rate occurs at a higher temperature. Even though the shrinkage rates for YSZ are higher than shrinkage rates for metal support, they attain maximum shrinkage rates at higher temperatures. This implies that the energy required for YSZ shrinkage is higher than for SS-430L. A sudden decrease in shrinkage rate close to 1350°C, as in the case of metal support, is also exhibited by YSZ samples with 5.0°C/min, and 7.5°C/min ramping rate. Sample with 2.5°C/min ramping, however, forms a peak close to 1280°C and the rate starts falling well before reaching the sintering temperature. This means that the YSZ samples with 2.5°C/min ramping rate are close to their maximum shrinkage upon reaching sintering temperature.

Useful information regarding the dynamics of sintering and retrieved from Figures 6.4-6.7 is summarized in Table 6.5.

Table 6.5: Summary of important parameters from Figure 6.4-6.7 (reducing sintering atmosphere).

	2.5℃/min ramping rate		5.0℃/min ramping rate		7.5℃/min ramping rate	
Parameter	Metal Support	YSZ	Metal Support	YSZ	Metal Support	YSZ
Sintering start temperature (℃)	1020	1175	1020	1050	1020(N/A)	1023
Maximum shrinkage (%)	16.5	19.6	25.1	20.5	8.8 (N/A)	20.4
Shrinkage (%) upon reaching 1350℃.	8.8	17.1	17.1	18.1	3.2 (N/A)	17.3
Maximum sintering rate (1/minute)	0.0022	0.0056	0.0043	0.0073	0.0018(N/A)	0.0107
Temperature at max sintering rate (℃)	1345	1280	1347	1325	1343	1340

As mentioned previously, metal support shrinkage (in reducing atmosphere) starts around similar temperature values irrespective of the ramping rate. However, for YSZ the shrinkage start temperature decreases with increasing ramping rate. If the thin YSZ electrolyte layer densifies too early, it will become brittle and may crack as the metal supports continues to shrink. Thus, ideally, the metal support should reach its maximum shrinkage prior to YSZ. Hence, during co-sintering of porous metal support and YSZ electrolyte layer it is critical to prolong the shrinkage of YSZ as much as possible. Figure 6.8 shows a graphic representation of this concept, in the diagrams metal support is at the bottom (thicker layer) and YSZ is at the top (thinner layer). In Figure 6.8 cell geometry after dwell on sintering temperature is what the samples looked like after cooldown.

However, cell geometry at the start of sintering temperature was speculated based on numbers from Table 6.5 and shape of the cells after sintering.

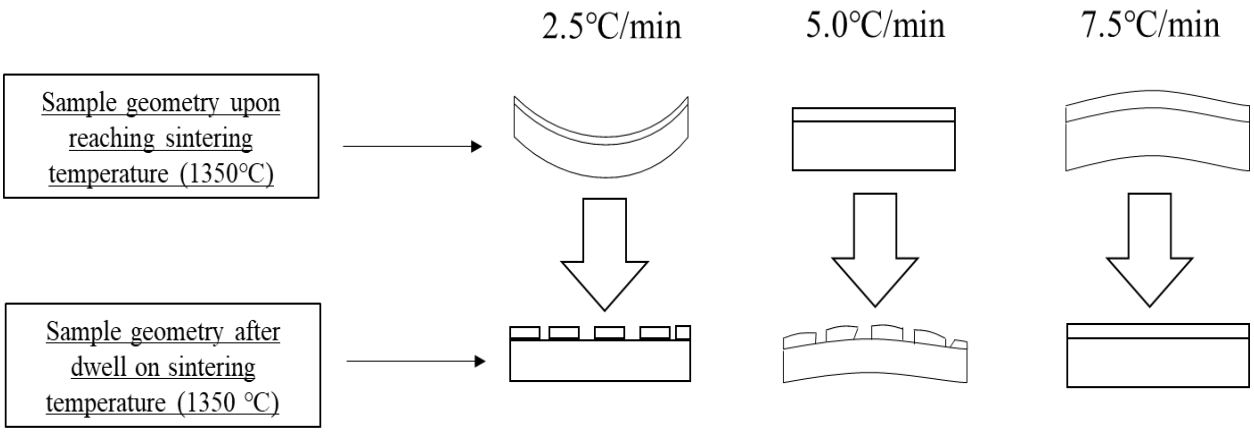

Figure 6.8: Schematic showing sample geometry upon reaching sintering temperature and after dwell on sintering temperature for samples with 2.5, 5.0, and 7.5°C/min ramping rate.

The shrinkage value of the samples just prior to reaching 1350°C plateau helps fine-tuning the co-sintering temperature profile. Cracking, delamination and warping of cells are dependant on how the components behave during the isothermal sintering step (1350°C for 2 hours here). Ideally YSZ layer should be soft and continue to shrink during this step. That means that upon reaching sintering temperature YSZ should not be in its final stage of shrinkage. Metal support, on the other hand, should be close to its maximum shrinkage. From Figure 6.8 (using information from Table 6.5) three scenarios can be considered.

Shrinkage profile with 2.5°C/min ramping rate.

In this case, upon reaching sintering temperature, the cell will be warped towards the electrolyte side (see Figure 6.8a). The metal support still has to shrink 7.7% to reach its final shrinkage compared to 2.5% for YSZ. The electrolyte will be somewhat brittle at this point and when the metal support continues to shrink the electrolyte might break or delaminate.

Shrinkage rate with 5.0°C/min ramping rate.

In this case, when the sample will reach sintering temperature both the metal support and electrolyte will have shrunk to almost the same value, 17.1% for metal support and 18.1% for YSZ.

The metal support still has to shrink 8% to get to its final shrinkage and YSZ have to shrink only 2.4%. Even in this case YSZ will be somewhat brittle and might crack when the metal support continues to shrink.

Shrinkage profile with 7.5℃/min ramping rate

In this case, when YSZ reaches sintering temperature it still has to shrink 3.1% (this is higher than that for samples with 2.5 and 5.0℃/min ramping). At the same time, although reliable dilatometry data for metal support in this condition is not available, it is anticipated from the trend at 2.5 and 5.0 ℃/min that metal support likely shows a higher shrinkage (more than 17.1%) upon reaching sintering temperature. Therefore, even if metal support still has to shrink (but less than that for 2.5 and 5.0℃/min ramping), the YSZ layer will be relatively softer and hence may not crack or delaminate when metal support continues to shrink while at the shrinkage temperature.

Keeping in mind the above reasoning, the best possible ramping rate seems to be 7.5℃/min between 1000 and 1350℃ for co-sintering in reducing atmosphere. Hence for co-sintering in reducing atmosphere this was chosen as the ramping rate.

The primary purpose for the use of reducing atmosphere is the protection of metal support. This may also be achieved by using inert atmosphere for sintering as long as shrinkage dynamics are similar. For this reason, similar dilatometry analysis was done in inert atmosphere (100% argon).

Dilatometry results in inert atmosphere

Figures 6.9 and 6.10 show shrinkage profiles of metal support in Argon. From Figure 6.9, it can be seen that the shrinkage of metal support samples, regardless of ramping rate, is higher than 26%, and there is no progressive increase in the shrinkage with increasing ramping rate. This is different than for metal support sintered in reducing atmosphere. Firstly, the maximum shrinkage of samples sintered in reducing atmosphere increases with increasing ramping rate (Figure 6.4). Secondly the final shrinkage of samples sintered in reducing atmosphere for all ramping rates is lower than for samples sintered in argon; final shrinkages for samples sintered in reducing atmosphere are between 16.5 and 25.1% whereas samples sintered in argon are all around 26%.

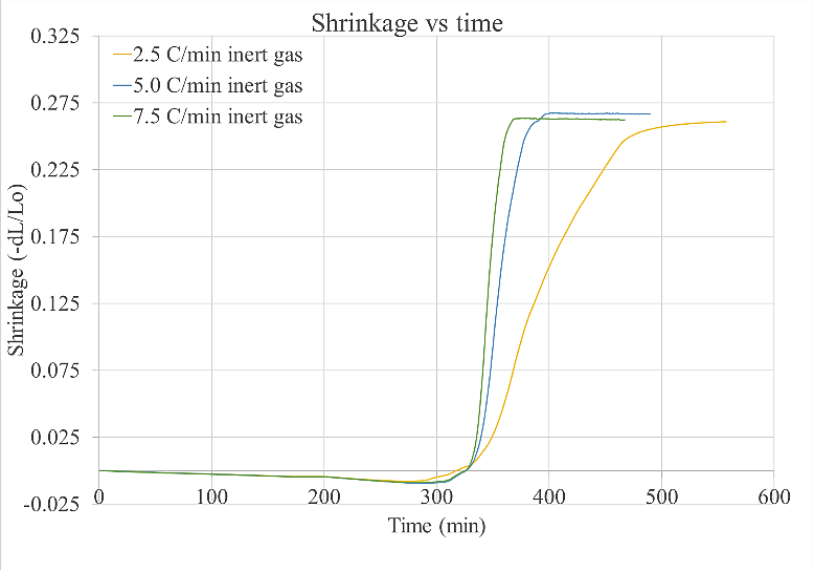

Figure 6.9: Shrinkage profile of metal support samples sintered at 1350℃ in inert gas atmosphere (Ar) and at different ramping rates.

Figure 6.10 shows shrinkage rate of metal support samples sintered in argon with temperature. Unlike samples sintered in reducing atmosphere, metal support sintered in inert atmosphere shows only a single peak for shrinkage rate for different ramping rates (Figure 6.10).

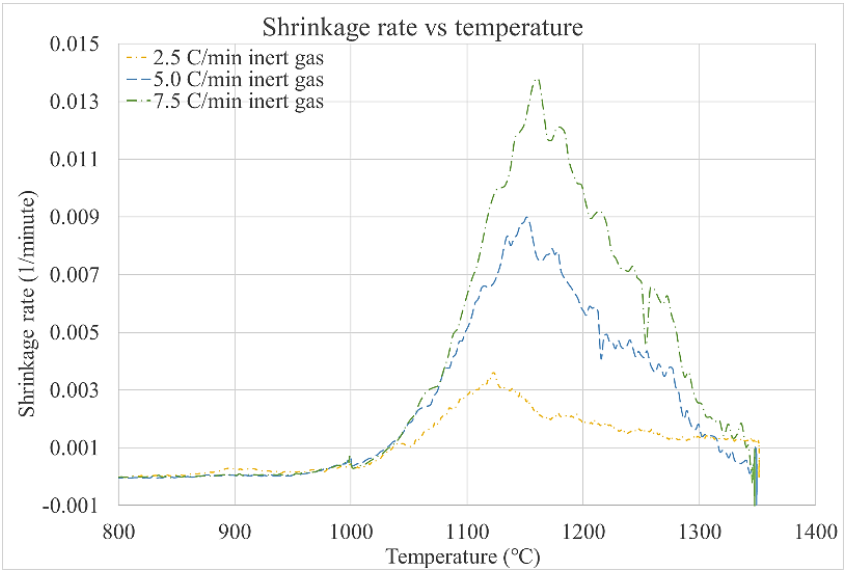

Figure 6.10: Shrinkage rate versus temperature for SS-430L samples sintered at 1350℃ in inert gas atmosphere.

The shrinkage rate increases and the shrinkage rate peak position shifts to a slightly higher temperature with increasing ramping rate. For instance, the shrinkage rate for metal support sintered in reducing atmosphere with a 5.0°C/min ramping is 0.0041 min^{-1} compared to 0.009 min^{-1} for samples sintered in inert.

The higher shrinkage rate might be the reason why samples sintered in inert gas atmosphere only show a single peak. When samples reach close to the actual sintering temperature (1350°C) they are already close to their maximum shrinkage (due to higher shrinkage rates at lower temperature). This means that upon reaching sintering temperature shrinkage will be lesser and slower and hence the shrinkage rate will be low as well. High shrinkage rates in case of sintering in argon might be due to the formation of chromia or silica on the metal support. This is discussed in more detail later.

Figures 6.11 and 6.12 show the shrinkage profile and shrinkage rate for YSZ samples sintered in inert gas atmosphere with different ramping rates.

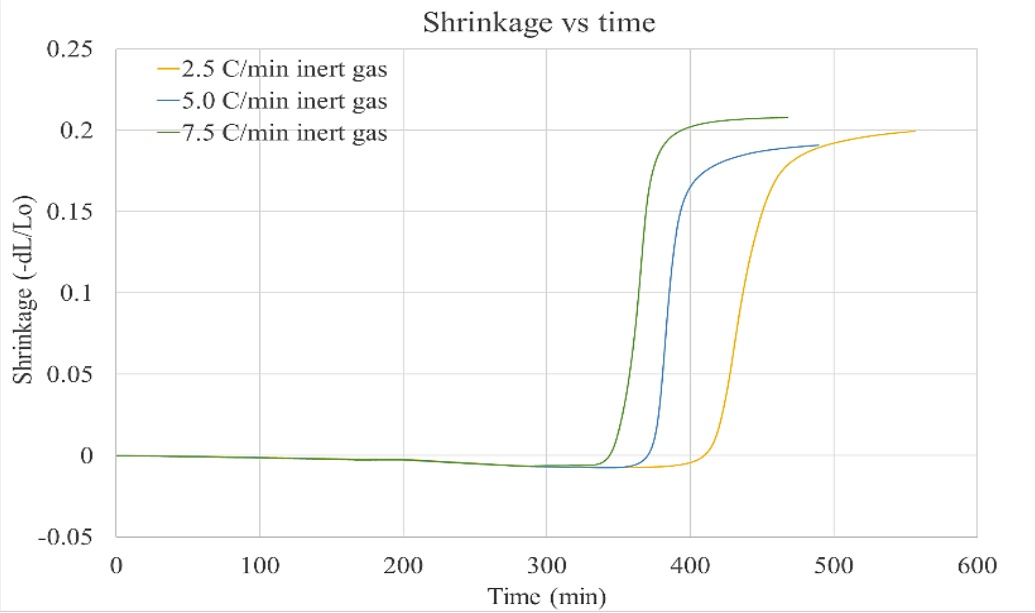

Figure 6.11: Shrinkage profile for YSZ samples sintered at 1350°C at different ramping rates in inert gas atmosphere.

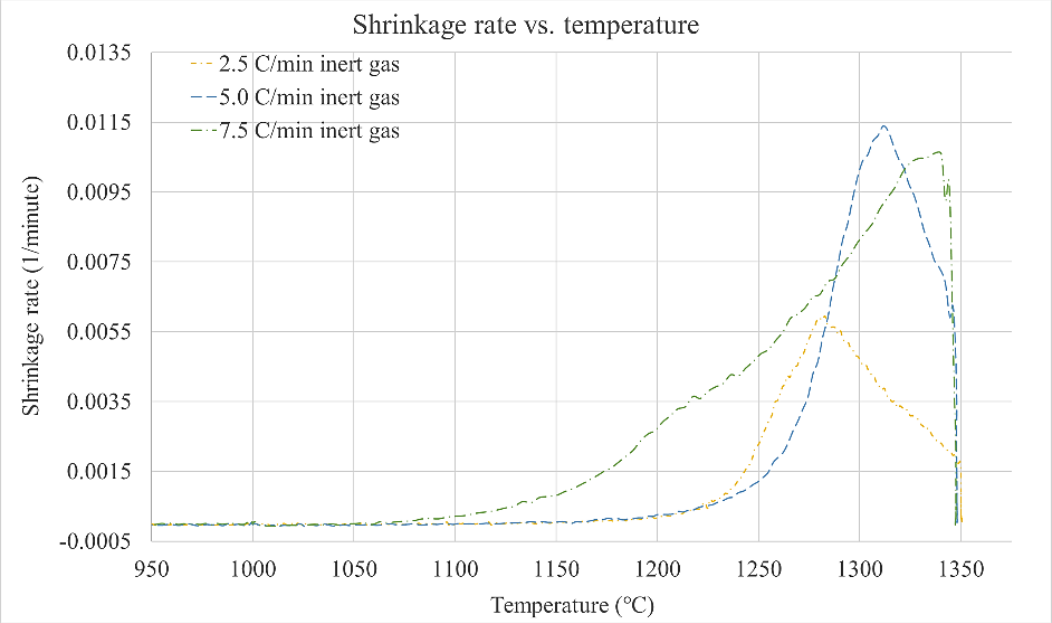

Figure 6.12: Shrinkage rate vs. temperature for YSZ samples sintered at 1350℃ in inert atmosphere with different ramping rates.

YSZ samples sintered in inert gas atmosphere show very similar dynamics to when the samples were sintered in reducing atmosphere. Even the maximum shrinkage rates are comparable for samples with 2.5℃/min and 7.5℃/min. For example, shrinkage rate for samples sintered with 2.5℃/min in reducing and in inert atmosphere are both close to 0.0055 min^{-1}. Table 6.6 summarizes important information that can be extracted from Figures 6.9-6.12.

Table 6.6: Summary of key parameters from Figures 6.9-6.12.

	2.5℃/min ramping rate		5.0℃/min ramping rate		7.5℃/min ramping rate	
Parameter	Metal Support	YSZ	Metal Support	YSZ	Metal Support	YSZ
Sintering start temperature (℃)	1010	1200	1010	1200	1010	1100
Maximum shrinkage (%)	26.1	20	26.7	20.6	26.2	19.8

Shrinkage (%) upon reaching 1350℃.	23.5	16.5	26.2	13.8	26.3	17.4
Maximum sintering rate (1/minute)	0.0036	0.0058	0.009	0.0114	0.0138	0.0106
Temperature at max sintering rate (℃)	1124	1282	1151	1311	1162	1340

The metal support shrinkage upon reaching the sintering temperature is always substantially higher than the shrinkage of YSZ at all ramping rates in inert atmosphere. The difference in shrinkage values of metal support and shrinkage of YSZ samples with 7.5℃/min ramping is 9% upon reaching the sintering temperature. This might not be ideal since metal support and YSZ both start off with same dimensions and such a huge difference in shrinkage upon reaching the sintering temperature will lead to physical defects. The reason for very high metal support shrinkage in inert gas compared to reducing gas is attributed to the presence of chromia (chromium oxide) or silica (silicon oxide) in the case of inert gas sintering. In inert atmosphere, in the absence of hydrogen, even trace amount of oxygen can lead to silica formation. Similarly, samples sintered for microstructure analysis were placed on a porous alumina support in the furnace which can lead to presence of alumina grains on the surface of sintered metal support. Figure 6.13 shows SEM images for metal support sintered in reducing and inert atmosphere. In both cases the ramping rate between 1000 and 1350℃ was set to 7.5℃/min.

It can be seen that the samples sintered in reducing atmosphere (Figure 6.13a) have more porous structure than that of samples sintered in inert atmosphere (Figure 6.13b). Higher magnification SEM images of samples shows that there is an additional phase present in samples sintered in inert atmosphere (Figure 6.13d, additional phase circled in red). EDX was used to identify the additional phase, and the results are shown in Figure 6.14. The extra phase in this picture is identified as silicon oxide and aluminium oxide due to the prominent peaks of silicon, aluminium, and oxygen in the EDX spectra (Figure 6.14b).

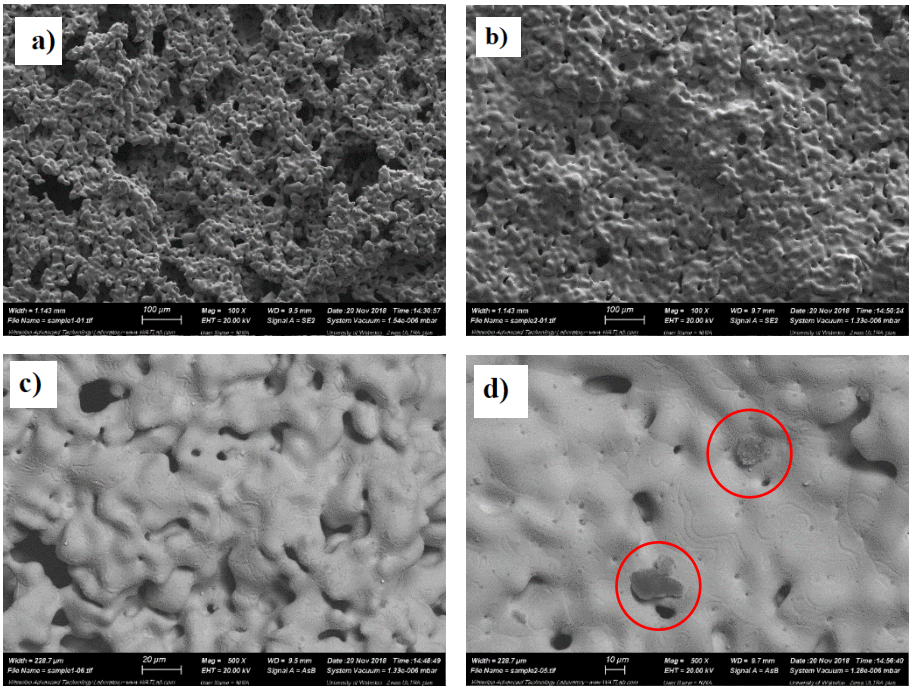

Figure 6.13: SEM images of metal support sintered in reducing atmosphere (a and c), and in inert atmosphere (b and d).

Upon further inspection it was found that the entire surface of the samples sintered in inert atmosphere have small particles of this phase. Hence, in the case of inert gas, silica and alumina present might act as a sintering aid and enhance the sintering of metal supports so that it shrinks faster (higher shrinkage rates) and to a larger extent (higher maximum shrinkage).

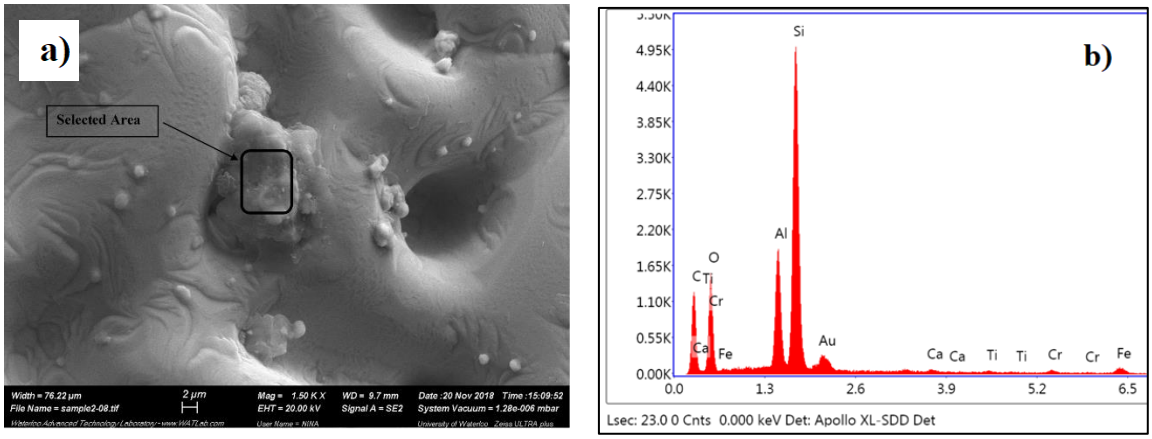

Figure 6.14: a) SEM image of metal support sintered in inert atmosphere; b) EDX spectra of selected area in SEM image in ‘a’.

From the above discussion there are two major reasons why inert atmosphere might not be a good choice for co-sintering:

1. Metal support shrinks to a high very high extent before reaching the sintering temperature. This implies that the metal support is already in its final stage of sintering and that the cell is warped towards the metal side. During the isothermal sintering step, YSZ continues to shrink whereas the metal support shows minimum shrinkage, which can lead to YSZ layer cracking or delamination.
2. Silicon is present in SS-430L (0.5 wt%) and during sintering in inert atmosphere it forms silica. In the same way, during sintering the metal support was placed on an alumina support, and traces of alumina were also present on the surface of metal support. Both silica and alumina grains protrude from the surface of the metal support. Even though non-conductive silica and alumina do not form continuous phases, their presence may lower the conductivity of the metal support [21].

This analysis does not take into account the effect of interaction of metal support with YSZ when they are co-sintered. Co-sintering in reducing atmosphere will be presented in the next section with a ramping rate of 7.5°C/min between 1000 and 1350°C. Figure 6.15 shows the sintering temperature profile used in the rest of this work.

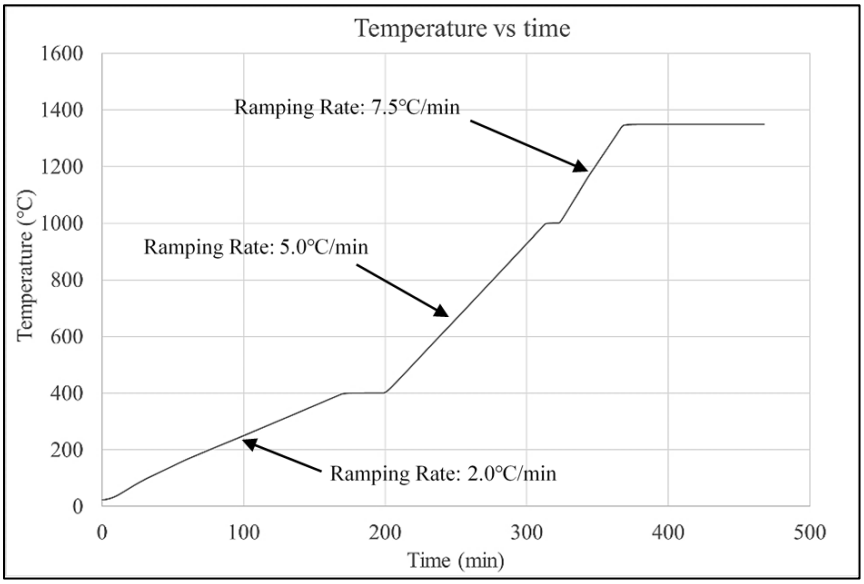

Figure 6.15: Refined sintering temperature profile for co-sintering of metal supported half-cells.

6.3.4 Fabrication of MS-SOFCs with copper co-doped SDC

Shrinkage profile of 0.5 mol% copper co-doped SDC (Figure 5.7 and 5.8 in Chapter 5) was used to assess the compatibility of SDC shrinkage with SS-430L. Figure 5.7 shows that the shrinkage set-off temperature for 0.5CSDC is close 700°C, which is considerably lower than that of SS-430L (around 1100°C). Further, the shrinkage rate peak (where the shrinkage is highest) for 0.5CSDC occurs before 1000°C and then the shrinkage rate drops. This means that 0.5CSDC will have attained close to maximum shrinkage even before SS-430L starts to shrink. Such mismatch in shrinkage behavior leads to physical defects, like cracking of the electrolyte layer. Nonetheless, 0.5CSDC was sintered on a pre-fabricated porous MS at 1100°C in reducing atmosphere, and PSDC was co-sintered with MS at 1350°C in inert atmosphere. The resulting microstructure of the electrolyte layers are shown in Figure 6.16.

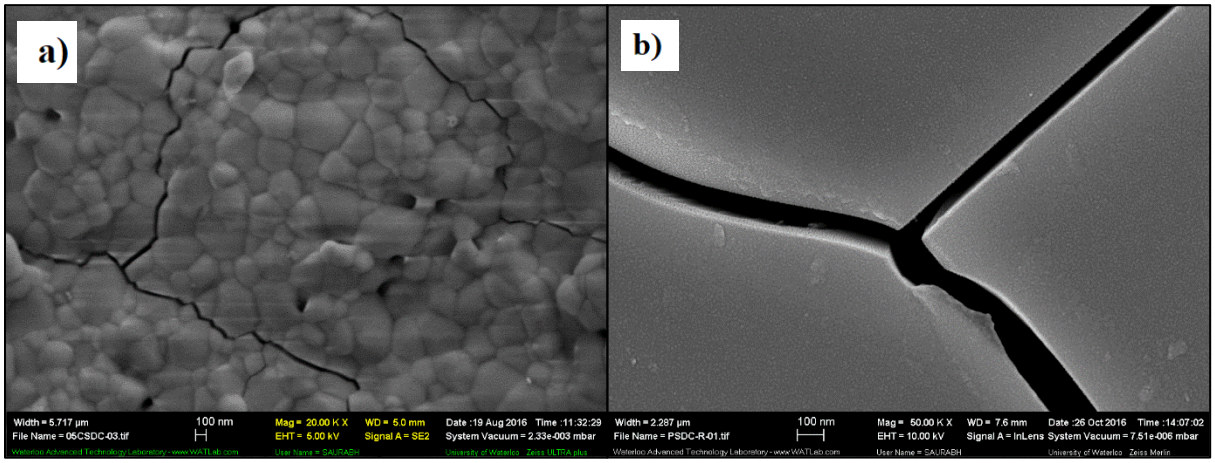

Figure 6.16: SEM image of a) 0.5CSDC surface of a SS-430L|0.5CSDC half-cell sintered at 1100°C in reducing atmosphere and b) SEM image of PSDC surface of a SS-430L|PSDC half-call sintered at 1350°C in inert atmosphere.

In both cases it can be seen that the electrolyte surface is cracked. Unfortunately, MS-SOFCs with copper doped SDC and plain SDC were not successfully fabricated in this research.

6.3.5 Fabrication of MS-SOFC with YSZ electrolyte using tape casting and co-sintering

Fabrication and characterization of MS-SOFCs was done in three sequential parts. The first was co-sintering of MS-SOFC half-cells where the sintering profile tuned (from previous section) was

used to co-sinter stacked metal support and electrolyte. Once half-cells with little to no physical defects were co-sintered, the next step was the structural analysis of the cell. In this, the cell structure was optimized to get a simple structure with minimum material usage. The last step was the addition of electrode electro-catalyst and electrochemical performance testing.

Co-sintering of hall cells (Metal support and electrolyte)

All metal supported cells were co-sintered using sintering profile presented in Figure 6.15, in reducing atmosphere. Figure 6.17 shows optical images of two sample sintered in reducing atmosphere in the same sintering profile. The difference between sample in Figure 6.17a and b is that an oxygen scavenger used during sintering for sample in Figure 6.17b. The reason to use scavenger is to remove trace amount of oxygen present in the furnace.

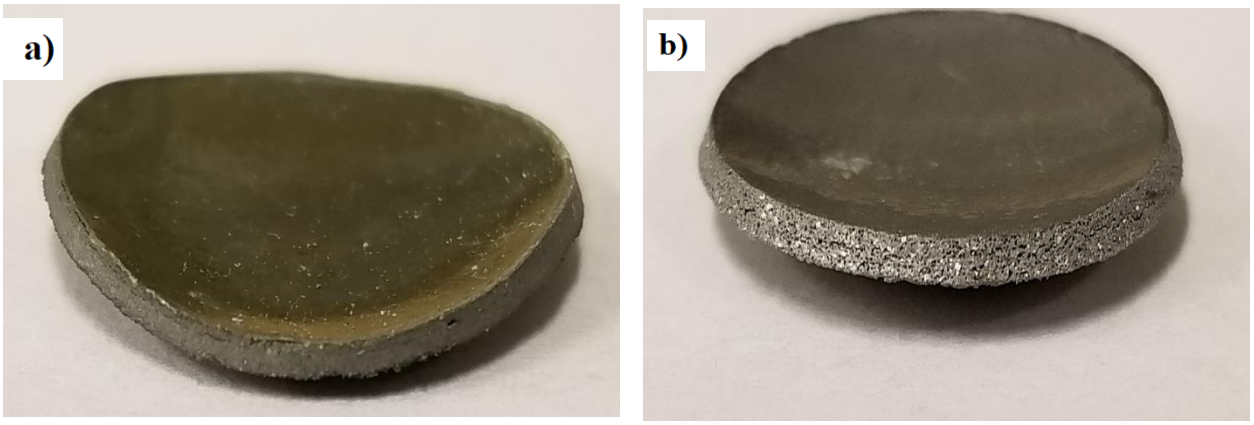

Figure 6.17: Optical image of a Metal Supported half-cell sintered in reducing atmosphere at 1350℃; a) Samples sintered without a scavenger, and b) samples sintered with a scavenger.

In Figure 6.17, the bottom part of both samples is metal support and the thin layer on top is YSZ. There is a difference in color between the samples. The sample sintered without scavenger (Figure 6.17a) shows a greenish color which is attributed to formation of chromia (indicates presence of oxygen in the furnace). Upon careful inspection, delamination is also seen close to the YSZ layer in the sample in Figure 6.17a. Use of scavenger (loose SS-430L powder in this case) can reduce the amount of chromia formed as seen by the absence of green color in sample in Figure 6.17b. Other than having a greyish color, the porosity of metal support is also more visible in the sample sintered with scavenger (Figure 6.16b).

In Figure 6.17 both samples seem to warp towards the YSZ (electrolyte) side. To resolve the issue of warping a counter weight (0.5 $g.cm^{-2}$) was used. The counter weight was placed on the cell during co-sintering to constraint the sintering of cell so that it does not warp. Figure 6.18 shows an optical image of a half-cell co-sintered with a counter weight.

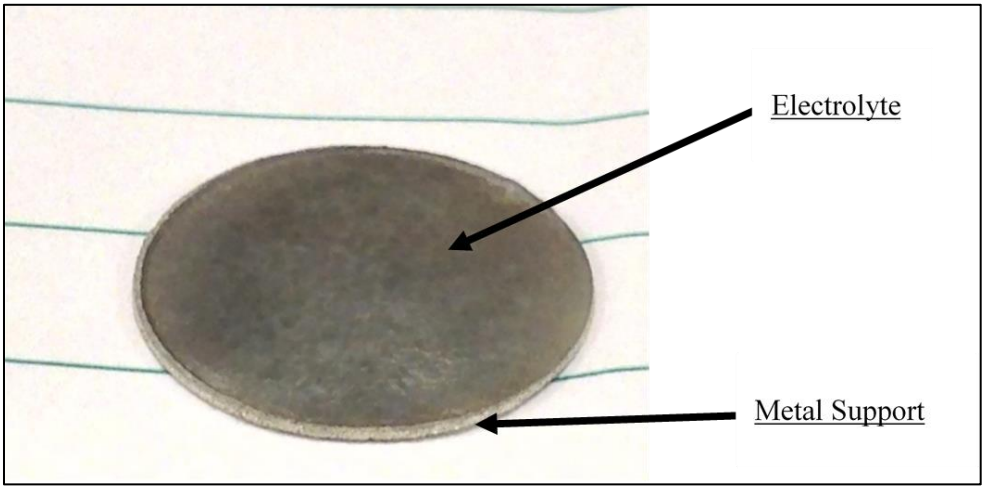

Figure 6.18: Optical image of co-sintered half-cell with a counter weight during sintering.

The final sintering profile was set as that shown in Figure 6.15 in reducing atmosphere. The next step is the structural analysis of different cell structures (shown in Figure 6.19).

Structural analysis of Metal-Supported half-cells.

Figure 6.18 shows the different half-cell structures studied. The difference is only in the type and number of transition layers used.

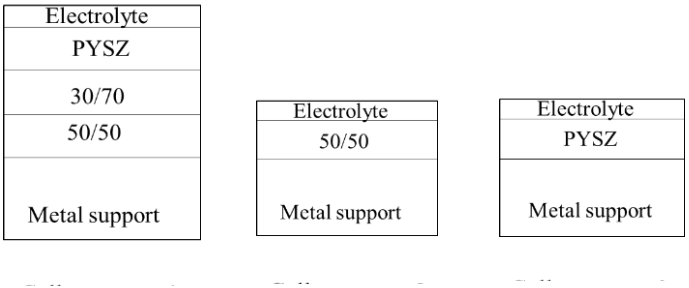

Figure 6.19: Cell structures tested in this study.

In Figure 6.19, ‘50/50’, ‘30/70’, and ‘PYSZ’ are all transition layers in which ‘50/50’ means 50% YSZ and 50% stainless-steel by mass, ‘30/70’ mean 30% YSZ and 70% stainless-steel by mass, and ‘PYSZ’ means porous YSZ layer. Also, the transition layers had 20% by mass pore former. Only the above three structures were chosen as they represent the complete spectrum of structures. Structure 1 being the most complex provides a very gradual and smooth transition by using two cermet layers and then a porous YSZ layer. Structure 2 on the other hand just employ one cermet layer (for transition) and structure 3 only used porous YSZ (for increasing TPB). In all cases, 4 disks of metal support and a single disk of other component layers were used. Transition layers are used in the cell structure to provide a smooth transition from metal support to YSZ. The transition layers also act as a bonding layer, where the metal particles in the metal support tend to bond to the metal particles in the transition layer, and where the YSZ particles in the electrolyte tend to bond to YSZ particles in the transition layer. Once the cells were co-sintered with different cell structures SEM was used to assess the structure on a micro level. The goal was to use the simplest structure which does not lead to any physical defects. Figure 6.20 shows a cross-sectional image of cell with structure 1.

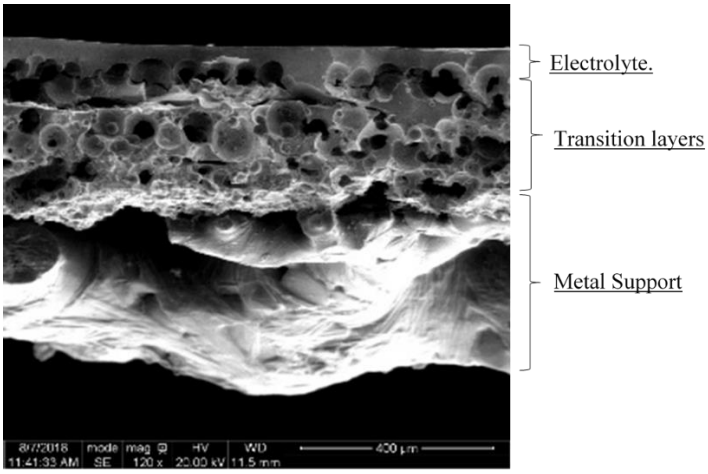

Figure 6.20: Cross-sectional SEM of a sintered MS-SOFC half-cell with structure 1 ‘Metal Support | 50/50 transition layer | 30/70 transition layer | Porous YSZ | Dense YSZ (electrolyte).

Complete segregation of the different layers (metal support, transition, and electrolyte) is evident from the SEM picture. However, it seems that the metal support layer (bottom part) is making one solid phase with very big pore sizes. Also, the transition layers 50/50, 30/70, and porous YSZ layer appear to form one indistinguishable layer. There is also a crack running through the interface of

transition layers and electrolyte. Since samples were broken in half for cross-sectional SEM the crack can also be a result for that. Figure 6.21 shows the cross-sectional image of sintered MS-SOFC half-cell with cell structure 2 (Figure 6.19). Segregation between the different layers is clear. In structure 2, the transition layer comprises only one 50/50 transition layer, as opposed to 3 transition layers for structure 1 ('50/50', '30/70', and 'PYSZ'). It can be concluded that having three different transition layers in structure 1 does not make a big difference on the micro-structure of the cell, compared to having only one layer as in structure 2. The electrolyte in this case (cell structure 2) appears flat, the edges seen are because the cell was broken in half. Even though cells were dipped in liquid nitrogen and broken in half in a thick cloth, the electrolyte layer still cracks a little during the breaking process (attributed to the low thickness and brittle nature of electrolyte).

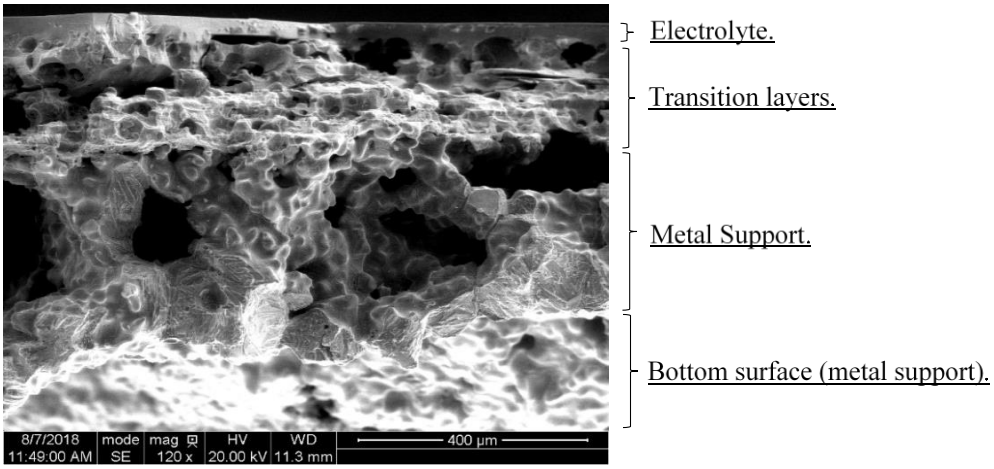

Figure 6.21: Cross-sectional SEM image of MS-SOFC sintered half-cell with structure 2 "Metal Support | 50/50 transition layer | Dense YSZ (electrolyte)".

Figure 6.22 shows the cross-sectional SEM image of cell with cell structure 3 (Figure 6.19). In this structure the mixed transition layers (mixture of stainless-steel and YSZ) were removed and only porous YSZ layer was used. Figure 6.20 shows clear segregation of the different layers. In cell structure 1, PYSZ was also employed, but as seen in Figure 6.20 the PYSZ layer was not distinguishable. Also, the presence of only Porous YSZ might lead to an increased Triple Phase Boundary (TPB) as the TPB in this case will be formed between the anode catalyst (NiO-SDC), electrolyte (YSZ), and the reactant fuel gas. Hence if a stand-alone layer of porous YSZ is incorporated in the cell it can lead to a higher TPB.

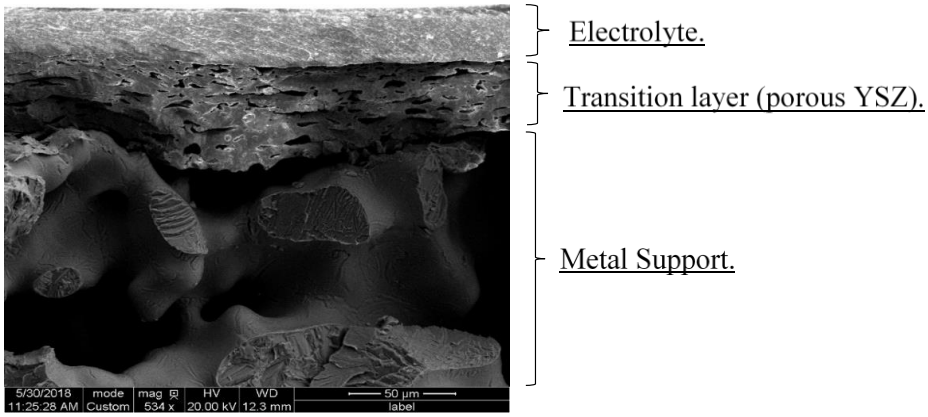

Figure 6.22: Cross-sectional SEM image of MS-SOFC sintered half-cell with the structure "Metal support | Porous YSZ | Electrolyte".

For structure 3, the porous YSZ layer has a very different structure compared to the transition layers of the other cell structures (Figure 6.20 and 6.21). The pore size is smaller, about 10 microns, whereas cells with structures 1 and 2 had pore sizes within the transition layers of up to 200 microns.

The low pore size of cell structure 3 might be a problem for anode catalyst solution infiltration. Cell performance will be compromised if the solution does not infiltrate the smaller pores of PYSZ layer. To increase the porosity of the porous YSZ layer in structure 3 the pore former content of PYSZ layer was increased. The cell shown in Figure 6.22 had 20 wt% pore former in PYSZ layer. Figure 6.23 shows pictures of MS-SOFC half-cells in which PYSZ layers had 30 and 40 wt% pore former.

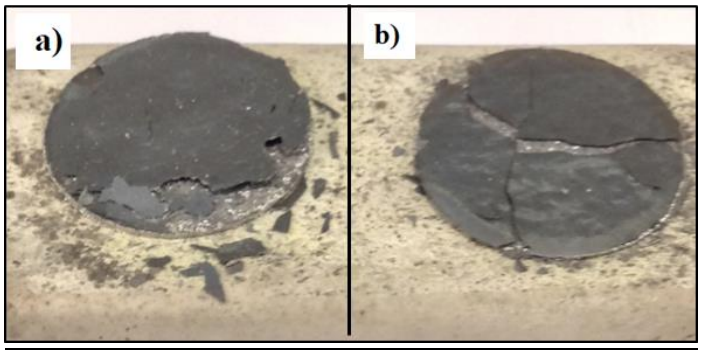

Figure 6.23: Co-sintered MS-SOFC half-cells; a) cell had 30 wt% pore former in PYSZ layer, b) cell has 40 wt % pore former in PYSZ layer.

Increasing pore former to more than 20 wt% leads to layer delamination and cracking of cell during co-sintering. Hence, structure 3 was discarded. Since structures 1 and 2 led to similar cells, structure 2 was selected for the next phase of the study because of its simpler configuration.

The next step is the infiltration of the anode electrocatalyst, and deposition of the cathode.

Anode catalyst infiltration.

A mixture of nickel oxide and Samarium Doped Ceria (SDC) was used as anode catalyst. Solution infiltration was used to incorporate the catalyst on the porous metal support side where a solution of nickel nitrate, samarium nitrate and cerium nitrate was infiltrated in the porous metal support. After infiltration the samples were heat treated at 400℃ (burn-out step) to thermally break down nitrates into oxides. The powder formed was run through XRD, and the resulting spectra is shown in Figure 6.24.

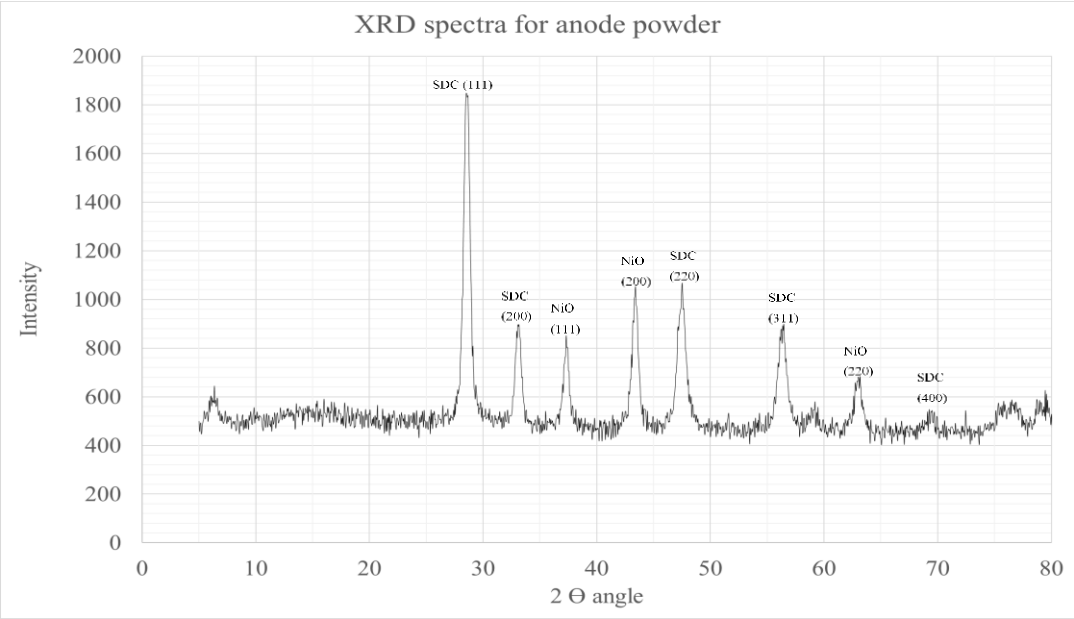

Figure 6.24: XRD spectra of anode powder made through heat treatment of anode catalyst solution (nitrate solution of Ni, Ce, and Sm).

The XRD spectra of the powder show peaks pertaining to only SDC and NiO. This shows that after every infiltration, a heat cycle at 400℃ will thermally crack the nitrates into oxides. The

amount of catalyst loaded on to the cell is important, with a target of 10 wt% with respect to the mass of the co-sintered sample. 5 to 6 infiltration cycles were necessary to achieve this target.

Since the burn-out is done in air, there is a chance of metal support oxidation. Figure 6.25 shows the TGA results of sintered metal support which underwent the first burn-out cycle. Figure 6.25 shows that there is an initial drop in mass, which is attributed to the removal of moisture in the sample. This is followed by a gradual, albeit small, increase in mass when the temperature reaches ~140°C. Hence, the actual mass percentage gained during one cycle is 0.04%. Jasinski et al. [42] reported mass percentage gain of 0.3% for SS-430L over approximately 225 hours at 400°C in air (Figure 3 in [42]). Through their graph a rough estimation shows that mass gain in the first 15 hours of operation is up to 0.06%. In [42] the samples were sintered at 1000°C as opposed to 1350°C in our case.

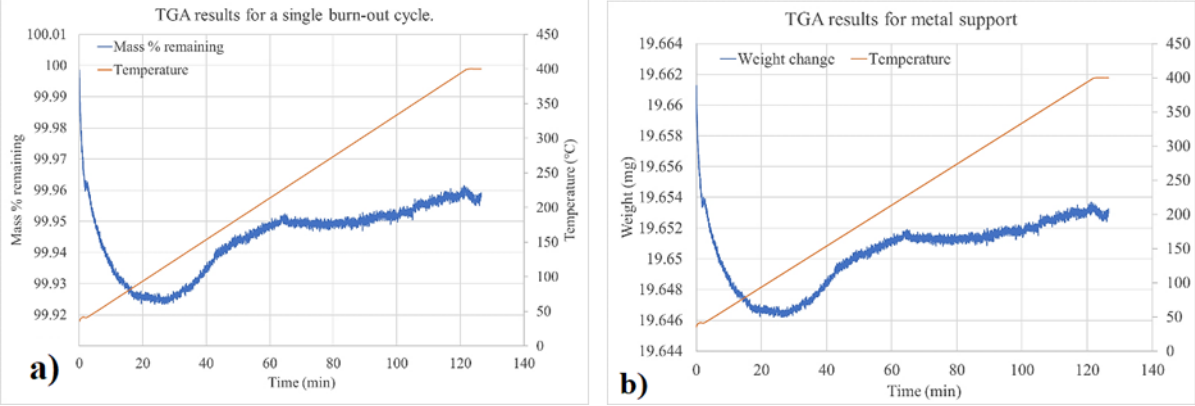

Figure 6.25: TGA result for sintered metal support for the first anode burn-out cycle. a) Percentage mass change with temperature and time; b) Actual mass change with temperature and time.

Oxidation of stainless-steel is due to the oxidation of silicon, aluminium, and chromium in the structure. It has been reported that the initial formation of chromia is not detrimental to the metal support as it is conductive and also protects iron from oxidation [35]. However, when chromia scale starts to grow (continued oxidation of chromium in SS-430L) then the chromia scale can lead to break away oxidation, spalling and disconnected structure of metal support which can reduce conductivity [54]. In the case of metal support structures for SOFCs it has been reported that a chromia scale of 5 micron thickness can lead to physical damage to the metal support [28].

However, due to a very small percentage mass gain, the possibility of 5-micron thick chromia scale formation during one burn-out cycle is ruled out.

Figure 6.26 shows an SEM image of MS-SOFC half-cells infiltrated with 10 wt% NiO/SDC and heat treated at 400℃ after each infiltration cycle.

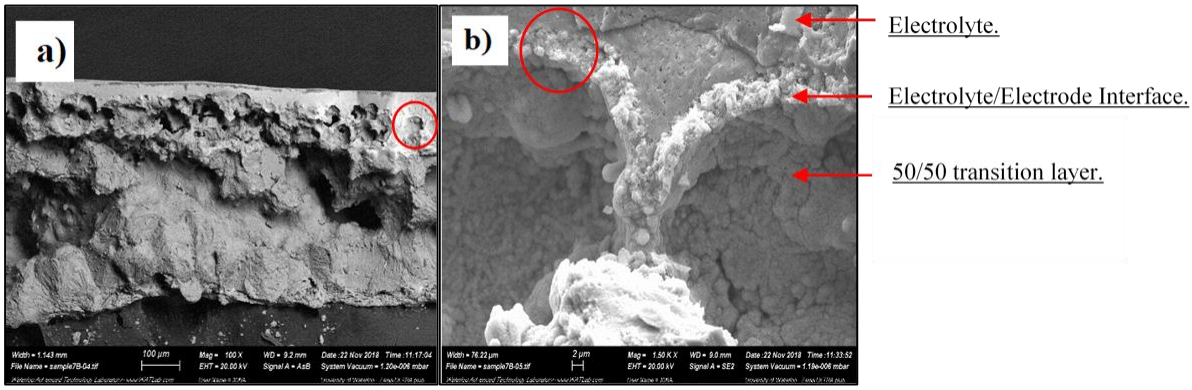

Figure 6.26: a) SEM image of MS-SOFC half-cell infiltrated with NiO/SDC and heat treated at 400℃, b) SEM image of section circled in Figure 6.24a (electrolyte-electrode interface).

The cross-section of the cell seems to have a rough surface, this is because the samples were broken in half before SEM. The high magnification image in Figure 6.26b shows the electrolyte (top)-transition layer (bottom) interface. It can be seen that there is a thick coating of infiltrated NiO/SDC on the interface. Figure 6.27 shows a further zoomed in SEM image (of circled section Figure 6.26b), with corresponding EDX spectra in Figure 6.28.

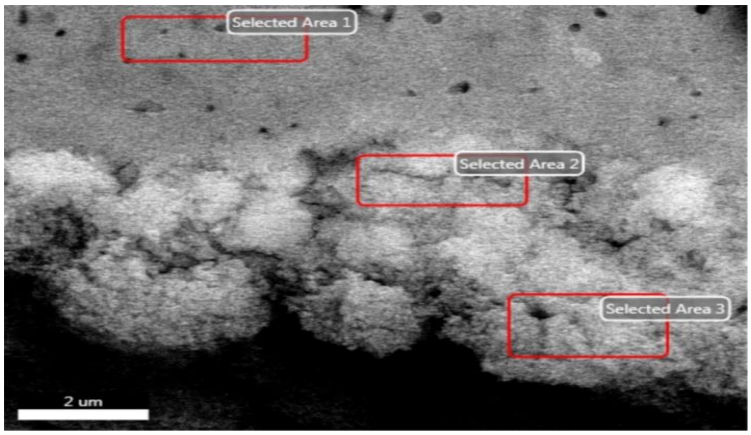

Figure 6.27: SEM image of electrolyte-transition layer interface.

Three different areas were selected for EDX measurement; ‘selected area 1’ is in the electrolyte region, ‘selected area 2’ is right at the boundary of electrolyte, and ‘selected area 3’ is on the anode catalyst.

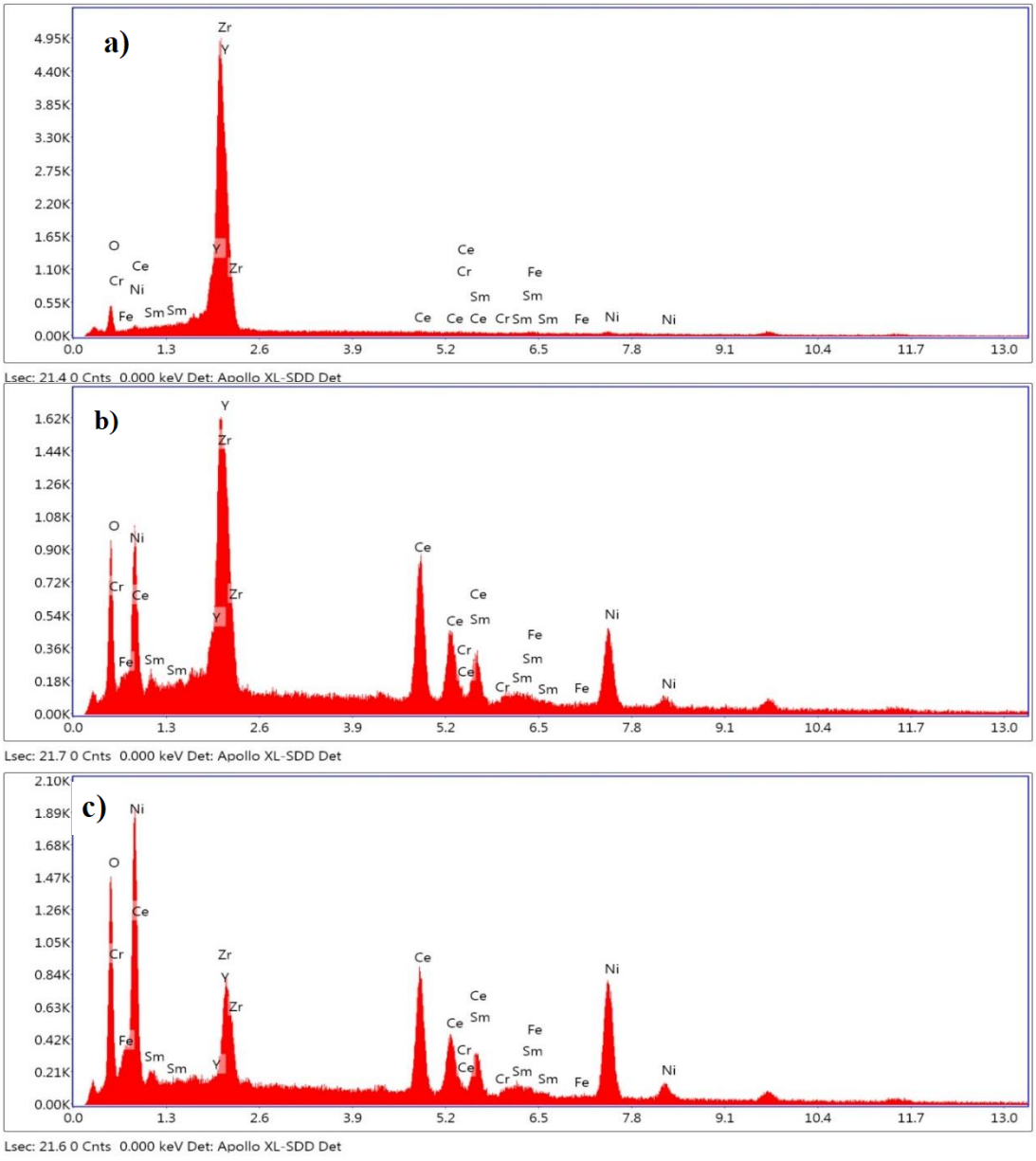

Figure 6.28: EDX spectra of selected areas in Figure 6.25; a) EDX spectra of selected area 1, b) EDX spectra of selected area 2, and c) EDX spectra of selected area 3.

From the EDX spectra in Figure 6.28a it is clear that the top region is pure YSZ only. The EDX spectra in figure 6.86b and c show that NiO/SDC is infiltrated up till to the start of electrolyte.

Through EDX spectra, comparing Figure 6.28b(interface) and 6.28c (anode catalyst) shows that Ni, Ce, and Sm are infiltrated up to the interface. From SEM it was also determined that the approximate particle sizes of NiO/SDC were in the range of 20-45 nm.

The above characterization confirms that solution infiltration and subsequent heat treatment at 400℃ lead to incorporation of NiO/SDC throughout MS-SOFCs, in particular up to the electrolyte.

Deposition of cathode:

LSCF/GDC was used as cathode with the fabricated MS-SOFCs and applied by printing on the electrolyte surface. Figure 6.29 is a picture of a MS-SOFC with anode and cathode catalyst used for electrochemical performance testing.

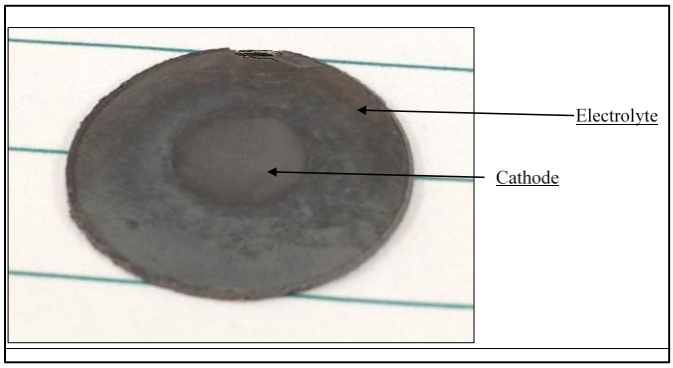

Figure 6.29: Picture of a MS-SOFC with anode and cathode catalyst.

Figure 6.30 shows a SEM image of a cross-section of MS-SOFC with cathode.

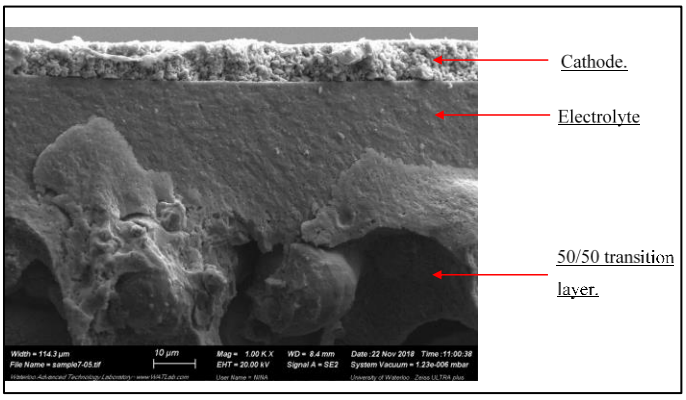

Figure 6.30: SEM image of cross-section of MS-SOFC with sintered cathode.

In Figure 6.30, the top layer is the cathode sintered at 1100℃ for 2 hours in argon. The middle layer is electrolyte and the bottom layer is a part of transition layer. The thickness of the sintered cathode was approximately 10 microns. The morphology of the cathode layer looks porous and there is a complete segregation of cathode layer from the electrolyte. After sintering, a brush was used to rub the surface of the cathode to see if it comes off or turns into powder; the cathode layer stayed intact.

Electrochemical Performance test

For electrochemical performance test full MS-SOFCs were used. Polarization curve, EIS, and microstructural analysis of used cell was used to fully characterize the fabricated cell's performance. The OCV of cells in humidified hydrogen at 700℃ was 0.989 V. Figure 6.31 shows the polarization curve (Figure 6.31a) and Nyquist plot (Figure 6.31b) at 700℃ under humidified hydrogen. The performance of the tested cell was very low compared to that of cells reported in literature. The Maximum Power Density (MPD) was 0.66 $mW.cm^{-2}$, compared to ~425 $mW.cm^{-2}$ for a cell with similar electrode catalysts[79]. Figure 6.31b shows the Nyquist plot for this cell at 2.47 $mA.cm^{-2}$ at 700℃. Both ohmic (close to 80 ohms) and polarization resistance (220 ohms) are very high.

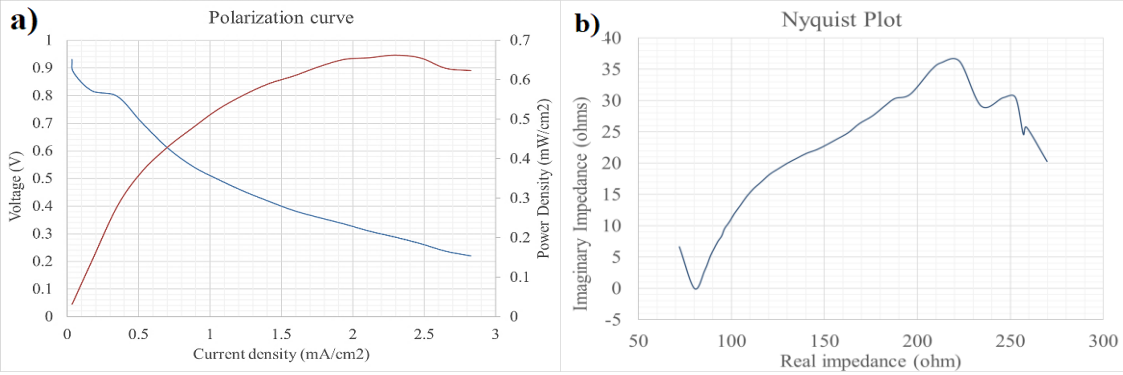

Figure 6.31: a) Polarization curve of MS-SOFC tested at 700℃; b) Nyquist plot for the same MS-SOFC at 700℃ with 2.47 $mA.cm^{-2}$ current density.

Ohmic resistance is the summation of all the resistances to charge conduction through the cell which includes the resistance faced at interface of current collector-electrode, electrode-electrolyte, and through electrolyte. In this case, since the OCV (an indication of gas-tightness of

electrolyte) is close to 1.0 V, the high ohmic resistance is attributed to high resistance to electron transfer between current collector and electrodes.

Polarization resistance depicts mostly the resistance faced in the electrodes, i.e. the resistance to charge transfer reactions, and transfer of oxygen ions between electrolyte and electrode. Figure 6.32 shows SEM of cross-section of the MS-SOFC used in performance testing.

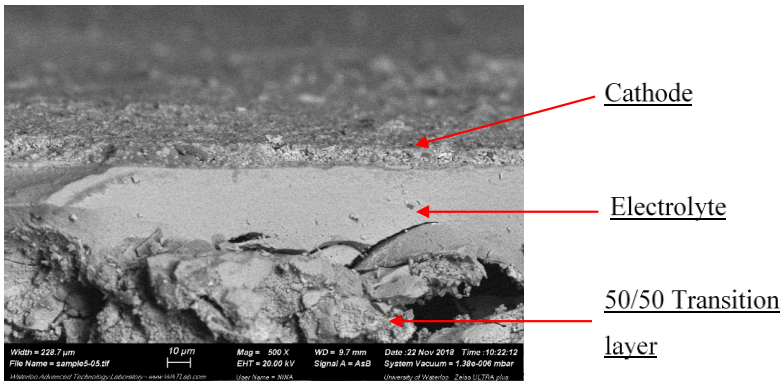

Figure 6.32: SEM image of cross-section of MS-SOFC used in performance testing. The top layer is cathode, the middle layer is electrolyte, and the bottom layer is the 50/50 transition layer.

In Figure 6.32 crack or delamination between the electrolyte and transition layer can be seen. However, this is attributed to the fact that these cells were fractured for SEM which can cause cracking and delamination of layers. Figure 6.33 shows an SEM image with high magnification showing the infiltrated anode catalyst after cathode sintering (before operation), and after operation.

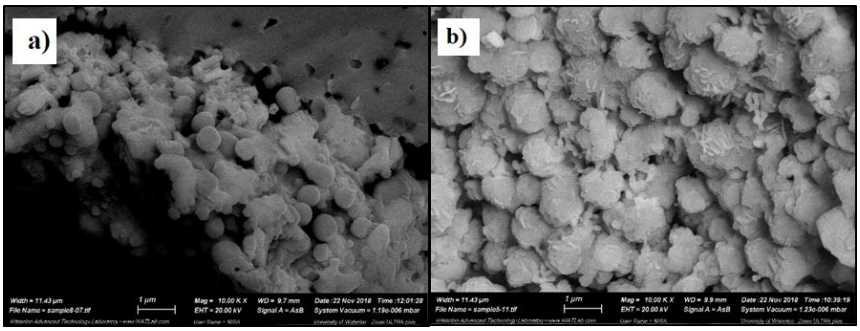

Figure 6.33: a) SEM image of anode catalyst before cathode sintering; b) SEM image of anode catalyst after operation.

SEM was used to measure the size of particles for anode catalyst, and it was seen that particle size increases from ~650 nm to ~1000nm during operation. This will increase the anode polarization due to decrease in active area with high particle size. The particle size during cathode sintering increases from 25-40 nm (Figure 6.27) to ~650 nm. This shows that particle size increases more during the sintering of cathode than during operation. Figure 6.34 shows the surface of cathode before and after operation of cell.

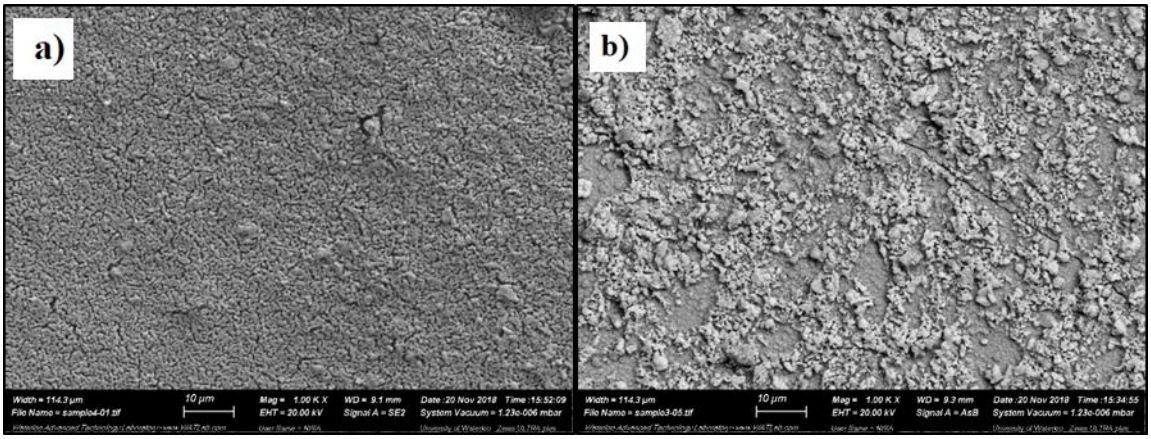

Figure 6.34: a) SEM image of cathode surface before operation, b) SEM image of cathode surface after operation.

It can be seen that the cathode surface is broken during operation which is attributed to reaction between cathode (LSCF/GDC) with the electrolyte (YSZ). This will also contribute to a high polarization resistance of the cell.

Summary

This chapter gives out the results of study of tape casting and co-sintering for fabrication of Metal Supported-Solid Oxide Fuel Cells using ferritic Stainless-Steel 400 series. In summary the following conclusions were made:

1. SS-430L is a more suitable metal support material compared to SS-410L for MS-SOFCs fabricated using tape casting and co-sintering. This was based on shrinkage profiles of both

SS-430L and SS-410L up till 1400℃ which showed that SS-430L shrinks more than SS-410L.

2. Stable slurries were formulated for tape casting. For use in tape casting the slurry should be uniform, without agglomeration, and should not crack upon casting.
3. Based on the components of slurry used in this study, it was concluded that 12.5% pore former content was suitable for metal support layers. This gave a porosity in the range of 39-43%.
4. Shrinkage analysis of SS-430L and YSZ was done in reducing (5% H_2/95% Ar) and inert (Ar) atmosphere under different sintering temperature profiles. The primary difference in the temperature profiles was the ramping rate between 1000℃ and sintering temperature (1350℃), in this case 2.5℃/min, 5.0℃/min, and 7.5℃/min was used. The following information was extracted through this analysis:
    a. Regardless of the ramping rate SS-430L shows a similar trend in the shrinkage profile, represented by shrinkage vs. temperature plot and shrinkage rate vs. time plot, in reducing atmosphere. SS-430L shows two peaks in shrinkage rate one closer to 1150℃, and the second one close to 1350℃.
    b. Higher ramping rate enhances the sintering, more shrinkage, of SS-430L by increasing the shrinkage rate. This is attributed to the high driving force for sintering with high a higher ramping rate in reducing atmosphere.
    c. By increasing the ramping rate for YSZ sintering in reducing atmosphere, the shrinkage rate increases and YSZ shrinkage also experiences a delaying effect. This means that with increasing the ramping rate the shrinkage rate peak position moves to a higher temperature. In this case with 7.5℃/min ramping the shrinkage peak occurred close to 1325℃.
    d. It was observed that high ramping rate of 7.5℃/min when sintering in reducing atmosphere is suitable for co-sintering SS-430L and YSZ together. This is so that when the samples (pressed half-cells) reach sintering temperature (1350℃), YSZ (electrolyte), which is more brittle and thinner (compared to metal support layer), is soft and continues to shrink. Whereas SS-430L (metal support) should be close to its maximum shrinkage.

e. Shrinkage in inert atmosphere was ruled out as suitable for co-sintering of MS-SOFCs. The reason was formation of non-conductive alumina and silica during sintering. This leads to very high shrinkage of SS-430L which can cause SS-430L reaching its maximum shrinkage before reaching the sintering temperature. When this happens SS-430L is already stiff at sintering temperature and YSZ layer continues to shrink which can cause cracks, delamination, and warping of sintered half-cells.

5. Shrinkage analysis of copper co-doped SDC and SS-430L showed that there is a significant mis-match in the shrinkage profile of 0.5CSDC and SS-430L. The half-cells which were co-sintered were always cracked.
6. MS-SOFC half-cells were successfully fabricated using tape casting and co-sintering based on the sintering temperature profile fixed using dilatometry analysis. It was also observed that a scavenger (loose SS-430L powder here) is critical to remove any trace oxygen, which might lead to oxidation, in the sintering furnace. A counter weight (0.5 g/cm^{-2}) is placed on the pressed samples during sintering to avoid slight cell warping.
7. Solution infiltrate of anode electro-catalyst (NiO/SDC) can be used for adding anode catalyst to the porous metal support. After infiltration of metal nitrate solution, a heat treatment at 400°C ensures that nitrates break down to metal oxides.
8. Similarly, cathode catalyst (LSCF/GDC) can be printed on the YSZ surface and sintered at 1100°C for 2 hours.
9. Cell electrochemical performance showed an OCV close to 1.0 V. This implies that electrolyte is sufficiently dense and without any cracks. This means that co-sintering can be used to fabricate MS-SOFCs.
    a. Ohmic resistance was very high in the initial tests which was attributed to the high resistance to current at the current collector-electrode resistance.
    b. Polarization resistance was also very high and attributed to the poor performance of electrode catalysts. Anode catalyst showed coarsening during cathode sintering, and during operation. The particle size increased from 40nm to almost 1 micron. Similarly, deposited cathode seems to disintegrate during operation. Nickel coarsening and creak down of cathode can increase polarization resistance.

Chapter 7 Conclusions and Recommendations

7.1 Conclusions

The primary objective of this work was to fabricate MS-SOFCs with SDC and YSZ as electrolyte using co-sintering. To use SDC, a lower than conventional sintering temperature (up to 1400°C) was desired to reduce the exposure of SDC to reducing atmosphere (5% H_2/95% Argon). Hence a study a was done on the effectiveness of copper as a sintering additive for SDC. To use YSZ (does not have limitation of sintering atmosphere) tape casting and co-sintering was studied to fabricate MS-SOFCs, which includes a detailed study of shrinkage behavior analysis of SS-430L (used as metal support), SDC, and YSZ.

7.1.1 Use of copper as sintering aid for SDC

1. 0.5 mol% copper doping in SDC is sufficient to enhance the sintering of SDC for the following reasons:
    a. The sintering temperature is reduced to 1180°C, 170°C lower than for SDC (1350°C).
    b. Sample with 0.5 mol% copper content shrinks/densifies to the same extent as those with higher copper content, evident by similar grain size (1-2 micron), grain shape, and negligible visible surface porosity for sintered samples.
    c. 0.5 mol% copper samples show formation of an additional copper phase, but in lower amount than for higher copper content.
    d. Amongst samples doped with copper, the sample with 0.5 mol% copper shows the highest conductivity. Conductivity of plain SDC is 0.077 $S.cm^{-1}$ and that of 0.5CSDC is 0.0642 $S.cm^{-1}$ at 800°C.
2. Copper amount of 0.5 mol% and above affects both grain boundary and grain interior conductivity:
    a. Activation energies for grain interior conduction increase till 1.0 mol% copper content and then decrease till 5.0 mol% copper content.
    b. Activation energy for grain boundary conduction first increases by addition of 0.1 mol% copper and then decreases up to 0.5 mol% copper. 0.5 mol% is also when the copper oxide additional phase appears. Further increase in copper content (up to 5.0 mol%) increases the grain boundary conduction activation energy.

7.1.2 Fabrication of MS-SOFCs using tape casting and co-sintering

1. Reducing atmosphere (5% H_2 / 95% Ar) is more suitable for co-sintering of MS-SOFCs than inert atmosphere. The reason is that sintering of metal support (SS-430L) in inert atmosphere leads to formation of silica and alumina. Firstly, these oxides are non-conductive and will increase the ohmic resistance of the metal support. Secondly, these oxides act as sintering additives for metal support and enhance its shrinkage. Metal support sample sintered in inert atmosphere with 5.0 °C/min ramping rate shows a shrinkage of more than 26% before reaching sintering temperature compared to only 17.1% in reducing atmosphere. This means that the metal support in inert atmosphere will already be close to its final shrinkage and, therefore, stiff. Any continued shrinkage of thin YSZ layer will result in physical defects since one layer (metal support) is stiff and the second layer (YSZ) is shrinking.
2. SS-430L when sintered in reducing atmosphere at a temperature of 1350°C shows two shrinkage peaks regardless of the ramping rate used in sintering temperature profile. The features of the peaks are:
    a. These peaks are shrinkage rate peaks and indicate how fast shrinking is occurring at a given temperature. The shrinkage rate increases with increasing ramping rate and hence the peaks are bigger for samples sintered with higher ramping rate.
    b. Irrespective of the ramping rate, shrinkage peaks occur at the same temperatures, the first one around 1150°C and the second one around 1350°C.
    c. This signifies that shrinkage of SS-430L is more temperature dependant than time.
3. The type of atmosphere does not have a significant effect on YSZ shrinkage. However, by increasing the ramping rate, the shrinkage of YSZ is delayed. This means that at higher ramping rate, YSZ samples show shrinkage peak at higher temperature. For instance, for sintering in reducing atmosphere the shrinkage peak for YSZ with 2.5°C/min ramping rate occur at 1280°C compared to 1340°C for YSZ sintered at 7.5 °C/min.
4. A higher ramping rate (7.5 °C/min) is more suitable for MS-SOFC co-sintering with SS-430L as metal support and YSZ as electrolyte. Due to higher shrinkage of SS-430L at higher ramping rate, the metal support would have reached a high shrinkage upon reaching sintering temperature. Similarly, due to delayed shrinkage of YSZ with higher ramping rate, upon reaching sintering temperature YSZ layer will not be too dense or brittle. Hence, continued shrinkage of YSZ while at sintering temperature will not lead to any physical defects like cracking, delamination, and warping.

5. Shrinkage of SDC with copper starts at a lower temperature (~700°C) than SS-430L (~1100°C). During co-sintering, copper co-doped SDC will already be in its final stage of shrinkage, and hence brittle, when the SS-430L starts its shrinkage. Due to significant mismatch in shrinkage behavior of copper co-doped SDC and SS-430L, using sintering aid to lower the co-sintering temperature can not be used for MS-SOFC fabrication with copper co-doped SDC electrolyte.

7.2 Recommendations.

7.2.1 Use of copper as sintering aid for SDC

1. Copper content between 0.1 mol% and 0.5 mol% can be studied to find out the solubility limit of copper in SDC crystal structure.
2. SDC with copper sintering aid may still be useful for all-ceramic cells because reducing the sintering temperature may reduce nickel coarsening in the anode and reduce the cost. Hence, testing under such situation should be pursued.

7.2.2 Fabrication of MS-SOFC using tape casting and co-sintering

1. More detailed study on gas tightness of electrolyte can be done. Even though the cell showed OCV of up to 1.0 V, it can be further increased. This might require slight changes in the electrolyte slurry, as well as in the co-sintering profile. For instance, a denser slurry can be used for YSZ, and co-sintering dwell time can be increased.
2. Improvement in anode performance:
    a. The composition and loading of anode catalyst can be varied to improve cell performance by reducing anode polarization.
    b. The sequence of anode and cathode processing can be reversed. That means that cathode can be deposited and sintered first followed by anode catalyst infiltration and heat treatment cycles. Since the cathode sintering temperature is above 1000°C, it can lead to anode catalyst coarsening.
    c. Study of copper containing anode catalyst can be carried out. In the past it has been reported that copper has been used to mitigate carbon deposition and enhance electronic conduction of anode for all-ceramic SOFCs. Copper containing anode like Cu-Ni/SDC can be studied with MS-SOFCs.
3. Improvement of cathode performance:

a. Due to reaction between conventional cathode materials and YSZ, a SDC barrier layer should be used between YSZ electrolyte and cathode. Specifically, the deposition method and further processing of the barrier layer can be studied, including the possibility of using copper doped SDC for denser barrier layer at lower sintering temperature.
b. Alternative cathode materials, such as BSCF, and SBSC50, with lower reactivity with YSZ and which can be sintered at lower temperature can be studied with MS-SOFCs.
c. Ex-situ sintering of cathode can be studied, where the effect of sintering temperature and time on the cathode polarization can be evaluated.

References

[1] BP. BP Statistical Review of World Energy 2017. Br Pet 2017:1–52. doi:http://www.bp.com/content/dam/bp/en/corporate/pdf/energy-economics/statistical-review-2017/bp-statistical-review-of-world-energy-2017-full-report.pdf.

[2] AbolhosSseini H, Heshmati A, Altmann J. A review of renewable energy supply and energy efficiency technologies. IZA Discuss Pap Ser 2014:1–36.

[3] Global Temperature | Vital Signs – Climate Change: Vital Signs of the Planet n.d. https://climate.nasa.gov/vital-signs/global-temperature/ (accessed November 10, 2018).

[4] Curtin S, Gangi J. 2013 Fuel Cell Technologies Market Report. 2014.

[5] Strap L, Series V, Rectory K, Dec TD, Series OV. No Title 1838:127–30.

[6] Mobius H-H. On the history of solid electrolyte fuel cells. J Solid State Electrochem 1997;1:2–16. doi:10.1007/s100080050018.

[7] de Souza S, Visco S, De Jonghe LC. Thin-film solid oxide fuel cell with high performance at low-temperature. Solid State Ionics 1997;98:57–61. doi:10.1016/S0167-2738(96)00525-5.

[8] Steele BCH. Interfacial reactions associated with ceramic ion transport membranes. Solid State Ionics 1995;75:157–65. doi:10.1016/0167-2738(94)00182-R.

[9] Tanasini P, Cannarozzo M, Costamagna P, Faes A, Van Herle J, Hessler-Wyser A, et al. Experimental and theoretical investigation of degradation mechanisms by particle coarsening in sofc electrodes. Fuel Cells 2009;9:740–52. doi:10.1002/fuce.200800192.

[10] Lee JH, Moon H, Lee HW, Kim J, Kim JD, Yoon KH. Quantitative analysis of microstructure and its related electrical property of SOFC anode, Ni-YSZ cermet. Solid State Ionics 2002;148:15–26. doi:10.1016/S0167-2738(02)00050-4.

[11] Kennouche D, Chen-Wiegart Y -c. K, Cronin JS, Wang J, Barnett SA. Three-Dimensional Microstructural Evolution of Ni- Yttria-Stabilized Zirconia Solid Oxide Fuel Cell Anodes At Elevated Temperatures. J Electrochem Soc 2013;160:F1293–304. doi:10.1149/2.084311jes.

[12] Brandon NP, Ruiz-Trejo E, Boldrin P. Solid Oxide Fuel Cell Lifetime and Reliability. London: Elsevier; 2017.

[13] Pihlatie M, Kaiser A, Mogensen M. Mechanical properties of NiO/Ni-YSZ composites depending on temperature, porosity and redox cycling. J Eur Ceram Soc 2009;29:1657–64. doi:10.1016/j.jeurceramsoc.2008.10.017.

[14] Cassidy M, Lindsay G, Kendall K. The reduction of nickel-zirconia cermet anodes and the effects on supported thin electrolytes. J Power Sources 1996;61:189–92. doi:10.1016/S0378-7753(96)02359-2.

[15] Waldbillig D, Wood A, Ivey DG. Electrochemical and microstructural characterization of the redox tolerance of solid oxide fuel cell anodes. J Power Sources 2005;145:206–15. doi:10.1016/j.jpowsour.2004.12.071.

[16] Tikekar NM, Armstrong TJ, Virkar A V. Reduction and Reoxidation Kinetics of Nickel-Based SOFC Anodes. J Electrochem Soc 2006;153:A654. doi:10.1149/1.2167949.

[17] Wood A, Pastula M, Waldbillig D, Ivey DG. Initial Testing of Solutions to Redox Problems with Anode-Supported SOFC. J Electrochem Soc 2006;153:A1929. doi:10.1149/1.2240085.

[18] Faes A, Hessler-Wyser A, Zryd A, Van Herle J. A review of RedOx cycling of solid oxide fuel cells anode. Membranes (Basel) 2012;2:585–664. doi:10.3390/membranes2030585.

[19] Ettler M, Timmermann H, Malzbender J, Weber A, Menzler NH. Durability of Ni anodes during reoxidation cycles. J Power Sources 2010;195:5452–67. doi:10.1016/j.jpowsour.2010.03.049.

[20] Sun B, Rudkin RA, Atkinson A. Effect of thermal cycling on residual stress and curvature of anode-supported SOFCs. Fuel Cells 2009;9:805–13. doi:10.1002/fuce.200800133.

[21] Tucker MC. Progress in metal-supported solid oxide fuel cells: A review. J Power Sources 2010;195:4570–82. doi:10.1016/j.jpowsour.2010.02.035.

[22] Williams KR, Smith JG, Sutton L. Fuel cells with solid state electrolytes 1969:3–7.

[23] Schiller G, Henne RH, Lang M, Ruckdäschel R, Schaper S. Development of vacuum plasma sprayed thin-film SOFC for reduced operating temperature. Fuel Cells Bull 2000;3:7–12. doi:10.1016/S1464-2859(00)88860-4.

[24] Li C, Li C, Ning X. Performance of YSZ electrolyte layer deposited by atmospheric plasma spraying for cermet-supported tubular SOFC 2004;73:699–703. doi:10.1016/j.vacuum.2003.12.096.

[25] Li C, Ohmori A. Relationships Between the Microstructure and properties of thermally sprayed deposits. J Therm Spray Technol 2002;11:365–74.

[26] Gupta M, Weber A, Markocsan N, Gindrat M. Electrochemical Performance of Plasma Sprayed Metal Supported Planar Solid Oxide Fuel Cells 2016;163:1059–65. doi:10.1149/2.0791609jes.

[27] Tucker MC, Jacobson CP, De Jonghe LC, Visco SJ. A braze system for sealing metal-supported solid oxide fuel cells. J Power Sources 2006;160:1049–57. doi:10.1016/j.jpowsour.2006.02.067.

[28] Tucker MC. Durability of symmetric-structured metal-supported solid oxide fuel cells. J Power Sources 2017;369:6–12. doi:10.1016/j.jpowsour.2017.09.075.

[29] Ren M. Development of Porous Meyal-Supported Solid Oxide Fuel Cells. McMaster University, 2013.

[30] Nakayama M, Ohshima H, Nogami M, Martin M. A concerted migration mechanism of mixed oxide ion and electron conduction in reduced ceria studied by first-principles density functional theory. Phys Chem Chem Phys 2012;14:6079. doi:10.1039/c2cp00020b.

[31] Zhang X, Dec C, Yick S, Robertson M, Kesler O, Maric R, et al. Short communication A study on sintering aids for Sm 0 . 2 Ce 0 . 8 O 1 . 9 electrolyte 2006;162:480–5. doi:10.1016/j.jpowsour.2006.06.061.

[32] Dong Y, Hampshire S, Lin B, Ling Y, Zhang X. High sintering activity Cu-Gd co-doped CeO2 electrolyte for solid oxide fuel cells. J Power Sources 2010;195:6510–5. doi:10.1039/c7sc04156j.

[33] Dong Y, Hampshire S, Zhou JE, Meng G. Synthesis and sintering of Gd-doped CeO2electrolytes with and without 1 at.% CuO dopping for solid oxide fuel cell applications. Int J Hydrogen Energy 2011;36:5054–66. doi:10.1016/j.ijhydene.2011.01.030.

[34] Lima CGM, Santos TH, Grilo JPF, Dutra RPS, Nascimento RM, Rajesh S, et al. Synthesis and properties of CuO-doped Ce0.9Gd0.1O2-δ electrolytes for for SOFCs. Ceram Int 2015;41:4161–8. doi:10.1016/j.ceramint.2014.12.093.

[35] Krishnan VV. Recent developments in metal-supported solid oxide fuel cells. Wiley Interdiscip Rev

Energy Environ 2017;6. doi:10.1002/wene.246.

[36] Lewandowski CM, Co-investigator N, Lewandowski CM, Bash E. Ceres Power Steel Cell Technology: Rapid Progress Towards a Truly Commercially Viable SOFC. PhD Propos 2015;1:1–18. doi:10.1017/CBO9781107415324.004.

[37] Choi JH, Lee T, Choi M, Yoo YS, Baek SW, Bae J. Long-term performance of anode-supported SOFC integrated with metal interconnect by joining process. Int J Hydrogen Energy 2010;35:4285–91. doi:10.1016/j.ijhydene.2010.02.062.

[38] Zhan Z, Zhou Y, Wang S, Liu X, Meng X, Wen T. Nanostructure Electrodes for Metal-Supported Solid Oxide Fuel Cells. ECS Trans 2013;57:925–31. doi:10.1149/05701.0925ecst.

[39] Hwang CS, Tsai CH, Chang CL, Chuang CM, Shie ZYC, Cheng SW, et al. Plasma sprayed metal-supported solid oxide fuel cell and stack with nanostructured anodes and diffusion barrier layer. Thin Solid Films 2014;570:183–8. doi:10.1016/j.tsf.2014.02.034.

[40] Lee C, Bae J. Fabrication and characterization of metal-supported solid oxide fuel cells. J Power Sources 2008;176:62–9. doi:10.1016/j.jpowsour.2007.10.067.

[41] Liu Z, Liu B, Ding D, Jiang Z, Xia C. Development of three-layer intermediate temperature solid oxide fuel cells with direct stainless steel based anodes. Int J Hydrogen Energy 2012;37:4401–5. doi:10.1016/j.ijhydene.2011.11.115.

[42] Molin S, Kusz B, Gazda M, Jasinski P. Evaluation of porous 430L stainless steel for SOFC operation at intermediate temperatures. J Power Sources 2008;181:31–7. doi:10.1016/j.jpowsour.2007.10.009.

[43] Jablonski PD, Sears JS. The impact of alloy chemistry on the formation of a silicon-rich subscale on two classes of ferritic steels. J Power Sources 2013;228:141–50. doi:10.1016/j.jpowsour.2012.11.107.

[44] Antepara I, Villarreal I, Rodríguez-Martínez LM, Lecanda N, Castro U, Laresgoiti A. Evaluation of ferritic steels for use as interconnects and porous metal supports in IT-SOFCs. J Power Sources 2005;151:103–7. doi:10.1016/j.jpowsour.2005.02.084.

[45] Sarasketa-Zabala E, Otaegi L, Rodriguez-Martinez LM, Alvarez MA, Burgos N, Castro F, et al. High temperature stability of porous metal substrates under highly humidified hydrogen conditions

for metal supported Solid Oxide Fuel Cells. Solid State Ionics 2012;222–223:16–22. doi:10.1016/j.ssi.2012.06.014.

[46] Ishihara T, Yan J, Enoki M, Okada S, Matsumoto H. Ni–Fe Alloy-Supported Intermediate Temperature SOFCs Using LaGaO[sub 3] Electrolyte Film for Quick Startup. J Fuel Cell Sci Technol 2008;5:031205. doi:10.1115/1.2930763.

[47] Hwang CS, Tsai CH, Hwang TJ, Chang CL, Yang SF, Lin JK. Novel Metal Substrates for High Power Metal-supported Solid Oxide Fuel Cells. Fuel Cells 2016;16:244–51. doi:10.1002/fuce.201500216.

[48] Yang SF, Shie ZYJ, Hwang CS, Tsai CH, Chang CL, Huang T. Ni-Mo Porous Alloy Fabricated as Supporting Component For Metal-Supported Solid Oxide Fuel Cell and Cell Performance. ECS Trans 2015;68:1849–55. doi:10.1149/06801.1849ecst.

[49] Karczewski J, Dunst KJ, Jasinski P, Molin S. High temperature corrosion and corrosion protection of porous Ni22Cr alloys. Surf Coatings Technol 2015;261:385–90. doi:10.1016/j.surfcoat.2014.10.051.

[50] Molin S, Gazda M, Jasinski P. Coatings for improvement of high temperature corrosion resistance of porous alloys. J Eur Ceram Soc 2011;31:2707–10. doi:10.1016/j.jeurceramsoc.2011.02.007.

[51] Brandon NP, Ruiz-Trejo E, Boldrin P. Solid Oxide Fuel Cell Lifetime and Reliability. Elsevier Ltd; 2017.

[52] Kim KJ, Kim SJ, Choi GM. Y0.08Sr0.88TiO3-CeO2composite as a diffusion barrier layer for stainless-steel supported solid oxide fuel cell. J Power Sources 2016;307:385–90. doi:10.1016/j.jpowsour.2015.12.130.

[53] Franco T, G. Schillera and AVKSZI. Ceramic Diffusion Barrier Layers for Metal Supported SOFCs. ECS Trans 2007;7:771–80. doi:10.1149/1.2729165.

[54] Yang ZG, Paxton DM, Weil KS, Stevenson JW, Singh P. Materials Properties Database for Selection of High-Temperature Alloys and Concepts of Alloy Design for SOFC Applications 2002:74.

[55] Zhou Y, Zhan Z, Wang S. Metal-Supported Solid Oxide Fuel Cells with Impregnated Electrodes. ECS Trans 2013;57:877–83. doi:10.1149/05701.0877ecst.

[56] Zhou Y, Zhang Z, Yuan C, Li J, Xia C, Zhan Z, et al. Metal-supported solid oxide fuel cells with in-situ sintered (Bi2O3)0.7(Er2O3)0.3-Ag composite cathode. Int J Hydrogen Energy 2013;38:16579–83. doi:10.1016/j.ijhydene.2013.02.068.

[57] Fernández-González R, Hernández E, Savvin S, Núñez P, Makradi A, Sabaté N, et al. A novel microstructured metal-supported solid oxide fuel cell. J Power Sources 2014;272:233–8. doi:10.1016/j.jpowsour.2014.08.081.

[58] Zhou Y, Yuan C, Chen T, Meng X, Ye X, Li J, et al. Evaluation of Ni and Ni-Ce0.8Sm0.2O2-δ(SDC) impregnated 430L anodes for metal-supported solid oxide fuel cells. J Power Sources 2014;267:117–22. doi:10.1016/j.jpowsour.2014.05.087.

[59] Blennow P, Hjelm J, Klemensø T, Persson A, Brodersen K, Srivastava A, et al. Development of Planar Metal Supported SOFC with Novel Cermet Anode. ECS Trans 2009:701–10. doi:10.1149/1.3205585.

[60] Lang M, Szabo P, Ilhan Z, Cinque S, Franco T, Schiller G. Development of solid oxide fuel cells and short stacks for mobile application. J Fuel Cell Sci Technol 2007;4:384–91. doi:10.1115/1.2756569.

[61] Rojek-Wöckner VA, Opitz AK, Brandner M, Mathé J, Bram M. A novel Ni/ceria-based anode for metal-supported solid oxide fuel cells. J Power Sources 2016;328:65–74. doi:10.1016/j.jpowsour.2016.07.075.

[62] Waldbillig D, Wood A, Ivey DG. Thermal analysis of the cyclic reduction and oxidation behaviour of SOFC anodes. Solid State Ionics 2005;176:847–59. doi:10.1016/j.ssi.2004.12.002.

[63] Holzer L, Iwanschitz B, Hocker T, Keller L, Pecho O, Sartoris G, et al. Redox cycling of Ni-YSZ anodes for solid oxide fuel cells: Influence of tortuosity, constriction and percolation factors on the effective transport properties. J Power Sources 2013;242:179–94. doi:10.1016/j.jpowsour.2013.05.047.

[64] Lee K, Kang J, Lee J, Lee S, Bae J. Evaluation of metal-supported solid oxide fuel cells (MS-SOFCs) fabricated at low temperature (~1,000 °C) using wet chemical coating processes and a catalyst wet impregnation method. Int J Hydrogen Energy 2018;43:3786–96. doi:10.1016/j.ijhydene.2018.01.027.

[65] Nielsen J, Persson ÅH, Sudireddy BR, Irvine JTS, Thydén K. Infiltrated La0.4Sr0.4Fe0.03Ni0.03Ti0.94O3based anodes for all ceramic and metal supported solid oxide fuel cells. J Power Sources 2017;372:99–106. doi:10.1016/j.jpowsour.2017.10.066.

[66] Zhou Y, Chen T, Li J, Yuan C, Xin X, Chen G, et al. Long-term stability of metal-supported solid oxide fuel cells employing infiltrated electrodes. J Power Sources 2015;295:67–73. doi:10.1016/j.jpowsour.2015.06.114.

[67] Liu X, Han D, Zhou Y, Meng X, Wu H, Li J, et al. Sc-substituted La0.6Sr0.4FeO3-δmixed conducting oxides as promising electrodes for symmetrical solid oxide fuel cells. J Power Sources 2014;246:457–63. doi:10.1016/j.jpowsour.2013.07.111.

[68] Zhou Y, Meng X, Yuan C, Luo T, Ye X, Li J, et al. SrFe0.75Mo0.25O3-δimpregnated 430L alloys for efficient fuel oxidation in metal supported solid oxide fuel cells. J Power Sources 2014;269:244–9. doi:10.1016/j.jpowsour.2014.06.092.

[69] Zhou Y, Liu X, Li J, Nie H, Ye X, Wang S, et al. Novel metal-supported solid oxide fuel cells with impregnated symmetric La0.6Sr0.4Fe0.9Sc0.1O3-δelectrodes. J Power Sources 2014;252:164–8. doi:10.1016/j.jpowsour.2013.12.020.

[70] Transactions ECS, Society TE. Investigation of Novel Electrocatalysts for Metal Supported Solid Oxide Fuel Cells - Ru:GDC 2015;68:1417–26.

[71] Hong YS, Kim SH, Kim WJ, Yoon HH. Fabrication and characterization GDC electrolyte thin films by e-beam technique for IT-SOFC. Curr Appl Phys 2011;11:S163–8. doi:10.1016/j.cap.2011.03.071.

[72] XU F, LI C, WANG Z, YE Z, ZHANG Y, ZENG Y. Preparation and characterization of SDC nanorods/LNC nanocomposite electrolyte. J Rare Earths 2016;34:711–6. doi:10.1016/S1002-0721(16)60083-2.

[73] Zhou Y, Yuan C, Chen T, Liu M, Li J, Wang S, et al. Enhanced Performance and Stability of Metal-Supported Solid Oxide Fuel Cells with (Bi2O3)0.7(Er2O3)0.3-Ag Composite Cathode. J Electrochem Soc 2014;162:F9–13. doi:10.1149/2.0131501jes.

[74] Zhou Y, Ye X, Li J, Zhan Z, Wang S. Metal-Supported Solid Oxide Fuel Cells with a Simple Structure. J Electrochem Soc 2014;161:F332–6. doi:10.1149/2.085403jes.

[75] Zhou Y, Meng X, Ye X, Li J, Wang S, Zhan Z. Metal-supported solid oxide fuel cells with impregnated SrFe0.75Mo0.25O3cathodes. J Power Sources 2014;247:556–61. doi:10.1016/j.jpowsour.2013.08.134.

[76] Zhou Y, Meng X, Liu X, Pan X, Li J, Ye X, et al. Novel architectured metal-supported solid oxide fuel cells with Mo-doped SrFeO3-δelectrocatalysts. J Power Sources 2014;267:128–35. doi:10.1016/j.jpowsour.2014.04.157.

[77] Tucker MC. Development of High Power Density Metal-Supported Solid Oxide Fuel Cells. Energy Technol 2017;5:2175–81. doi:10.1002/ente.201700242.

[78] Klemensø T, Nielsen J, Blennow P, Persson AH, Stegk T, Christensen BH, et al. High performance metal-supported solid oxide fuel cells with Gd-doped ceria barrier layers. J Power Sources 2011;196:9459–66. doi:10.1016/j.jpowsour.2011.07.014.

[79] Blennow P, Hjelm J, Klemensø T, Ramousse S, Kromp A, Leonide A, et al. Manufacturing and characterization of metal-supported solid oxide fuel cells. J Power Sources 2011;196:7117–25. doi:10.1016/j.jpowsour.2010.08.088.

[80] Stange M, Denonville C, Larring Y, Brevet A, Montani A, Sicardy O, et al. Improvement of corrosion properties of porous alloy supports for solid oxide fuel cells. Int J Hydrogen Energy 2017;42:12485–95. doi:10.1016/j.ijhydene.2017.03.170.

[81] Molin S, Tolczyk M, Gazda M, Jasinski P. Stainless Steel/Yttria Stabilized Zirconia Composite Supported Solid Oxide Fuel Cell. J Fuel Cell Sci Technol 2011;8:1–5. doi:10.1115/1.4003994.

[82] Haydn M, Ortner K, Franco T, Uhlenbruck S, Menzler NH, Stöver D, et al. Multi-layer thin-film electrolytes for metal supported solid oxide fuel cells. J Power Sources 2014;256:52–60. doi:10.1016/j.jpowsour.2014.01.043.

[83] Hwang C, Tsai CH, Lo CH, Sun CH. Plasma sprayed metal supported YSZ/Ni-LSGM-LSCF ITSOFC with nanostructured anode. J Power Sources 2008;180:132–42. doi:10.1016/j.jpowsour.2008.01.075.

[84] Hwang CS, Hwang TJ, Tsai CH, Chang CL, Yang SF, Wu MH, et al. Effect of plasma spraying power on LSGM electrolyte of metal-supported solid oxide fuel cells. Ceram Int 2017;43:S591–7. doi:10.1016/j.ceramint.2017.05.192.

[85] Hwang CS, Tsai CH, Yu JF, Chang CL, Lin JM, Shiu YH, et al. High performance metal-supported intermediate temperature solid oxide fuel cells fabricated by atmospheric plasma spraying. J Power Sources 2011;196:1932–9. doi:10.1016/j.jpowsour.2010.10.029.

[86] Rüttinger M, Mücke R, Franco T, Büchler O, Menzler NH, Venskutonis A. Metal-Supported Cells with Comparable Performance to Anode-Supported Cells in Short-Term Stack Environment. ECS Trans 2011;35:259–68. doi:10.1149/1.3570001.

[87] Transactions ECS, Society TE. Redox-stability of a Planar Metal-supported SOFC D. Roehrens 2013;57:665–72.

[88] Huang QA, Oberste-Berghaus J, Yang D, Yick S, Wang Z, Wang B, et al. Polarization analysis for metal-supported SOFCs from different fabrication processes. J Power Sources 2008;177:339–47. doi:10.1016/j.jpowsour.2007.11.092.

[89] Blennow P, Nielsen J, Hjalmarsson P, Hansen MH. Effect of low temperature in-situ sintering on the impedance and the performance of intermediate temperature solid oxide fuel cell cathodes. J Power Sources 2014;245:418–28. doi:10.1016/j.jpowsour.2013.06.067.

[90] Zhou Y, Han D, Yuan C, Liu M, Chen T, Wang S, et al. Infiltrated SmBa0.5Sr0.5Co2O5+δcathodes for metal-supported solid oxide fuel cells. Electrochim Acta 2014;149:231–6. doi:10.1016/j.electacta.2014.10.067.

[91] Baek SW, Jeong J, Kim JH, Lee C, Bae J. Interconnect-integrated solid oxide fuel cell with high temperature sinter-joining process. Int J Hydrogen Energy 2010;35:11878–89. doi:10.1016/j.ijhydene.2010.07.108.

[92] Baek SW, Jeong J, Kim YM, Kim JH, Shin S, Bae J. Metal-supported solid oxide fuel cells with barium-containing in-situ cathodes. Solid State Ionics 2011;192:387–93. doi:10.1016/j.ssi.2010.09.047.

[93] Han D, Wu H, Li J, Wang S, Zhan Z. Nanostructuring of SmBa0.5Sr0.5Co2O5+δ cathodes for reduced-temperature solid oxide fuel cells. J Power Sources 2014;246:409–16. doi:10.1016/j.jpowsour.2013.07.113.

[94] Blennow P, Klemensø T, Nielsen J, Persson ÅH, Stegk T, Hjalmarsson P, et al. Development of Long-term Stable and High-performing Metal-supported SOFCs T. Klemensø 2011;35:369–78.

[95] Zhou Y, Xin X, Li J, Ye X, Xia C, Wang S, et al. Performance and degradation of metal-supported solid oxide fuel cells with impregnated electrodes. Int J Hydrogen Energy 2014;39:2279–85. doi:10.1016/j.ijhydene.2013.11.086.

[96] Tucker MC, Ying AS. Metal-supported solid oxide fuel cells operated in direct-flame configuration. Int J Hydrogen Energy 2017;42:24426–34. doi:10.1016/j.ijhydene.2017.07.224.

[97] Li J, Wang S, Sun X, Liu R, Ye X, Wen Z. Improvement of (La0.74Bi0.10Sr0.16)MnO3-Bi1.4Er0.6O3composite cathodes for intermediate-temperature solid oxide fuel cells. J Power Sources 2008;185:649–55. doi:10.1016/j.jpowsour.2008.09.012.

[98] Lee C, Bae J, Kim JH, Baek S-W. La0.8Sr0.2Co1−xMnO3 Cathode and Its Application to Metal-Supported Solid Oxide Fuel Cells. J Fuel Cell Sci Technol 2010;7:021022. doi:10.1115/1.3182738.

[99] Baek S-W, Jeong J, Lee S, Bae J. Electrochemical Property of Cr-containing Cathode Materials for Metal-supported Solid Oxide Fuel Cell. ECS Trans., vol. 25, ECS; 2009, p. 2909–14. doi:10.1149/1.3205856.

[100] Tucker MC, Lau GY, Jacobson CP, DeJonghe LC, Visco SJ. Performance of metal-supported SOFCs with infiltrated electrodes. J Power Sources 2007;171:477–82. doi:10.1016/j.jpowsour.2007.06.076.

[101] Tucker MC, Lau GY, Jacobson CP, DeJonghe LC, Visco SJ. Stability and robustness of metal-supported SOFCs. J Power Sources 2008;175:447–51. doi:10.1016/j.jpowsour.2007.09.032.

[102] Tucker MC, Dogdibegovic E, Wang R, Lau GY. High performance metal-supported solid oxide fuel cells with infiltrated electrodes. J Power Sources 2019;410–411:91–8. doi:10.1016/j.jpowsour.2018.11.004.

[103] Tucker MC. Personal power using metal-supported solid oxide fuel cells operated in a camping stove flame. Int J Hydrogen Energy 2018:1–8. doi:10.1016/j.ijhydene.2018.03.161.

[104] Baertsch CD, Jensen KF, Hertz JL, Tuller HL, Vengallatore ST, Spearing SM, et al. Fabrication and structural characterization of self-supporting electrolyte membranes for a micro solid-oxide fuel cell. J Mater Res 2004;19:2604–15. doi:10.1557/JMR.2004.0350.

[105] Hayles J, Bao H. The reduction and oxidation of ceria: A natural abundance triple oxygen isotope perspective. Geochim Cosmochim Acta 2015;159:220–30. doi:10.1016/j.gca.2015.03.030.

[106] Yoshida H, Inagaki T. Effects of additives on the sintering properties of samaria-doped ceria. J Alloys Compd 2006;408–412:632–6. doi:10.1016/j.jallcom.2004.12.155.

[107] Yoshida H, Miura K, Fujita J, Inagaki T. Effect of gallia addition on the sintering behavior of samaria-doped ceria. JACerS 1999;82:219–21. doi:10.1111/j.1151-2916.1999.tb01747.x.

[108] Zhang T, Hing P, Huang H, Kilner J. Densification, microstructure and grain growth in the CeO2-Fe2O3system (0 ≤ Fe/Ce ≤ 20%). J Eur Ceram Soc 2001;21:2221–8. doi:10.1016/S0955-2219(00)00342-3.

[109] Zhang TS, Ma J, Kong LB, Chan SH, Hing P, Kilner JA. Iron oxide as an effective sintering aid and a grain boundary scavenger for ceria-based electrolytes. Solid State Ionics 2004;167:203–7. doi:10.1016/j.ssi.2004.01.006.

[110] Le S, Zhu S, Zhu X, Sun K. Densification of Sm0.2Ce0.8O1.9with the addition of lithium oxide as sintering aid. J Power Sources 2013;222:367–72. doi:10.1016/jjpowsour.2012.08.020.

[111] Santos TH, Grilo JPF, Loureiro FJA, Fagg DP, Fonseca FC, Macedo DA. Structure, densification and electrical properties of Gd3+and Cu2+co-doped ceria solid electrolytes for SOFC applications: Effects of Gd2O3content. Ceram Int 2017;44:2745–51. doi:10.1016/j.ceramint.2017.11.009.

[112] Nicholas JD, De Jonghe LC. Prediction and evaluation of sintering aids for Cerium Gadolinium Oxide. Solid State Ionics 2007;178:1187–94. doi:10.1016/j.ssi.2007.05.019.

[113] Sudarsan P, Krishnamoorthy SB. Grain boundary scavenging through reactive sintering of strontium and iron in samarium doped ceria electrolyte for ITSOFC applications. Mater Res Bull 2018;100:446–57. doi:10.1016/j.materresbull.2017.12.047.

[114] Gil V, Tartaj J, Moure C, Durán P. Sintering, microstructural development, and electrical properties of gadolinia-doped ceria electrolyte with bismuth oxide as a sintering aid. J Eur Ceram Soc 2006;26:3161–71. doi:10.1016/j.jeurceramsoc.2005.09.068.

[115] Chen D, Wang F, Shao Z. Interlayer-free electrodes for IT-SOFCs by applying Co 3O 4 as sintering aid. Int J Hydrogen Energy 2012;37:11946–54. doi:10.1016/j.ijhydene.2012.05.053.

[116] Villas-Boas LA, Figueiredo FML, De Souza DPF, Marques FMB. Zn as sintering aid for ceria-based electrolytes. Solid State Ionics 2014;262:522–5. doi:10.1016/j.ssi.2013.11.002.

[117] Zajac W, Suescun L, Świerczek K, Molenda J. Structural and electrical properties of grain boundaries in Ce0.85Gd0.15O1.925 solid electrolyte modified by addition of transition metal ions. J Power Sources 2009;194:2–9. doi:10.1016/j.jpowsour.2008.12.020.

[118] Kang SJ. Sintering Processes. Sinter. Densif. Grain Growth, Microstruct., Amsterdam, Boston, London: Elsevier Butterworth-Heinemann; 2005, p. 3–8. doi:10.1016/B978-0-7506-6385-4.50001-7.

[119] Rahaman MN. Sintering of Ceramics. Boca Raton: CRS press; 2008.

[120] German RM. Sintering Theory and Practice. John Wiley and Sons, Inc.; n.d.

[121] Kang SJ. Sintering: Densification, Grain Growth, and Microstructure. Amsterdam, Boston, London: Elsevier Butterworth-Heinemann; 2005.

[122] German RM, Rabin BH. Enhanced Sintering Through Second Phase Additions. Powder Metall 1985;28:7–12. doi:10.1179/pom.1985.28.1.7.

[123] Herring C. Effect of change of scale on sintering phenomena. J Appl Phys 1950;21:301–3. doi:10.1063/1.1699658.

[124] Ideris A. Carbon Formation Inhibition in Solid Oxide Fuel Cells (SOFCs) Using H2S 2014.

[125] Zhu T, Lin Y, Yang Z, Su D, Ma S, Han M, et al. Evaluation of Li2O as an efficient sintering aid for gadolinia-doped ceria electrolyte for solid oxide fuel cells. J Power Sources 2014;261:255–63. doi:10.1016/j.jpowsour.2014.03.010.

[126] Hermawan E, Sang Lee G, Sik Kim G, Chul Ham H, Han J, Pil Yoon S. Densification of an YSZ electrolyte layer prepared by chemical/electrochemical vapor deposition for metal-supported solid oxide fuel cells. Ceram Int 2017;43:10450–9. doi:10.1016/j.ceramint.2017.05.085.

[127] Zhang T, Hing P, Huang H, Kilner JA. Sintering and grain growth of CoO-doped CeO 2 ceramics. J Eur Ceram Soc 2002;22:27–34. doi:10.1016/S0955-2219(01)00240-0.

[128] Eltayeb A, Vijayaraghavan RK, McCoy AP, Cullen J, Daniels S, McGlynn E. Control of crystal structure, morphology and optical properties of ceria films by post deposition annealing treatments. Thin Solid Films 2016;603:363–70. doi:10.1016/j.tsf.2016.02.036.

[129] Peng R, Xia C, Peng D, Meng G. Effect of powder preparation on (CeO2)0.8(Sm 2O3)0.1 thin film properties by screen-printing. Mater Lett 2004;58:604–8. doi:10.1016/S0167-577X(03)00578-0.

[130] Liu M, Liu Z, Ding D, Liu M, Li X, Sun W, et al. Highly active Sm0.2Ce0.8O1.9powders of very low apparent density derived from mixed cerium sources. J Power Sources 2013;229:277–84. doi:10.1016/j.jpowsour.2012.11.082.

[131] Alenka Kosmač B (B). Stainless steels at high temperatures. vol. 19. 2000.

[132] Cho HJ, Choi GM. Fabrication and characterization of Ni-supported solid oxide fuel cell. Solid State Ionics 2009;180:792–5. doi:10.1016/j.ssi.2008.12.041.

APPENDIX A

Porosity calculation for sintered metal support

Data was collected for 12.5 wt% pore former content.

Collected Data

Table A.1: Measured values of mass for porosity measurement.

Description	Mass (grams)
Mass before impregnation	0.5627 ± 0.001
Mass after impregnation	0.6064 ± 0.001
Mass impregnated	0.0437 ± 0.002

Density of stainless-steel 430L: **7.8 g.cm^{-3}**

Density of oil: **0.9118 g.cm^{-3}**

Volume of stainless-steel 430L: $\frac{mass}{volume}$ = 0.5627/7.8 = **0.072 ± 0.0001 cm^3**

Volume of oil: $\frac{mass}{density}$ = 0.0437/0.9118 = **0.048 ± 0.0022 cm^3**

Porosity = $\frac{Volume\ of\ oil}{Total\ volume}$ = $\frac{0.048}{(0.048 + 0.072)}$ = **0.4 ± 0.024.**

APPENDIX B

Use of EIS for conductivity and activation energy calculation.

Conductivity calculation

Figure B.1 shows Nyquist plot (experimental and fit) for 0.5 CSDC at 400°C

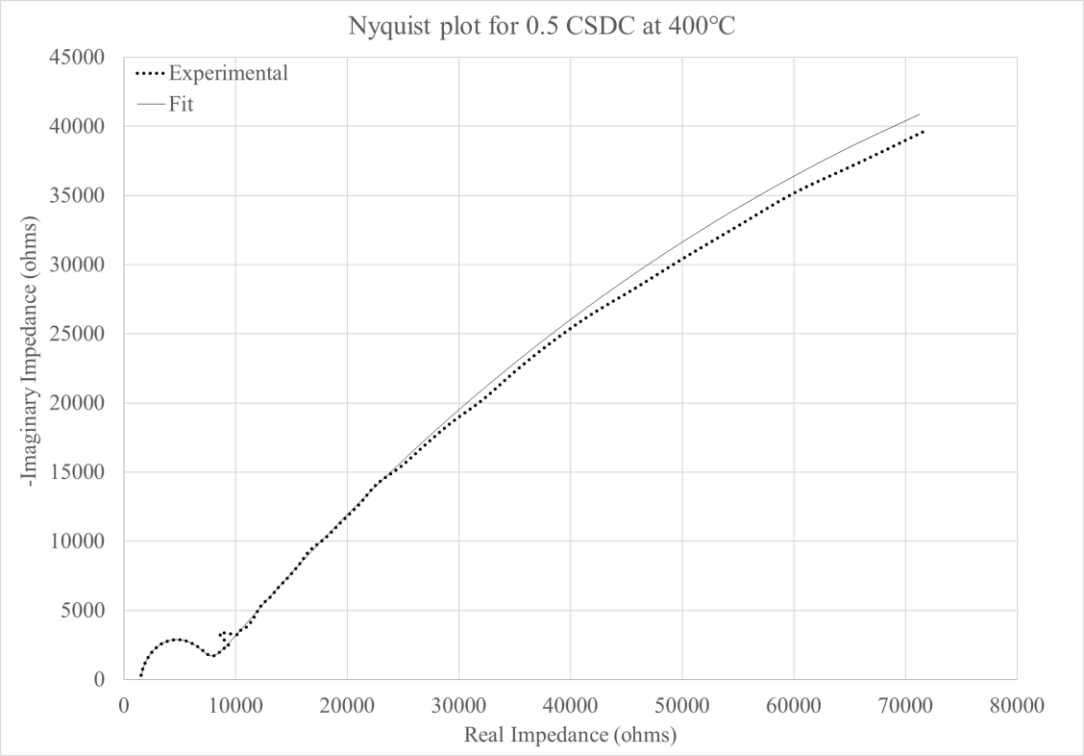

Figure B.1: Nyquist plot for 0.5CSDC at 400°C.

Equivalent circuit data fitting was done using z-view software. Fitting of experimental was used to get values of resistance for grain interior and grain boundary.

Grain interion resistance (R_{gi}) = **1478 ohms.**

Grain boundary resistance (R_{gb}) = **5374 ohms.**

Total resistance (R_T) = R_{gi} + R_{gb} = **6852 ohms.**

Conductivity (σ) = $\frac{Length}{Resistance.Area}$

Thickness of sample = 0.0944 cm

Area = 0.283 cm^2

Grain interior conductivity (σ_{gi}) = **2.26×10^{-4} S.cm^{-1}**

Grain boundary conductivity (σ_{gb}) = **6.21×10^{-5} S.cm^{-1}**

Total conductivity (σ_T) = **4.87×10^{-5} S.cm^{-1}**

Activation energy calculation

Arrhenius equation: $\sigma = \sigma_o exp\ (\frac{-E_A}{KT})$

For activation energy calculation, plot of Ln(conductivity) vs (1/Temperature) can be used. The slope of the linear plot is the ratio of activation energy and Boltzmann constant.

$$Ln(\sigma) = (\frac{-E_A}{K})(\frac{1}{T}) + Ln(\sigma_o)$$

Figure B.2 shows Arrhenius plot of PSDC grain boundary conductivity.

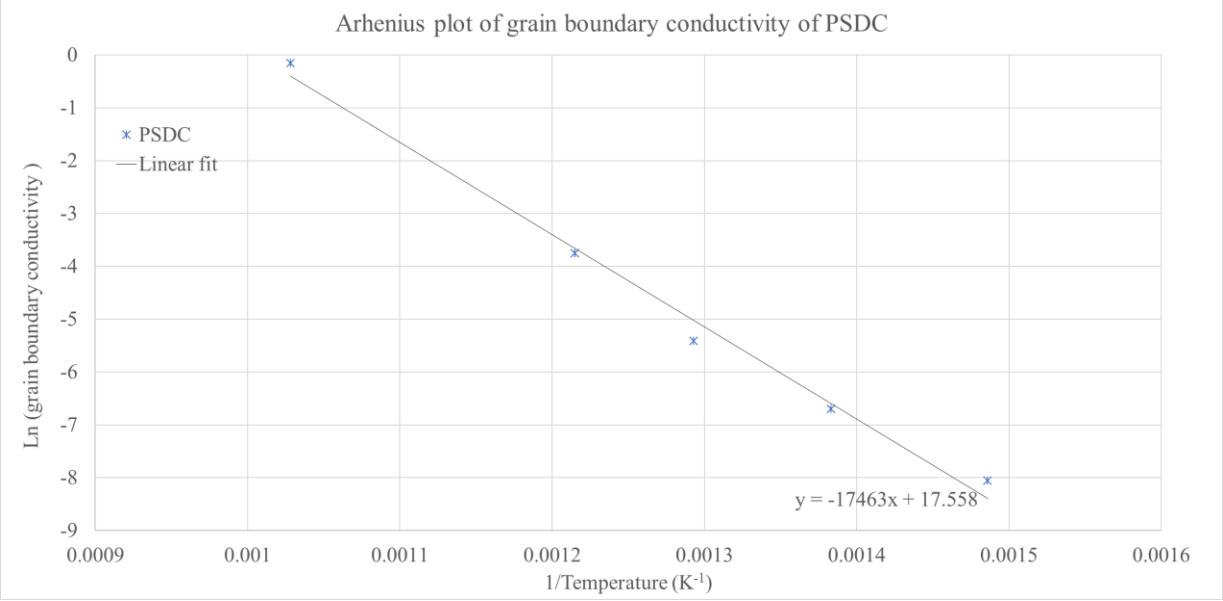

Figure B.2: Arrhenius plot of PSDC grain boundary conductivity.

From Figure B.2:

$$\frac{-E_A}{K} = -17463$$

$E_A = (-17463) \times K = (-17463) \times (-8.6173303 \times 10^{-5}) = 1.52$ eV